Institut für Meteorologie und Klimatologie
Gottfried Wilhelm Leibniz Universität Hannover

Coriolis Instabilities in Coupled Atmosphere-Ocean Large-Eddy Simulations

Jens Fricke

Diploma Thesis in Meteorology
-Corrected version-

June 2011

Contents

List of Figures

List of Tables

List of Symbols and Abbreviations

Abbreviations

ABL	Atmospheric boundary layer
CFL	Courant-Friedrichs-Lewy (time step criterion)
DNS	Direct numerical simulation
FFT	Fast Fourier transformation
HLRN	Norddeutscher Verbund für Hoch- und Höchstleistungsrechnen
IMUK	Institute for Meteorology and Climatology at the Leibniz University of Hannover
IPI	Inflection point instability
LES	Large-eddy simulation
OML	Ocean mixed layer
OT	Other terms in the energy budget equations of the along-roll and the cross-roll components (section 1.4.1)
PALM	Parallelized large-eddy simulation model
PE	Processor element
PI	Parallel instability
POD	Proper orthogonal decomposition
RANS	Reynolds-averaged Navier-Stokes simulations
RK3	Third-order Runge-Kutta scheme
SGS	Subgrid-scale model
SGS-TKE	Subgrid-scale turbulent kinetic energy
TKE	Turbulent kinetic energy

Operators

Ψ_0	Basic state (Boussinesq approximation), surface value of a quantity
Ψ^*	Deviation from the basic state (Boussinesq approximation), energy of organized and unorganized turbulence e^*, deviation from a mean
$\overline{\Psi}$	Temporal or spatial average of a quantity, resolved part of a quantity
$< \Psi >$	Temporal or spatial average of a quantity
$\Psi^{'}$	Resolved-scale turbulence, deviation from a mean value
$\Psi^{''}$	Subgrid-scale turbulence

$\|\Psi\|$	Absolute value of a quantity Ψ
∂	Partial derivative operator
$\int$	Integral operator
$\sum$	Summation operator
$\lfloor x \rfloor$	Floor function of a real number x

Latin Letters

A_h, B_h	Coefficients for calculating the characteristic temperature
A_m, B_m	Coefficients for calculating the friction velocity
a_m, b_m	Coefficients for calculating the friction velocity in the one-dimensional model
c_m	Smagorinksy constant
c_p	Specific heat capacity at a constant pressure
c_0	Constant in the dissipation parameterization of the one-dimensional model
D	Ekman length
d	Distance from a bottom boundary or a wall
d_f	Damping factor
$d2_{nx}, d2_{ny}$	Number of oceanic grid points between two atmospheric grid points in x- and y-direction
E	Spectral turbulent kinetic energy
E_Ψ	Spectral energy of a quantity Ψ
E^*	Resolved-scale turbulent kinetic energy, normalized by the total number of grid points
e	Subgrid-scale turbulent kinetic energy
e^*	Energy of organized and unorganized turbulence
$e^*_\parallel, e^*_\perp$	Along- and cross-roll component of the roll energy
F_{real}, F_{imag}	Matrix with the real and imaginary values of the two-dimensional FFT
f, f^*	Horizontal and vertical Coriolis parameter
f_s	Stretching factor for the vertical grid length
g	Gravitational constant
H	Vertical extension of roll vortices
I	Turbulence intensity
$\vec{i},\vec{j},\vec{k}$	Unit vectors in x-,y- and z-direction
i, j, k	Integer indices $\in \{1, 2, 3\}$
ii, jj	Integer indices $ii \in [0, d2_{nx}]$, $jj \in [0, d2_{ny}]$

K_m, K_h, K_s	Turbulent diffusion coefficients for momentum, heat and scalars
k, k_x, k_y	Wavenumber
k_s	Index of the first height for the grid stretching
L	Typical length scale of a boundary layer
L_x, L_y, L_z	Model domain size in x-, y- and z-direction
l	Mixing length
l_w	Specific heat of vaporization
$N; N_a, N_o$	Total number of grid points; for atmosphere and ocean
nx, ny	Number of grid points in x- and y-direction
P_d, P_n	Polynomials for the calculation of the ocean density after Jackett et al. (2006)
p	Pressure
Q_h, Q_S, Q_s	Source and sink terms for temperature, salinity and scalars
R	Ideal gas constant
R_f	Richardson flux number
R_v	Coefficient of the Rayleigh damping
r_i	Coefficient of the fractional time step of the Runge-Kutta time step scheme
Re	Reynolds number
Re_c	Critical Reynolds number
S	Salinity
S_Ψ	Spectral energy density
s	Scalar quantity
T	Temperature
t	Time
U	Typical velocity scale of a flow
$u, v, w; u_i$	Velocity components in x-,y- and z-direction, $i \in \{1, 2, 3\}$
u_g, v_g	Geostrophic wind velocity components
$u_*; u_{*,a}, u_{*,o}$	Friction velocity; for atmosphere and ocean
V	Volume of air or water
V_g	Geostrophic wind or surface current vector
$\vec{v}$	Velocity vector
$x, y, z; x_i$	Cartesian coordinates in space, $i \in \{1, 2, 3\}$
z_b	Bottom boundary height of the model domain
z_i	Height of the atmospheric boundary layer
z_{inv}	Height/depth of the beginning of the inversion layer
z_p	Prandtl layer height
z_R	Height of the beginning of the Rayleigh damping

z_t	Top boundary height of the model domain
z_0	Roughness length

Greek letters

α	Angle of deflection between the near surface flow and the geostrophic flow, angle of the geostrophic flow in relation to the north-east system
α_k	Kolmogorov constant
β	Angle between the roll axis and the north-east coordinate system
Δ	Characteristic grid length
Δt	Time step
$\Delta x, \Delta y, \Delta z; \Delta x_i$	Grid length in x-, y- and z-direction, $i \in \{1, 2, 3\}$
Δk	Difference between neighboring wavenumbers
δ_{ij}	Kronecker delta
ϵ	Angle between roll axis and the geostrophic flow (band orientation angle), dissipation rate
ϵ_{ijk}	Levi-Civita symbol
η	Kolmogorov microscale
θ	Potential temperature
ϑ_*	Characteristic temperature
κ	von Karman constant
λ	Wavelength, typical length scale
λ_r	Wavelength of the roll vortices
ν_m, ν_h, ν_s	Molecular viscosity of momentum, heat and scalars
ρ	Density, in-situ density of the ocean model
ρ_a, ρ_o	Density of the atmosphere and ocean
ρ_{pot}	Potential density
σ_Ψ	Standard deviation of a quantity Ψ
τ	Surface stress
τ_i	Period of the inertial oscillation
τ_{ki}	Subgrid-scale stress tensor
ϕ	Geographical latitude
Φ_m, Φ_h	Businger-Dyer function
χ	Quantity
Ψ	Quantity
ψ	Quantity
$\vec{\Omega}$	Earth rotation vector
Ω	Angular velocity of the earth

1. Introduction

The present study investigates the influence of atmospheric roll vortices on the flow structure of a wind driven ocean boundary layer. Therefore, a neutrally stratified Ekman flow is simulated in the atmosphere and ocean with a large-eddy simulation (LES) model. The present chapter gives general information about the atmospheric boundary layer and the ocean boundary layer in the first two sections. Section 1.3 describes the Ekman flow and the Coriolis force. The responsible mechanisms for the roll development and the current state of research are presented in section 1.4. The chapter closes with the discussion of the purposes and approach of this work.

1.1. The atmospheric boundary layer

The atmospheric boundary layer (ABL) is the lowest part of the atmosphere and is directly influenced by the earth's surface. The flow in the ABL is affected by the surface through frictional drag, heat and humidity transfer and the influence of the terrain. The height (or depth) of the ABL varies in space and time and ranges from a few hundred meters to a few kilometers. The significant transport of momentum, heat, moisture and solutes is achieved by turbulent motions (turbulent fluxes) in the ABL. Turbulence is three-dimensional, random and non-stationary and can be visualized as eddies. The size of the largest eddies is of the order of the boundary layer depth while the size of the smallest eddies is of the order of a few millimeters. The different scales of eddies have lifetimes from several hours (larger eddies) to few seconds (smaller eddies). In the bulk of the ABL, turbulent transport is approximately five orders of magnitude stronger than molecular transport (Stull, 1988; Etling, 2002).

In the ABL, turbulence is produced by wind shear and buoyancy forces, where the latter can also destruct turbulence. The influence of the buoyancy forces is described by the stratification of the ABL. Stable boundary layers are characterized by an increase of potential temperature with height and turbulence reduction due to negative buoyancy fluxes. For example, a stable boundary layer develop at night over land when the surface cools due to long wave radiation. Convective boundary layers are well mixed over the bulk of the ABL due to thermal buoyancy caused by surface heating. In neutrally stratified boundary layers, the potential temperature is constant with height. Hence, buoyancy forces have not an influence on the turbulence production. For example, this type occurs in a strong wind situation under a cloudy sky (Stull, 1988; Kraus, 2008).
The flow of the ABL is driven by a large scale pressure gradient. The ABL can be divided into three parts. The lowest few millimeters are the viscous sublayer where molecular transport dominates turbulent transport. The layer above is called surface layer or Prandtl layer with a vertical thickness of less than 100 m. Turbulent fluxes vary by less than 10 % of their magnitude within the surface layer. The influence of the Coriolis force is negligible small compared to the friction force. The mean wind speed increases with height up to a value between 70 % and 80 % of the wind speed at the top of the ABL (Etling, 2002; Kraus, 2008). The upper

part of an ABL is called Ekman layer which is characterized by an equilibrium of the pressure gradient force, the friction force and the Coriolis force. The friction force decreases with height and hence the wind speed increases with height. As a consequence, the influence of the Coriolis force increases and the horizontal mean wind turns with height. The turbulent fluxes decrease to nearly zero at the top of the ABL. Above the ABL, in the free atmosphere, the influence of surface friction becomes insignificant and the wind is nearly geostrophic (Stull, 1988; Etling, 2002; Kraus, 2008). Further information about the flow in the Ekman layer are given in section 1.3.

1.2. The upper ocean boundary layer

The upper ocean boundary layer is the part of the ocean, which is directly affected by the atmosphere. At the sea surface, the ocean is driven by the atmosphere through heat and moisture fluxes and wind stress. The ocean boundary layer includes the sea surface with its wave field, the ocean mixed layer (OML) and the upper part of the pycnocline (Stewart, 2008; Thorpe, 2005).

Within the OML, temperature and salinity are constant or slightly decreasing with depth. The depth of the OML varies between a few meters and a few hundred of meters, depending on the heat exchange with the atmosphere and the induced turbulence by wave breaking and wind stress. The flow in the OML is driven at the sea surface by wind stress in contrast to the atmosphere which is driven by a large scale pressure gradient. Below the OML, the potential density strongly increases with depth. This layer is called pycnocline. The potential density increases if the temperature decreases or the salinity increases. In the pycnocline, the strong density gradient is mainly caused by the temperature gradient and hence the layer is also called thermocline. The upper part of the pycnocline is the seasonal thermocline and ranges down to several hundred meters. The strongest temperature and density gradients occur within that layer and have a slightly seasonal variation. The lower part of the pycnocline is not a part of the upper ocean boundary layer and is called the permanent thermocline. Within that layer, the temperature gradient does not change over decades (Stewart, 2008; Thorpe, 2005).

The ocean part of this study deals with the turbulent structure of the OML. In the OML, turbulence can be produced by several processes: Langmuir circulation, breaking surface waves, convection and shear. The latter is investigated in this work and further information about the flow are given in section 1.3. For a detailed explanation of the other processes, it should be directed to the literature. Breaking surface waves generate turbulence close to the sea surface (e.g. Kraus and Businger, 1994; Noh et al., 2004; Thorpe, 2005; Stewart, 2008). Wave propagation transports mass which is known as Stokes drift. Following the theory of Craik and Leibovich (1976), the Stokes drift at the sea surface induces Langmuir circulation. This circulation was first described by Langmuir (1938). The presence of Langmuir circulation can be seen in bands of floating material aligned parallel to the wind. A considerable amount of literature has been published about Langmuir circulation (e.g. Leibovich, 1983; Noh et al., 2004; Thorpe, 2004, 2005). In the OML, convection occurs if the water density increases towards the sea surface due to surface heat loss or increasing salinity caused by evaporation or ice forming. The denser water subsides and induces turbulent motions (e.g. Thorpe, 2005; Stewart, 2008).

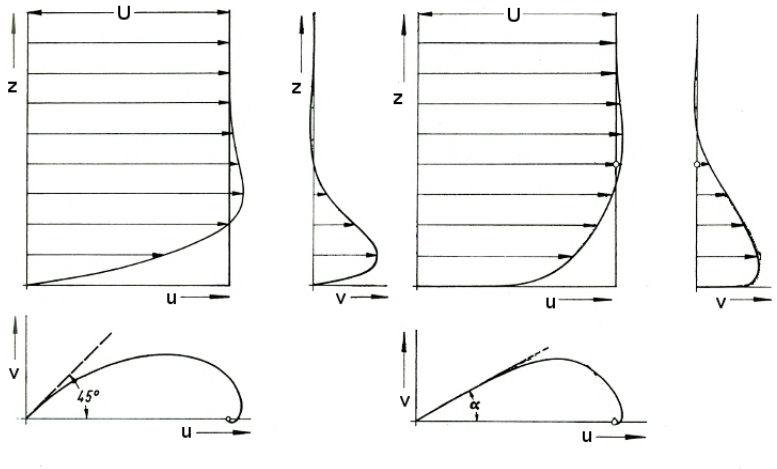

Figure 1.1.: Vertical profiles of the mean horizontal velocity components u and v of a quasi-laminar (left) and a turbulent (right) Ekman flow. z is the height, U the geostrophic flow and u and v the components of the mean horizontal flow. The hodographs (bottom) shows the angle of deflection α between the near-surface flow and the geostrophic flow at the top of the boundary layer (after Prandtl et al., 1969).

1.3. The Coriolis force and the Ekman layer

The flow of an ABL and the flow of the OML are affected by the Coriolis force. The force is caused by the earth's rotation which can be expressed as a vector $\vec{\Omega}$. In a cartesian coordinate system where the x-axis points east, the y-axis north and the z-axis in the vertical, $\vec{\Omega}$ can be divided into a horizontal and a vertical component (Etling, 2002):

$$\vec{\Omega} = \Omega \cos\phi \vec{j} + \Omega \sin\phi \vec{k} \,. \tag{1.1}$$

$\vec{j}$ and $\vec{k}$ are the unit vectors in y- and z-direction. ϕ represents the latitude and $\Omega = 2\pi/24\,\mathrm{h}$ is the angular velocity of the earth. With the flow components (u, v, w) along the respective spatial directions (x, y, z), the Coriolis force can be written as (Etling, 2002):

$$-2\vec{\Omega} \times \vec{v} = (fv - f^* w)\vec{i} - fu\vec{j} + f^* u\vec{k} \,, \tag{1.2}$$

with

$$f = 2\Omega \sin\phi \quad \text{and} \quad f^* = 2\Omega \cos\phi \,. \tag{1.3}$$

The Coriolis force acts perpendicular to the flow and deflects it. For the northern hemisphere, the acceleration caused by the Coriolis force is as follows: An eastward flow is accelerated southward by the term $-fu$ and vertically upward by f^*u. A northward flow is deflected eastward by the term fv and a vertically upward flow is deflected westward by $-f^*w$ (Gerkema et al., 2008).

The first description of an OML flow which is balanced by the friction force, Coriolis force and a large scale pressure gradient was given by Ekman (1905). He assumed a steady state flow which is horizontally homogeneous, neutrally stratified and without vertical velocities and got the solution:

$$\overline{u}_o = \frac{{u_{*,o}}^2}{\sqrt{K_m f}} \left[1 - e^{z/D} \cos\left(\frac{z}{D} - \frac{\pi}{4}\right)\right] , \tag{1.4}$$

$$\overline{v}_o = \frac{{u_{*,o}}^2}{\sqrt{K_m f}} \left[e^{z/D} \sin\left(\frac{z}{D} - \frac{\pi}{4}\right)\right] . \tag{1.5}$$

The turbulent diffusion coefficient of momentum K_m is part of the gradient transport theory which is chosen for the parametrization of turbulent fluxes (e.g. Stull, 1988). $u_{*,o}$ denotes the friction velocity of the ocean and is connected to the surface stress τ and the friction velocity of the atmosphere $u_{*,a}$ by the relation (Stull, 1988):

$$\tau = \rho_o {u_{*,o}}^2 = \rho_a {u_{*,a}}^2 . \tag{1.6}$$

ρ_o and ρ_a are the density of the ocean and the atmosphere, respectively. D is the Ekman length which is defined as (Ekman, 1905)[1]:

$$D = \sqrt{2\frac{K_m}{f}} . \tag{1.7}$$

As mentioned in section 1.1, the ABL can be divided in a Prandtl layer and an Ekman layer. The Prandtl layer ranges from the surface to a height z_P and the Ekman layer from z_P to the top of the ABL. For a constant geostrophic flow in the x-direction $|\vec{v}_g| = u_g$, the mean flow can be described in the Prandtl layer by (Etling, 2002):

$$\overline{u}_a = \frac{u_{*,a}}{\kappa} \ln\frac{z}{z_0} \cos\alpha , \tag{1.8}$$

$$\overline{v}_a = \frac{u_{*,a}}{\kappa} \ln\frac{z}{z_0} \sin\alpha , \tag{1.9}$$

and in the Ekman layer by:

$$\overline{u}_a = u_g \left[1 - \sqrt{2}\, exp\left(-\frac{z - z_P}{D}\right) \sin\alpha\ \cos\left(\frac{z - z_P}{D} + \frac{\pi}{4} - \alpha\right)\right] , \tag{1.10}$$

$$\overline{v}_a = u_g \left[\sqrt{2}\, exp\left(-\frac{z - z_P}{D}\right) \sin\alpha\ \sin\left(\frac{z - z_P}{D} + \frac{\pi}{4} - \alpha\right)\right] . \tag{1.11}$$

[1] Ekman (1905) and other oceanographic papers use the notation $a = \sqrt{2\frac{K_m}{f}}$ which is equal to D in this work and define the Ekman length as $D = \pi\sqrt{2\frac{K_m}{f}}$ which corresponds to the boundary layer depth z_i in the present work (see below).

α is the angle between the surface wind and the geostrophic wind. The depth of a wind driven OML and the height of the ABL z_i is defined by (Ekman, 1905):

$$z_i = \pi D \; . \tag{1.12}$$

The oceanic solution and the atmospheric solution result in a spiral for the velocity vector as a function of depth/height which is called Ekman spiral. In a wind driven ocean, the Ekman spiral extends from the sea surface down to the top of the thermocline. In the ABL, this spiral ranges from the top of the Prandtl layer to the top of the ABL (Stull, 1988; Etling, 2002; Stewart, 2008). Figure 1.1 shows vertical profiles of the horizontal velocity components u and v of a neutrally stratified Ekman layer driven by a geostrophic flow for a quasi-laminar and a turbulent Ekman flow. A quasi-laminar Ekman flow means that the turbulent diffusion coefficient K_m is constant with height while K_m varies with height in a turbulent Ekman flow. In case of a quasi-laminar flow (Fig. 1.1, left), the surface wind is turned to the left of the geostrophic flow at the top of the boundary layer by an angle of 45°. In a turbulent boundary layer (Fig. 1.1, right), the flow speed close to the surface is higher compared to the quasi-laminar flow and the angle of deflection α is smaller. In the atmosphere, α usually ranges between 15° and 25° (Etling, 2002).

The ideal Ekman solution is based on a number of assumptions and hence differs from real flows in the ABL and OML. Prandtl and Tollmien (1924) first noted that the turbulent diffusion coefficient K_m is not constant within the whole boundary layer due to stratification and vertical wind shear. Other effects, which are not considered by the ideal Ekman solution, are surface convection and gravity waves (e.g. Zikanov et al., 2003). However, the Ekman solution is adequate for nearly neutrally stratified boundary layers (Stull, 1988).

1.4. Roll vortices and flow instabilities

1.4.1. General information

Under certain conditions, organized large eddies with horizontally oriented axes, which are called roll vortices or rolls, occur in the ABL and OML. Roll vortices can be visible by cloud streets in the atmosphere, schematically sketched in figure 1.2, and by lines of seaweed in the ocean (Brown, 1980; Etling and Brown, 1993). An air parcel that moves with the mean wind along the roll axis has a spiral trajectory. The wavelength of the roll vortices λ_r includes two counter-rotating vortex rolls. H denotes the vertical extension of a roll vortex and ϵ the angle between the roll axis and the geostrophic flow (band orientation angle). A positive ϵ refers to a roll axis oriented to the left and a negative value to the right of the geostrophic flow. Roll vortices may play an important role in the vertical transport of momentum, heat, moisture and solutes in the ABL and OML (Etling and Brown, 1993).

Roll vortices develop due to three different flow instability mechanisms: thermal instability (also called convective instability), inflection point instability (IPI, see section 1.4.2) and parallel instability (PI, see section 1.4.3). The IPI and PI are dynamical instability mechanism (e.g. Etling and Brown, 1993). To determine responsible instability mechanisms of the roll vortices, an energy budget equation can be calculated for the rolls. Therefore, the flow components u_i

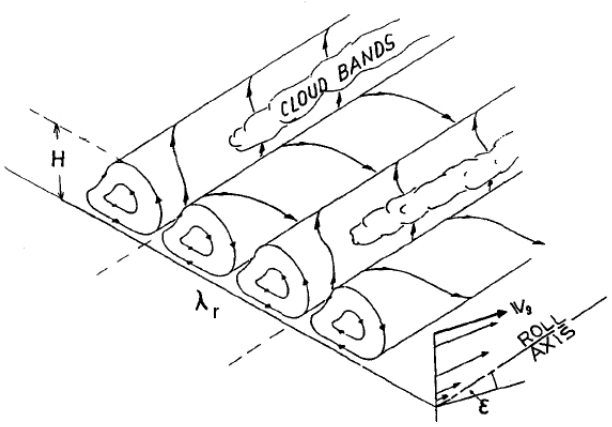

Figure 1.2.: Schematic representation of horizontal roll vortices in the ABL. H denotes the vertical extension and λ_r the wavelength of the roll vortices. The band orientation angle ϵ is the angle between the roll axis and the geostrophic flow $\vec{v}_g$ (after Etling and Brown, 1993).

are divided in a mean value $\overline{u}_i$ and a disturbance u_i^*

$$u_i = \overline{u}_i + u_i^* \; . \tag{1.13}$$

u_i^* includes the whole turbulence. Thus, if rolls develop within the flow, u_i^* contains the roll vortices. The averaged energy budget equation for the kinetic energy of the disturbance $e^* = u_i^{*2}/2$ is derived from the energy budget equation of the averaged kinetic energy per unit mass $\overline{u_i^2/2}$ and the energy budget equation of the averaged flow $\overline{u}_i^2/2$.
For the energy budget equation of the averaged kinetic energy, the Navier-Stokes equations are Boussinesq-approximated which leads to an incompressible flow with $\partial u_k/\partial x_k = 0$ (see section 2.3). Furthermore, the equations are multiplied with the velocity u_i and Reynolds averaged (e.g. Stull, 1988), which yields to:

$$\begin{aligned}
\frac{\partial}{\partial t}\frac{\overline{u}_i{}^2}{2} + \frac{\partial \overline{e^*}}{\partial t} + \frac{\partial}{\partial x_k}\left(\overline{u}_k\frac{\overline{u}_i{}^2}{2}\right) + \frac{\partial\left(\overline{u}_k\overline{e^*}\right)}{\partial x_k} + \frac{\partial}{\partial x_k}\left(\overline{u_i}\,\overline{u_k^* u_i^*}\right) + \frac{\partial \overline{u_k^* e^*}}{\partial x_k} \\
= \delta_{i3}\frac{g}{\theta_0}\overline{\theta}\overline{u}_i + \delta_{i3}\frac{g}{\theta_0}\overline{u_i^*\theta^*} - \epsilon_{ijk}f_j\overline{u}_i\overline{u}_k - \epsilon_{ijk}f_j\overline{u_i^* u_k^*} - \frac{1}{\rho_0}\overline{u}_i\frac{\partial\overline{p}}{\partial x_i} - \frac{1}{\rho_0}\frac{\partial\overline{u_i^* p^*}}{\partial x_i} \\
+ \nu_m\frac{\partial^2}{\partial x_k^2}\frac{\overline{u}_i{}^2}{2} + \nu_m\frac{\partial^2\overline{e^*}}{\partial x_k^2} - \nu_m\left(\frac{\partial\overline{u}_i}{\partial x_k}\right)^2 - \nu_m\overline{\left(\frac{\partial u_i^*}{\partial x_k}\right)^2} \; .
\end{aligned} \tag{1.14}$$

u_i are the velocity components u, v and w in the spatial directions x_i with the components x, y and z. The indices i, j and $k \in \{1, 2, 3\}$ denotes one of the three components of a quantity. t denotes the time, p the pressure and g the acceleration of gravity. The operator ∂ defines the partial derivative, δ_{ij} the Kronecker delta and ϵ_{ijk} the Levi-Civita symbol (also called alternating or permutation symbol). θ symbolizes the potential temperature and ν_m the molecular or kinematic viscosity. Quantities with an index 0 are related to the basic state of the Boussinesq approximation (see section 2.3).

An equation for the kinetic energy of the averaged flow $\overline{u}_i^2/2$ can be obtained by the averaged

Navier-Stokes equations multiplied with u_i:

$$\frac{\partial}{\partial t}\frac{\overline{u}_i{}^2}{2} + \frac{\partial}{\partial x_k}\left(\overline{u}_k\frac{\overline{u}_i{}^2}{2}\right) + \frac{\partial}{\partial x_k}\left(\overline{u_i}\,\overline{u_k^* u_i^*}\right)$$
$$= \delta_{i3}\frac{g}{\theta_0}\overline{\theta}\overline{u}_i - \epsilon_{ijk}f_j\overline{u}_i\overline{u}_k - \frac{1}{\rho_0}\overline{u}_i\frac{\partial\overline{p}}{\partial x_i} + \nu_m\frac{\partial^2}{\partial x_k^2}\frac{\overline{u}_i{}^2}{2} - \nu_m\left(\frac{\partial\overline{u}_i}{\partial x_k}\right)^2 + \overline{u_k^* u_i^*}\frac{\partial\overline{u}_i}{\partial x_k}\,. \quad (1.15)$$

A budget equation for the disturbance energy e^* is derived by subtracting equation 1.15 from equation 1.14:

$$\frac{\partial\overline{e^*}}{\partial t} + \frac{\partial\left(\overline{u}_k\overline{e^*}\right)}{\partial x_k} + \frac{\partial\overline{u_k^* e^*}}{\partial x_k} + \frac{1}{\rho_0}\frac{\partial\overline{u_i^* p^*}}{\partial x_i} + \epsilon_{ijk}f_j\overline{u_i^* u_k^*} - \nu_m\frac{\partial^2\overline{e^*}}{\partial x_k^2}$$
$$= -\overline{u_k^* u_i^*}\frac{\partial\overline{u}_i}{\partial x_k} + \delta_{i3}\frac{g}{\theta_0}\overline{u_i^*\theta^*} - \nu_m\overline{\left(\frac{\partial u_i^*}{\partial x_k}\right)^2}\,. \quad (1.16)$$

On the left hand side of equation 1.16 are the local change of disturbance energy, divergence terms, the Coriolis term and the diffusion term. On the right hand side are production and dissipation terms. The term $-\overline{u_k^* u_i^*}\,\partial\overline{u}_i/\partial x_k$ refers to the IPI where shear of the mean flow produces kinetic energy of the disturbance. $\delta_{i3}\,g/\theta_0\,\overline{u_i^*\theta^*}$ represents energy production or destruction by buoyancy forces (convective instability). $-\nu_m\,\overline{\left(\partial u_i^*/\partial x_k\right)^2}$ destroys perturbation energy by molecular processes.
If the x-axis is oriented along the roll axis and e^* is the roll energy, equation 1.16 can be split into an along-roll component $e_\parallel^* = u^{*2}/2$ and a cross-roll component $e_\perp^* = \left(v^{*2} + w^{*2}\right)/2$, perpendicular to the roll axis (e.g. Brümmer, 1985):

$$\frac{\partial}{\partial t}\overline{e_\parallel^*} = -\overline{w^* u^*}\frac{\partial\overline{u}}{\partial z} + f\overline{u^* v^*} - f^*\overline{u^* w^*} + OT\,, \quad (1.17)$$

$$\frac{\partial}{\partial t}\overline{e_\perp^*} = -\overline{w^* v^*}\frac{\partial\overline{v}}{\partial z} - f\overline{u^* v^*} + f^*\overline{u^* w^*} + OT\,. \quad (1.18)$$

The abbreviation OT (other terms) represents all terms which are not investigated in this study. The Coriolis force exchanges roll energy from the parallel component $e_\parallel^*$ to the perpendicular component $e_\perp^*$ and vice versa. Thus, the Coriolis force enhances or reduces roll vortices but cannot develop roll vortices by its own. This process is known as PI (Lilly, 1966).

Roll vortices are frequently observed phenomena and a large volume of published studies analyzing roll vortices in the atmosphere by observational data exist. They cannot all be mentioned in this work but some important results should be presented in the following. For a detailed overview of observations, it should be referred to the review paper of Brown (1980), Etling and Brown (1993) and Young et al. (2002).
Data from aircraft and tower measurements over land were analyzed by LeMone (1973, 1976). The observed rolls had a wavelength λ_r between 1.5 km and 6 km and ϵ ranged between 10° and 20°. The rolls occurred with moderately strong winds ($\vec{v}_g$ at the top of the boundary layer ranged between $8\,\mathrm{m\,s^{-1}}$ and $16\,\mathrm{m\,s^{-1}}$) and slightly convective conditions. Walter and Overland (1984) used satellite pictures and aircraft measurements to investigate roll vortices over

the ice-covered Bering Sea. Under nearly neutrally conditions, several scales of superimposing roll vortices developed during the study. They stated that rolls induced by the inflection point instability have a band orientation angle between 16° and 18° and a wavelength between 1.3 km and 6 km. Brümmer (1985) examined roll vortices under strong wind conditions ($\vec{v}_g \approx 19\,\mathrm{m\,s^{-1}}$) with data collected by aircraft measurements over the North Sea. The observed rolls were caused by the IPI on two days and by the convective instability on the other day. For the IPI induced rolls, the average wavelength was 1 km and for the convective case the wavelength was 700 m. The data analysis showed a significant contribution of the rolls to the vertical transport and hence they reduce the mean vertical gradients of temperature, moisture and horizontal velocity.
Weckwerth et al. (1997) studied roll structures under convective conditions by radar measurements and numerical simulations. They showed that a minimum wind speed of $5.5\,\mathrm{m\,s^{-1}}$ is necessary for the development of rolls. Otherwise a cellular or unorganized convection arise. Rolls under convective conditions were studied into more detail by Drobinski et al. (1998). They summarized that there are three regimes of large eddy circulation in the ABL. In the pure convection case, cells without a characteristic horizontal direction occur. If the ambient wind increases up to $3\,\mathrm{m\,s^{-1}}$, cells are replaced by rolls. Wind speeds of $5\,\mathrm{m\,s^{-1}}$ or higher form rolls which are indistinguishable with roll vortices in a neutrally stratified ABL.
Chen et al. (2001) supposed from observations with aircraft measurements and satellite pictures that atmospheric rolls dominate the momentum fluxes above the sea surface. They suggested that darkened sea surface streaks correspond to updraft areas of atmospheric roll vortices. However, the study does not show if roll vortices increase the momentum fluxes.

1.4.2. Inflection point instability

The IPI produces roll energy by shear of the mean flow. Therefore, an inflection point has to be in the vertical profile of the mean velocity which is connected to a vorticity extremum in the same height. The inflection point is in the velocity component perpendicular to the roll axis.

Faller (1963) constructed an experiment with a rotating water tank to study the IPI of an Ekman flow. Data analysis and theoretical studies with the linear perturbation theory showed that rolls caused by the IPI have a wavelength λ_r of approximately $11D$ and a band orientation angle ϵ between 10° and 15°. However, quasi-laminar Ekman flows were used in these studies (Faller, 1965; Faller and Kaylor, 1966; Lilly, 1966; Etling, 1971; Brown, 1972; Etling and Wippermann, 1975; Stensrud and Shirer, 1988; Aelbrecht et al., 1999)[2].
The IPI was identified in observational studies by the vertical profiles of the velocity component or by calculating the energy budget terms. Rolls in the atmosphere caused by the IPI have wavelengths up to 6 km and a band orientation angle between 10° and 20° (e.g. LeMone, 1973, 1976; Walter and Overland, 1984; Brümmer, 1985).
Further investigations were made with direct numerical simulations (DNS) and large-eddy simulations (LES) by Deardorff (1972), Mason and Thomson (1987), Coleman et al. (1990) and Moeng and Sullivan (1994). These simulations did not find roll vortices within the model domain but streaks. Streaks are near surface linear bands with smaller horizontal and vertical

[2]In some studies the rolls caused by the IPI are denoted as 'type I'.

extension as roll vortices (e.g. Young et al., 2002; Drobinski and Foster, 2003). Foster (1997) suggested that the dependence of the flow structure on model domain size and grid resolution could be responsible for the absence of roll structures in the three-dimensional DNS and LES results. The greatest model extension was 5 km in the horizontal direction in Moeng and Sullivan (1994) while the observed wavelengths are up to 6 km. Glendening (1996) conducted an LES with strong wind shear and weak buoyancy. He used a model domain of 25 km × 18 km and a simulation time of 16 h and found roll vortices with a wavelength of 3.5 km.
As mentioned in the previous section, rolls caused by IPI do not only occur in neutrally stratified flows but also in slightly convective boundary layers together with the convective instability (e.g. Etling and Brown, 1993; Weckwerth et al., 1997; Drobinski et al., 1998).

1.4.3. Parallel instability

The PI does not produce roll energy on its own but intensifies or reduces the roll vortices. As shown by equations 1.17 and 1.18, the Coriolis force exchanges roll energy between the along-roll and cross-roll components of the roll energy. The rolls are intensified if the energy is transported from the along-roll to the cross-roll component, a reverse exchange reduces the roll intensity.

The PI was found and termed by Lilly (1966) in his theoretical study based on the laboratory experiment by Faller (1963)[3]. Experimental and theoretical studies indicated that roll vortices affected by the PI have a wavelength $\lambda_r \approx 19D$ and a band orientation angle between $0°$ and $-20°$ (Lilly, 1966; Faller and Kaylor, 1966; Etling, 1971; Aelbrecht et al., 1999). However, calculation of energy budget terms from observational data of the atmosphere could not verify the influence of the PI at mid-latitudes (e.g. LeMone, 1973; Brümmer, 1985). Brümmer (1985) supposed an effect of the Coriolis force on the rolls near the equator caused by the vertical Coriolis force. A strong influence of the vertical Coriolis force on the flow stability was first assumed by Wippermann (1969). Etling (1971) pointed out that an easterly flow is more unstable than a westerly flow if the vertical Coriolis force is considered[4]. Extensive studies of the influence of the vertical Coriolis force on the flow stability were conducted by Leibovich and Lele (1985). Using linear perturbation theory, they examined the flow stability for different latitudes and wind directions for the atmosphere and the ocean. Their results showed a maximum instability for easterly flows and a minimum instability for westerly flows. This difference is increasing with a decreasing latitude. Coleman et al. (1990) used DNS to investigate the effect of the vertical Coriolis force and confirmed the result of Leibovich and Lele (1985). However, Coleman et al. (1990) did not observe roll vortices and showed that the difference of the flow stability between a westerly and an easterly flow is caused by the unorganized turbulence. Using LES, Glazunov (2010) observed roll vortices in a neutrally stratified atmospheric flow. He showed that the development of roll vortices depends on latitude and wind direction comparable to the unorganized turbulence. Glazunov (2010) calculated the contribution of the roll vortices on the vertical momentum transport in easterly and northeasterly wind regimes to approximately 40 %. Furthermore, he showed that under stable conditions the effect of the vertical Coriolis force and hence the PI vanishes, which was previously presumed by Dubos et al. (2008) and Gerkema et al. (2008). Esau (2003) analyzed LES data with the proper

[3] In some studies the rolls caused by the PI are denoted as 'type II'.
[4] Neglecting the vertical Coriolis component is also called the 'f-plane' approximation.

orthogonal decomposition (POD) method[5] and concluded that the Coriolis effect is strong in neutrally stratified shear-driven geophysical flows and weak in buoyancy driven flows.
LES studies for a wind driven OML by Zikanov et al. (2003) showed an increasing turbulence production at lower latitudes caused by the vertical Coriolis force and a maximum of the effect for a northwest wind. (The angle of the wind direction γ should be replaced by $-\gamma$ for a correct reading of the paper by Zikanov et al. (2003). Therefore, the terms "west" and "east" should be interchanged in their text. This circumstance was already recognized by Gerkema et al. (2008).) Zikanov et al. (2003) could not observe roll vortices in their data and showed, comparable to Coleman et al. (1990) for the atmosphere, that the influence of the vertical Coriolis force on the unorganized turbulence is responsible for the increasing turbulence production at lower latitudes.

1.5. Motivation and scope of this study

The present work examines the influence of atmospheric roll vortices on wind driven oceanic flows with the aid of LES. Roll vortices are responsible for a large amount of turbulent transport within the ABL and OML and therefore are of interest for the flow structure of the boundary layers. This thesis deals with the question if atmospheric roll vortices induce coherent circulations within the OML.
For reasons of simplification, the roll vortices are studied in a neutrally stratified Ekman flow. I. N. Esau (2009, personal communication) and Glazunov (2010) investigated such a flow and observed that the development of roll vortices depends on latitude and wind direction due to the variability of the vertical Coriolis force. In detail, roll vortices develop in easterly flows but not in westerly flows. For easterly flows, the organization of the turbulence in roll vortices increases with decreasing latitude.
Starting from this point of research, a parameter study is carried out which investigates the effect of wind direction and latitude. The results of the parameter study are compared with earlier investigations for developing a setup for a coupled atmosphere-ocean simulation. For a better understanding of the underlying mechanisms of the roll development, the energy budget terms of the IPI and the PI are analyzed.
LES studies of an Ekman flow in the OML were made for example by Zikanov et al. (2003) and Noh et al. (2004). Noh et al. (2004) investigated the effect of wave-breaking and Langmuir circulation and used a reference case without these effects. The reference case is used by this study for a model validation. Zikanov et al. (2003) examined the influence of the wind direction and latitude on the instability of a wind driven Ekman flow within the OML and observed that the vertical momentum transport by unorganized turbulence shows a maximum for a north-east wind and a minimum for a south-west wind. The difference of vertical momentum transport between the wind directions is zero at the poles and increases with lower latitudes. This effect is also present for the unorganized turbulence in the atmosphere (Leibovich and Lele, 1985; Coleman et al., 1990) and caused by the vertical Coriolis force. Hence, it is assumed that the IPI and PI also induces roll vortices in the OML, as in the atmospheric case. However, Zikanov et al. (2003) did not observe large coherent structures in their data. This may be caused by the used grid length which is of the order of 10 m. Noh et al. (2004) used a grid length of 1.25 m for investigations of the Langmuir circulation which shows that this grid length is sufficiently large to resolve large coherent structures with wavelengths of 100 m. In

[5] A detailed description of the POD is given in Berkooz et al. (1993).

the current study, the ocean is simulated with the grid length based on the study by Noh et al. (2004) to investigate if rolls develop within the OML by dynamical instability mechanisms. To study the influence of the atmospheric roll vortices on the OML, a coupled atmosphere-ocean simulation is carried out. The coupled simulation considers the different length scales of atmosphere and ocean. For resolving the roll vortices in atmosphere and ocean, the horizontal model domain size has to be of the order of several kilometers due to atmospheric roll vortices, while the ocean model needs a grid resolution of a few meters for resolving large coherent structures. The coupled simulation shall answer the question if atmospheric roll vortices can induce large coherent structures with wavelengths of several kilometers in the OML. To the authors knowledge, this has not been done before.

This work is structured as follows: The LES model PALM (PArallelized Large-eddy simulation Model), used for all simulations of the present study, is introduced in chapter 2 with the underlying equations. The chapter also contains detailed information about the coupling between atmosphere model and ocean model. The simulation setups and results are presented and analyzed in chapter 3, which is divided into three sections: Atmospheric simulations, oceanic simulations and coupled atmosphere-ocean simulation. A summary and final conclusions are given in the last chapter.

2. PALM - A Parallelized Large-Eddy Simulation Model

All simulations were carried out using the parallelized LES model PALM which is designed for simulations of turbulent flows in the atmospheric boundary layer and the ocean boundary layer. It has been developed at the Institute for Meteorology and Climatology (IMUK) at the Leibniz University of Hannover for parallel computing (Raasch and Schröter, 2001, and references therein) and has been written in `Fortran 95` [1].

This chapter provides an overview of the underlying equations and parts of the used numerical and physical model features. General information about modeling of turbulent flows and an outline of the LES technique are given in section 2.1. Section 2.2 includes the basic equations and section 2.3 the Boussinesq approximation. The main idea of LES is the separation of the larger and smaller scale turbulence with a filter (section 2.4). Thereby, the smaller scale turbulence has to be parameterized (section 2.5) and the larger scale turbulence is explicitly resolved. Section 2.6 contains information on the spatial and temporal discretization. In order to solve the model equations, specific initialization parameters and boundary conditions must be declared and are described in section 2.7. For the initialization state of the three-dimensional model, PALM provides a one-dimensional precursor run (section 2.8).
Section 2.9 deals with the ocean model and section 2.10 with the coupling between the atmosphere model and the ocean model.
The chapter closes by an overview of the parallelization method of PALM and hints for an optimized using of the coupling.

2.1. Modeling of turbulent flows

Reynolds (1883) introduced a measure to distinguish between laminar and turbulent flows, the so called Reynolds number:

$$Re = \frac{UL}{\nu_m} \, . \tag{2.1}$$

Re is defined as the ratio of inertial to viscous forces. U and L are typical velocity and length scales of the boundary layer flow and ν_m the kinematic viscosity of a flow (Stull, 1988). A flow becomes turbulent if it exceeds a critical value Re_c which is about 1×10^4 (Thorpe, 2005). Typical values are for the ABL $L = 1000\,\mathrm{m}$, $U = 1\,\mathrm{m\,s^{-1}}$ and $\nu_m = 1 \times 10^{-5}\,\mathrm{m^2\,s^{-1}}$ and for the OML $L = 100\,\mathrm{m}$, $U = 0.01\,\mathrm{m\,s^{-1}}$ and $\nu_m = 10^{-6}\,\mathrm{m^2\,s^{-1}}$ (Etling, 2002; Thorpe, 2005). Thus, $Re \approx 1 \times 10^8$ in the ABL and $Re \approx 1 \times 10^6$ in the OML.

Figure 2.1 shows the spectrum of the turbulent kinetic energy (TKE) of a boundary layer flow as a function of the eddy wavenumber k. It illustrates that the larger eddies (smaller wavenumbers) contain the bulk of the TKE. The spectrum of the TKE is divided into three wavelength spans: the production range P, the inertial subrange I and the dissipation range D.

[1] For an online documentation of PALM see http://palm.muk.uni-hannover.de

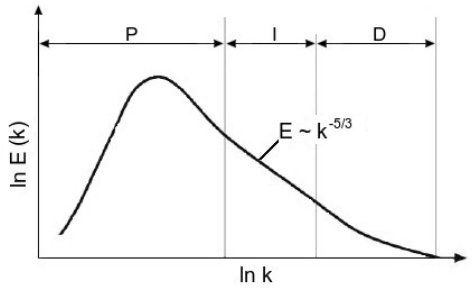

Figure 2.1.: Schematic representation of the spectrum of TKE as a function of the wavenumber k. P represents the production range, I the inertial subrange and D the dissipation range (after Kraus, 2008).

The production range includes smaller wavenumbers and TKE is produced by buoyancy and shear, where the latter extracting energy from the mean flow (Stull, 1988). In the range of the smallest eddies (largest wavenumbers), TKE is converted into heat by viscous dissipation. The length scale of the smallest eddies is called the Kolmogorov microscale

$$\eta = \left(\frac{\nu_m^3}{\epsilon} \right)^{1/4} . \tag{2.2}$$

ϵ is the viscous dissipation rate of TKE. With $\nu_m = 1.5 \times 10^{-5}\,\mathrm{m^2\,s^{-1}}$ and $\epsilon \approx 0.01\,\mathrm{m^2\,s^{-3}}$ close to the surface, the Kolmogorov length scale results into $\eta \approx 1\,\mathrm{mm}$ for the smallest eddies (Stull, 1988; Garratt, 1992). In the inertial subrange, larger eddies decay more and more into smaller eddies which transports energy into the dissipation range. This process is known as the energy cascade. The decrease of energy satisfy the relation

$$E(k) = \alpha_k \, \epsilon^{2/3} \, k^{-5/3} , \tag{2.3}$$

which is well known as Kolmogorov's minus five-third law. $E(k)$ depends on the constant $\alpha_k \approx 1.5$ (from experimental data), the dissipation rate ϵ and the wavenumber k (Tennekes and Lumley, 1972).

Basically, three different approaches exist to model a turbulent flow which can be distinguished by the rate of resolved turbulence: DNS, LES and RANS (Reynolds-averaged Navier-Stokes simulations). DNS directly solves the Navier-Stokes equations on a grid which resolves all scales of eddies. Therefore, the grid has to be fine enough to resolve eddies of the order of the Kolmogorov length scale η and the model domain size has to be sufficiently large to resolve the largest eddies in the flow. The number of grid points N can be estimated by the Reynolds number of the flow or by the ratio of the characteristic length scales of the largest and smallest eddies:

$$N \sim \frac{L}{\eta} \sim Re^{3/4} , \tag{2.4}$$

which relates to one spatial direction (Fröhlich, 2006). For a three-dimensional turbulent flow in the ABL with a typical Reynolds number of $Re = 10^8$, as shown above, the number of grid points is estimated to:

$$N^3 \sim \left(Re^{3/4} \right)^3 \sim Re^{9/4} \sim 10^{18} . \tag{2.5}$$

Today's supercomputers can handle simulations with a number of grid points of the order of 10^{11} which is seven magnitudes below the required grid points. For this reason, DNS models are used only for turbulent flows with small Reynolds numbers.

RANS models average the Navier-Stokes equations with a Reynolds-average by separating all quantities ψ in a mean $\overline{\psi}$ and a statistical deviation ψ' (Fröhlich, 2006):

$$\psi = \overline{\psi} + \psi' \, . \tag{2.6}$$

After the replacement, the Navier-Stokes equations are ensemble-averaged and solved only for the statistical mean. The whole turbulence is included in ψ' and predicted by a turbulence model. Hence, RANS models can be used for flows with high Reynolds numbers because they need less computational time compared to DNS and LES models. The disadvantage is the high dependence on the turbulence model which is not universally for all flows (Fröhlich, 2006). The parameterization of the entire turbulence spectrum makes RANS models unsuitable for turbulence studies.

The idea of LES is a combination of DNS and RANS techniques in such a way that the advantages of both are used. To achieve this, the turbulence spectrum is divided into a part containing the larger scale turbulence and a part including the smaller scale turbulence, which is known as filtering (see section 2.4). The larger scales are explicitly resolved and the smaller eddies are parameterized with a so called subgrid-scale model (SGS, section 2.5). This approach is adequate because the larger eddies contain the bulk of TKE and depend on the geometry. The smaller eddies have a small amount of TKE and are isotropic after the theory of Kolmogorov (1941). The isotropic character of the smaller scales simplifies the parameterization in an LES model compared to a RANS model where the whole turbulence must be parameterized.
The advantage of LES is the possibility of a coarser grid compared to DNS. Thus, LES models can simulate the turbulence in flows with high Reynolds numbers with today's supercomputers and they are a powerful tool for studies of geophysical flows. Difficulties of LES, apart from numerical and discretization errors, exist in regions where the parameterized small eddies dominate. For detailed information on the LES technique, it shall be referred to Fröhlich (2006).

2.2. Basic equations of turbulent flows

The dynamics of a turbulent flow can be described by a set of prognostic equations. For a rotating Cartesian coordinate system, these equations can be written in tensor notation as follows:

$$\frac{\partial u_i}{\partial t} = -u_k \frac{\partial u_i}{\partial x_k} - \epsilon_{ijk} f_j u_k - \frac{1}{\rho} \frac{\partial p}{\partial x_i} - g\delta_{i3} + \nu_m \left(\frac{\partial^2 u_i}{\partial x_k^2} + \frac{1}{3} \frac{\partial}{\partial x_i} \frac{\partial u_k}{\partial x_k} \right) \tag{2.7}$$

for the conservation of momentum (Navier-Stokes equations),

$$\frac{\partial \rho}{\partial t} = -\frac{\partial (u_i \rho)}{\partial x_i} \tag{2.8}$$

for the conservation of mass (continuity equation),

$$\frac{\partial \theta}{\partial t} = -u_k \frac{\partial \theta}{\partial x_k} + \nu_h \frac{\partial^2 \theta}{\partial x_k^2} + Q_h \tag{2.9}$$

representing the conservation of heat (first law of thermodynamics) and

$$\frac{\partial s}{\partial t} = -u_k \frac{\partial s}{\partial x_k} + \nu_s \frac{\partial^2 s}{\partial x_k^2} + Q_s \tag{2.10}$$

for the conservation of scalar quantities. s symbolizes any scalar with or without an impact on the flow. $\nu_m,\ \nu_h,\ \nu_s$ are the molecular viscosities related to momentum, temperature and scalar quantities, respectively. $Q_h,\ Q_s$ are source and sink terms for the potential temperature and the scalar quantities, respectively.
Equations 2.7 - 2.10 form a system of nonlinear partial differential equations which can only be solved numerically. The used approximations of PALM are presented in the following sections.

2.3. Boussinesq approximation

The Boussinesq approximation simplifies the Navier-Stokes equations 2.7 and is commonly used for the description of phenomena in boundary layer meteorology (Etling, 2002). Local values of density, pressure and temperature (represented by the universal variable Ψ) are divided into a basic state ψ_0 and a deviation ψ^* of this (e.g. Etling, 2002):

$$\psi(x,y,z,t) = \psi_0(z) + \psi^*(x,y,z,t)\ . \tag{2.11}$$

The deviations ψ^* depend on space and time. The basic states ψ_0 only depend on altitude by definition, except the pressure. A constant horizontal pressure gradient is allowed and expressed by the geostrophic flow:

$$\frac{\partial p_0(x,y,z)}{\partial x} = f\rho_0 v_g \quad \text{and} \quad \frac{\partial p_0(x,y,z)}{\partial y} = -f\rho_0 u_g\ . \tag{2.12}$$

Furthermore, the basic state fulfills the hydrostatic equation

$$\frac{\partial p_0(z)}{\partial z} = -g\rho_0(z) \tag{2.13}$$

and the ideal gas law

$$p_0 = \rho_0 R T_0\ . \tag{2.14}$$

R is the ideal gas constant.
Multiplying equation 2.7 with ρ and using equation 2.11 yields to:

$$\begin{aligned}\rho_0 \left(1 + \frac{\rho^*}{\rho_0}\right)\left(\frac{\partial u_i}{\partial t} + u_k \frac{\partial u_i}{\partial x_k} + \epsilon_{ijk} f_j u_k\right) = &-\frac{\partial p_0}{\partial x_i} - \frac{\partial p^*}{\partial x_i} - \rho_0 g \delta_{i3} - \rho^* g \delta_{i3} \\ &+ \rho_0 \left(1 + \frac{\rho^*}{\rho_0}\right)\left(\nu_m \left(\frac{\partial^2 u_i}{\partial x_k^2} + \frac{1}{3}\frac{\partial}{\partial x_i}\frac{\partial u_k}{\partial x_k}\right)\right)\end{aligned} \tag{2.15}$$

The deviations are presumed to be small compared to the basic states, $\psi^* << \psi_0$ and $\psi^*/\psi_0 << 1$. For that reason, all terms including ρ^* are eliminated except for the buoyancy term. The vertical derivation of the first term and the third term, both on the right-hand side of equation 2.15, cancel each other with 2.13. The horizontal derivations of the first term on the right-hand side can be replaced as shown in equation 2.12. Thus, equation 2.15 can be written as:

$$\frac{\partial u_i}{\partial t} = -u_k \frac{\partial u_i}{\partial x_k} - \epsilon_{ijk} f_j u_k + \epsilon_{i3k} f_3 u_{g_k} - \frac{1}{\rho_0}\frac{\partial p^*}{\partial x_i} - \frac{\rho^*}{\rho_0} g \delta_{i3} + \nu_m \left(\frac{\partial^2 u_i}{\partial x_k^2} + \frac{1}{3}\frac{\partial}{\partial x_i}\frac{\partial u_k}{\partial x_k} \right) . \quad (2.16)$$

Because density measurements are difficult, the density ratio in the buoyancy term can be replaced by the temperature ratio which can be derived from the logarithmic differentiation of the ideal gas law with the assumptions $\Delta\psi = \psi - \psi_0 = \psi^*$, $p^*/p_0 \ll \rho^*/\rho_0$ and $T^*/T_0 \approx \theta^*/\theta_0$:

$$\frac{dp}{p} = \frac{d\rho}{\rho} + \frac{dT}{T} \Rightarrow \frac{\Delta p}{p} \approx \frac{\Delta\rho}{\rho} + \frac{\Delta T}{T} \Rightarrow \frac{\Delta\rho^*}{\rho_0} - \frac{\Delta p^*}{p_0} \approx -\frac{\Delta T^*}{T_0} \Rightarrow \frac{\Delta\rho^*}{\rho_0} \approx -\frac{\Delta\theta^*}{\theta_0} . \quad (2.17)$$

Replacing the density ration in equation 2.16 leads to:

$$\frac{\partial u_i}{\partial t} = -u_k \frac{\partial u_i}{\partial x_k} - \epsilon_{ijk} f_j u_k + \epsilon_{i3k} f_3 u_{g_k} - \frac{1}{\rho_0}\frac{\partial p^*}{\partial x_i} + \frac{\theta^*}{\theta_0} g \delta_{i3} + \nu_m \left(\frac{\partial^2 u_i}{\partial x_k^2} + \frac{1}{3}\frac{\partial}{\partial x_i}\frac{\partial u_k}{\partial x_k} \right) . \quad (2.18)$$

The advantages of the Boussinesq approximation are the simplification of the continuity equation 2.8 which is for small height intervals where $\partial\rho_0/\partial z \approx 0$ holds:

$$\frac{\partial u_i}{\partial x_i} = 0 . \quad (2.19)$$

The flow is incompressible after the Boussinesq approximation. Hence, sound waves are filtered which leads to the possibility of a larger time step in numerical models. More detailed information can be found in Etling (2002) and Stull (1988).

2.4. Filtering

As mentioned in section 2.1, the main idea of LES is the separation of the turbulence scales. Therefor, every quantity ψ is divided into a resolved part (grid-scale) $\overline{\psi}$ and an unresolved part (subgrid-scale) ψ'':

$$\psi = \overline{\psi} + \psi'' . \quad (2.20)$$

The resolved and unresolved part are separated by the so called filter width. In PALM, the method after Schumann (1975) is used:

$$\overline{\psi}(V,t) = \frac{1}{V}\int_V \psi(V',t)\, dV' , \quad (2.21)$$

with the grid volume

$$V = \left[x - \frac{\Delta x}{2}, x + \frac{\Delta x}{2}\right] \times \left[y - \frac{\Delta y}{2}, y + \frac{\Delta y}{2}\right] \times \left[z - \frac{\Delta z}{2}, z + \frac{\Delta z}{2}\right] . \quad (2.22)$$

In PALM, the filter width is equal to the grid length of the spatial discretization. Thus, the subgrid-scale turbulence is filtered by averaging over one grid box (volume average). This method is an implicit filtering (Fröhlich, 2006). The filtering after equation 2.21 has the same properties as a Reynolds operator which fulfills:

$$\overline{\overline{\psi}} = \overline{\psi} \ , \quad \overline{\psi''} = 0 \quad \text{and} \quad \overline{\psi\chi} = \overline{\psi}\overline{\chi} + \overline{\psi''\chi''} \ . \tag{2.23}$$

ψ and χ can be any atmospheric or oceanic quantity (Stull, 1988).

The application of Reynolds averaging to the Boussinesq approximated equations (Eq. 2.18, 2.19), the first law of thermodynamics (Eq. 2.9) and the conservation equation for scalar quantities (Eq. 2.10) leads to the filtered model equations of PALM:

$$\frac{\partial \overline{u}_i}{\partial t} = -\frac{\partial \overline{u}_k \overline{u}_i}{\partial x_k} - \epsilon_{ijk} f_j \overline{u}_k + \epsilon_{i3k} f_3 \overline{u}_{g_k} - \frac{1}{\rho_0}\frac{\partial \overline{p^*}}{\partial x_i} + \frac{\overline{\theta^*}}{\theta_0} g \delta_{i3} - \frac{\partial \tau_{ki}}{\partial x_k} \ , \tag{2.24}$$

$$\frac{\partial \overline{u}_i}{\partial x_i} = 0 \ , \tag{2.25}$$

$$\frac{\partial \overline{\theta}}{\partial t} = -\frac{\partial \overline{u}_k \overline{\theta}}{\partial x_k} - \frac{\partial \overline{u_k'' \theta''}}{\partial x_k} + Q_\theta \ , \tag{2.26}$$

$$\frac{\partial \overline{s}}{\partial t} = -\frac{\partial \overline{u}_k \overline{s}}{\partial x_k} - \frac{\partial \overline{u_k'' s''}}{\partial x_k} + Q_s \ . \tag{2.27}$$

The subgrid-scale terms are defined as follows:

$$\tau_{ki} = \overline{u_k'' u_i''} = \overline{u_k u_i} - \overline{u}_k \overline{u}_i \ , \quad \overline{u_k'' \theta''} = \overline{u_k \theta} - \overline{u}_k \overline{\theta} \quad \text{and} \quad \overline{u_k'' s''} = \overline{u_k s} - \overline{u}_k \overline{s} \ . \tag{2.28}$$

τ_{ki} is the subgrid-scale stress tensor and its components are velocity fluxes. $\overline{u_k'' \theta''}$ denotes the subgrid-scale flux for temperature and $\overline{u_k'' s''}$ for scalar quantities. These terms cannot be calculated explicitly and must be parameterized with a subgrid-scale model. The overbar marks a volume averaged quantity which contains the resolved part of turbulence and the double prime denotes the subgrid-scale portion of turbulence. The molecular diffusion is neglected in equation 2.24 because it is much smaller than the turbulent diffusion.

2.5. Subgrid-scale model

The filtered system of equations of PALM (Eq. 2.24 - 2.27) contains more unknowns than equations, which is known as the turbulence closure problem. To close the system of equations, the subgrid-scale fluxes are parameterized by resolved quantities in such a way that the impact of the smaller scales to the larger scales is well modeled. The model for the smaller scales has to provide enough dissipation to ensure that enough energy is transported from larger to smaller scales according to the energy cascade (Fröhlich, 2006). The parameterization in

PALM is realized according to Deardorff (1980). According to the gradient transport theory, the subgrid-scale fluxes can be written as:

$$\tau_{ki} = -K_m \left(\frac{\partial \overline{u}_i}{\partial x_k} + \frac{\partial \overline{u}_k}{\partial x_i} \right) , \tag{2.29}$$

$$\overline{u_k'' \theta''} = -K_h \frac{\partial \overline{\theta}}{\partial x_k} , \tag{2.30}$$

$$\overline{u_k'' s''} = -K_s \frac{\partial \overline{s}}{\partial x_k} . \tag{2.31}$$

K_m, K_h and K_s denote the subgrid-scale eddy coefficients or turbulent diffusion coefficients for momentum, heat and scalar quantities, respectively. The coefficient for momentum is calculated after the Prandtl-Kolmogorov hypothesis (Kolmogorov, 1942; Prandtl, 1945):

$$K_m = c_m l \sqrt{e} . \tag{2.32}$$

K_h and K_s are calculated by:

$$K_h = K_s = K_m \left(1 + \frac{2l}{\Delta} \right) . \tag{2.33}$$

$c_m = 0.1$ is the Smagorinsky constant, l denotes the mixing length, $\Delta = \sqrt[3]{\Delta x \Delta y \Delta z}$ is the characteristic grid length, which is equivalent to the filter width in PALM, and e denotes the subgrid-scale turbulent kinetic energy (SGS-TKE):

$$e = \frac{1}{2} \overline{u_i'' u_i''} . \tag{2.34}$$

The mixing length l is a measure of the ability of turbulence to cause mixing (Stull, 1988) and can be interpreted as the free path of the air molecules (Etling, 2002). The mixing length relates to the eddy size of the subgrid-scale eddies which are parameterized. l is directly related to the filter width Δ, the distance d from the bottom boundary or a wall and the stratification because the eddy sizes decrease with the increase of boundary layer stability. In PALM, the mixing length is calculated as follows:

$$l = \begin{cases} \min \left(\Delta,\ 0.7d,\ 0.76\sqrt{e} \left(\frac{g}{\theta_0} \frac{\partial \overline{\theta}}{\partial z} \right)^{-1/2} \right) & \text{if } \frac{\partial \overline{\theta}}{\partial z} > 0 , \\ \min \left(\Delta,\ 0.7d \right) & \text{if } \frac{\partial \overline{\theta}}{\partial z} \leq 0 . \end{cases} \tag{2.35}$$

The SGS-TKE e is calculated by a prognostic equation:

$$\frac{\partial e}{\partial t} = -\frac{\partial \overline{u}_k e}{\partial x_k} - \tau_{ki} \frac{\partial \overline{u_i}}{\partial x_k} + \frac{g}{\theta_0} \overline{u_3'' \theta''} - \frac{\partial}{\partial x_k} \left[\overline{u_k'' \left(e + \frac{p''}{\rho_0} \right)} \right] - \epsilon . \tag{2.36}$$

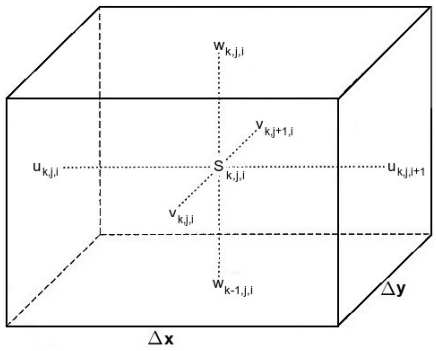

Figure 2.2.: Schematic representation of the numerical grid used in PALM (Arakawa-C grid). Scalar quantities s are defined at the center of the grid box and the velocity components u_i are shifted one half grid length $\Delta x_i/2$ in x_i-direction (after Sheng et al., 1998).

The model equations are closed with a parameterization of the turbulent transport of the SGS-TKE and the pressure variations:

$$\overline{u_k'' \left(e + \frac{p''}{\rho_0} \right)} = -2K_m \frac{\partial e}{\partial x_k} \, , \tag{2.37}$$

and for a parameterization of the dissipation rate ϵ:

$$\epsilon = \left(0.19 + 0.74 \frac{l}{\Delta} \right) \frac{e^{3/2}}{l} \, . \tag{2.38}$$

2.6. Discretization and numerical schemes

The prognostic model equations 2.24 - 2.27 and 2.36 must be discretized in space and time to solve them numerically. In PALM, this is done by the finite difference method where differential operators are approximated by finite differences ($\partial \approx \Delta$). A cartesian staggered grid, Arakawa-C grid, is used for the spatial discretization (Arakawa and Lamb, 1977). As illustrated in figure 2.2, scalar quantities are defined in the center of a grid volume V which is spanned by Δx, Δy and Δz (see Eq. 2.22). The velocity components are calculated at the sides of the grid boxes. Compared to the scalar quantities, the u component is shifted half a grid length in the negative x-direction, the v component half a grid length in the negative y-direction and the w component half a grid length in the positive z-direction.

The horizontal grid length is equidistant, whereas the vertical grid length Δz can be stretched with a constant stretch factor f_s to save computational time:

$$\Delta z(k+1) = f_s \cdot \Delta z(k) \;\; \forall \; k > k_s \, . \tag{2.39}$$

Stretching starts above a user-defined height level k_s and is intended for high levels above the ABL.

In this study, the advection terms are solved by the second-order advection-scheme of Piacsek and Williams (1970) and the time integration is done by a third-order Runge-Kutta scheme (RK3) (Williamson, 1980).

For the stability of the time integration, the dynamical time step Δt must fulfill the Courant-Friedrichs-Lewy (CFL) criterion (Courant et al., 1928):

$$\Delta t_{CFL} \leq \min\left(\frac{\Delta x_i}{\overline{u}_{imax}}\right) , \tag{2.40}$$

which ensures that information are not transported over more than one grid length during one time step. A further limitation of the dynamical time step is the diffusion criterion (Roache, 1985):

$$\Delta t_{diff} \leq \min\frac{1}{8}\left(\frac{\Delta x_i^2}{\max(K_m, K_h)}\right) . \tag{2.41}$$

To ensure stability, the final time step is reduced by a factor of 0.9:

$$\Delta t = 0.9 \cdot \min(\Delta t_{CFL}, \Delta t_{diff}) . \tag{2.42}$$

The time integrated equations of motion 2.24 are not necessarily free of divergence. Thus, the equations do not fulfill the continuity equation 2.25 for an incompressible flow. To ensure incompressibility, the fractional step method after Patrinos and Kistler (1977) is used which is based on a method of Chorin (1968). Due to the Boussinesq approximation, the perturbation pressure p^* is not coupled with the ideal gas law and is a pure dynamical pressure. Therefore, the term $-1/\rho_0 \cdot \partial\overline{p^*}/\partial x_i$ is used to get a divergence free velocity field. Neglecting the pressure term, a preliminary velocity field $\overline{u}_{i,pre}^{t+\Delta t}$ is calculated first, so that the prognosticated velocity field can be written as

$$\overline{u}_i^{t+\Delta t} = \overline{u}_{i,pre}^{t+\Delta t} - \frac{r_i \Delta t}{\rho_0}\frac{\partial \overline{p^*}^t}{\partial x_i} . \tag{2.43}$$

$r_i\Delta t$ is the fractional time step and ρ_0 the constant density with a value of $1\,\mathrm{kg\,m^{-3}}$. For RK3, tendency terms are calculated at the points $t^n + 1/3\Delta t$, $t^n + 3/4\Delta t$ and $t^n + \Delta t$ which leads to fractional time steps of $r_1\Delta t = 1/3\Delta t$, $r_2\Delta t = 5/12\Delta t$ and $r_3\Delta t = 1/4\Delta t$, respectively.

The prognosticated velocity field is free of divergence if it fulfills the continuity equation 2.25:

$$\frac{\partial \overline{u}_i^{t+\Delta t}}{\partial x_i} = \frac{\partial}{\partial x_i}\left(\overline{u}_{i,pre}^{t+\Delta t} - \frac{r_i \Delta t}{\rho_0}\frac{\partial \overline{p^*}^t}{\partial x_i}\right) \stackrel{!}{=} 0 . \tag{2.44}$$

Rearranging this equation leads to a Poisson equation for the perturbation pressure:

$$\frac{\partial^2 \overline{p^*}^t}{\partial x_i^2} = \frac{\rho_0}{r_i \Delta t}\frac{\partial \overline{u}_{i,pre}^{t+\Delta t}}{\partial x_i} . \tag{2.45}$$

The Poisson equation is solved with the Fast Fourier Transformation (FFT) algorithm in this study.

2.7. Initialization and boundary conditions

In order to solve the model equations numerically, initialization and boundary conditions must be set. These conditions should be similar to physical properties. The lateral boundary conditions are cyclic which means that in the horizontal directions the model domain repeats infinitely. The advantage of this method is that turbulence can freely develop.
The top and bottom boundary conditions and the initialization state are different for the ocean and the atmosphere. In the present section, the conditions for the atmosphere are given and the conditions of the ocean model are discussed in section 2.9. At the top boundary z_t of the model domain, Dirichlet boundary conditions are chosen for the velocity and the perturbation pressure:

$$\overline{u}(x,y,z_t) = u_g \ , \quad \overline{v}(x,y,z_t) = v_g \ , \quad \overline{w}(x,y,z_t) = 0 \ , \quad \overline{p^*}(x,y,z_t) = 0 \ . \tag{2.46}$$

Neumann conditions are selected for the TKE and the potential temperature, where the latter is constant in time:

$$e(x,y,z_t) = e(x,y,z_t - \Delta z) \ , \tag{2.47}$$

$$\left.\frac{\partial\overline{\theta}}{\partial z}\right|_{z_t,t} = \left.\frac{\partial\overline{\theta}}{\partial z}\right|_{z_t,t=0} \ . \tag{2.48}$$

The bottom edge of the atmosphere is limited by the earth's surface and the boundary conditions at the bottom of the model are orientated at its characteristics. At the bottom boundary $z_b = 0$, all quantities are defined at the same grid level contrary to the staggered grid levels above. Dirichlet boundary conditions are chosen for the velocity, potential temperature and scalar quantities:

$$\overline{u}(x,y,z_b) = 0 \ , \quad \overline{v}(x,y,z_b) = 0 \ , \quad \overline{w}(x,y,z_b) = 0 \ , \tag{2.49}$$

$$\overline{\theta}(x,y,z_b) = \overline{\theta}_{ini} \ , \quad \overline{s}(x,y,z_b) = \overline{s}_{ini} \ . \tag{2.50}$$

Neumann conditions are used for the perturbation pressure and the TKE:

$$\overline{p^*}(x,y,z_b - \frac{\Delta z}{2}) = \overline{p^*}(x,y,z_b + \frac{\Delta z}{2}) \ , \quad e(x,y,z_b - \frac{\Delta z}{2}) = e(x,y,z_b + \frac{\Delta z}{2}) \ . \tag{2.51}$$

Furthermore, a Prandtl layer is assumed between the bottom and the first prognostic vertical grid level of the scalar quantities above the surface ($z_p = z_b + \frac{\Delta z}{2}$). The vertical velocity flux is estimated with the similarity theory of Monin and Obukhov (1954) in the Prandtl layer. The components of the vertical velocity flux are calculated by:

$$\overline{w^* u_i^*} = -\frac{u_i}{|\vec{\overline{v}}|} u_*^2 \quad \text{with } i \in \{1,2\} \ . \tag{2.52}$$

The friction velocity u_* can be derived from the vertical profile of the mean horizontal wind velocity (Monin and Obukhov, 1954):

$$\frac{\partial|\vec{\overline{v}}|}{\partial z} = \frac{u_*}{\kappa z}\Phi_m \ , \tag{2.53}$$

with the von Karman constant κ, which has a value of 0.4, and the Businger-Dyer function Φ_m (Dyer, 1974). Integration of equation 2.53 leads to the equation for the friction velocity:

$$u_* = \begin{cases} \dfrac{\kappa\,|\overline{\vec{v}}(z_p)|}{\ln\left(\frac{z_p}{z_0}\right)+5Rif\left(\frac{z_p-z_0}{z_p}\right)} & \text{if } Rif \geq 0\ , \\ \\ \dfrac{\kappa\,|\overline{\vec{v}}(z_p)|}{\ln\left(\frac{z_p}{z_0}\right)-\ln\left(\frac{(1+A_m)^2}{(1+B_m)^2}\frac{(1+A_m^2)}{(1+B_m^2)}\right)+2\,(\arctan(A_m)-\arctan(B_m))} & \text{if } Rif < 0\ . \end{cases} \tag{2.54}$$

The components A_m and B_m are given by:

$$A_m = (1-16Rif)^{1/4} \quad \text{and} \quad B_m = \left(1-16Rif\frac{z_0}{z_p}\right)^{1/4}\ , \tag{2.55}$$

with the Richardson flux number (e.g. Etling, 2002):

$$Rif = \frac{z_p\,\kappa\,g\,\vartheta_*}{\theta_0\,u_*^2}\,. \tag{2.56}$$

The dimensionless Richardson flux number is the ratio of buoyancy and shear production and characterizes the dynamical stability of a flow (Stull, 1988). z_0 denotes the roughness length and represents the height where the mean wind speed is zero. It is a property of the surface (Stull, 1988) and the default value is $z_0 = 0.1\,\mathrm{m}$ in PALM. ϑ_* is the characteristic temperature and is derived by integration of the equation (Monin and Obukhov, 1954):

$$\frac{\partial\overline{\theta}}{\partial z} = \frac{\vartheta_*}{\kappa z}\Phi_h\ , \tag{2.57}$$

with the Businger-Dyer function Φ_m (Dyer, 1974), to:

$$\vartheta_* = \begin{cases} \dfrac{\kappa\left(\overline{\theta}(z_p)-\overline{\theta}(z_0)\right)}{\ln\left(\frac{z_p}{z_0}\right)+5Rif\left(\frac{z_p-z_0}{z_p}\right)} & \text{if } Rif \geq 0\ , \\ \\ \dfrac{\kappa\left(\overline{\theta}(z_p)-\overline{\theta}(z_0)\right)}{\ln\left(\frac{z_p}{z_0}\right)-2\ln\left(\frac{1+A_h}{1+B_h}\right)} & \text{if } Rif < 0\ , \end{cases} \tag{2.58}$$

with the components

$$A_h = (1-16Rif)^{1/2} \quad \text{and} \quad B_h = \left(1-16Rif\frac{z_0}{z_p}\right)^{1/2}\ . \tag{2.59}$$

The gradient of the temperature is zero in a neutrally stratified ABL. Thus, ϑ_* and Rif are zero.

For the model initialization, vertical profiles of the geostrophic flow and the potential temperature are set in the entire model domain. Depending on the flow characteristics, it can take several hours until the flow reaches a quasi-stationary state. For saving computational costs, a one-dimensional precursor run can be used. During the precursor run, the flow reaches the geostrophic balance. The calculated flow of the precursor run is used as initialization of the

three-dimensional model. With the flow of the precursor run the flow of the three-dimensional calculation reaches faster the stationary state compared to the calculation with constant initialization profiles. A detailed description of the one-dimensional model is given in section 2.8.

For damping the inertial oscillation in a neutrally stratified ABL (see section 3.1.3.1), a Rayleigh damping can be used in PALM. Therefore, an additional term is added to all prognostic equations at the final RK3 substep:

$$-R_v(\overline{u}_k - \overline{u}_{g_k}) \; . \tag{2.60}$$

The coefficient R_v is calculated by (Klemp and Lilly, 1978):

$$R_v = \begin{cases} 1 & \text{if } z \leq z_R \; , \\ \\ d_f \; \sin^2\left(\frac{\pi}{2}\frac{z-z_R}{z_t-z_R}\right) & \text{if } z \geq z_R \; . \end{cases} \tag{2.61}$$

z_R is the height where the Rayleigh damping starts. d_f is the damping factor and is set to 0.01 in this study. The damping forces the horizontal flow to the geostrophic value and reduces the vertical velocity. The damping height z_R should be equal to the boundary layer height z_i in this study.

The initialization fields do not have a horizontal gradient. Thus, turbulence cannot develop in the flow and must be generated by the model at the beginning. This is realized by imposing random perturbations to the horizontal velocity field during the first time steps. Therefore, a random generator is used which provides a specified sequence of numbers. These numbers are evenly distributed in the interval $[0, 1]$ and are multiplied to the velocity field as long as the resolved TKE reaches a threshold value.

2.8. One-dimensional model

As mentioned in section 2.7, PALM contains a one-dimensional model to provide quasi-stationary vertical profiles of the horizontal velocity components for the initialization of the three-dimensional model. During the precursor simulation, the inertial oscillation (see section 3.1.3.1) can decay. Hence, the oscillation is weaker in the three-dimensional simulation. Therefore, the three-dimensional model reaches faster the stationary state which saves computational time.

The one-dimensional model calculates prognostic equations for the horizontal velocity components u_i with $i \in \{1, 2\}$ and the TKE e:

$$\frac{\partial \overline{u}_i}{\partial t} = -\epsilon_{i3k} f_3 \overline{u}_k + \epsilon_{i3k} f_3 \overline{u}_{g_k} - \frac{\partial \overline{u_3'' u_i''}}{\partial x_3} \; , \tag{2.62}$$

$$\frac{\partial e}{\partial t} = -\frac{\partial \overline{u_3'' u_1''}}{\partial x_3} - \frac{\partial \overline{u_3'' u_2''}}{\partial x_3} - \frac{g}{\theta_0}\frac{\partial \overline{u_3'' \theta''}}{\partial x_3} - \frac{\partial \overline{u_3'' e''}}{\partial x_3} - \epsilon \; . \tag{2.63}$$

The whole turbulence spectrum is parameterized in this model because the turbulence cannot be resolved by a one-dimensional model. The dissipation ϵ is parameterized after Detering and Etling (1985):

$$\epsilon = c_0^3 \frac{e^{3/2}}{l} \tag{2.64}$$

with a value of 0.4 for the constant c_0. l is the mixing length and is calculated after Blackadar (1962):

$$l = \frac{\kappa z}{1 + \frac{\kappa z}{\lambda}} \ . \tag{2.65}$$

The typical length scale

$$\lambda = 2.7 \cdot 10^{-4} \frac{|\vec{v}_g|}{f} \tag{2.66}$$

is the maximum value for the mixing length. l is zero at the surface and increases with height until it approaches λ.
A first-order closure is taken for the Reynolds stress terms:

$$\overline{u_3'' u_i''} = -K_m \frac{\partial \overline{u}_i}{\partial x_3} \ , \quad \overline{u_3'' \theta''} = -K_h \frac{\partial \overline{\theta}}{\partial x_3} \quad \text{and} \quad \overline{u_3'' e''} = -K_m \frac{\partial e}{\partial x_3} \ . \tag{2.67}$$

K_m is calculated after the Prandtl-Kolmogorov hypothesis (Kolmogorov, 1942; Prandtl, 1945):

$$K_m = c_0 l \sqrt{e} \ , \tag{2.68}$$

and K_h is calculated by

$$K_h = \begin{cases} K_m & \text{if } Rif \geq 0 \ , \\ \\ K_m \left(1 - 16 Rif\right)^{1/4} & \text{if } Rif < 0 \ , \end{cases} \tag{2.69}$$

with the Richardson flux number

$$Rif = \begin{cases} \frac{\frac{g}{\theta_0} \frac{\partial \overline{\theta}}{\partial z}}{\left(\frac{\partial \overline{u}}{\partial z}\right)^2 + \left(\frac{\partial \overline{v}}{\partial z}\right)^2} & \text{if } Rif \geq 0 \ , \\ \\ \frac{\frac{g}{\theta_0} \frac{\partial \overline{\theta}}{\partial z}}{\left(\frac{\partial \overline{u}}{\partial z}\right)^2 + \left(\frac{\partial \overline{v}}{\partial z}\right)^2} \left(1 - 16 Rif\right)^{1/4} & \text{if } Rif < 0 \ . \end{cases} \tag{2.70}$$

The cartesian grid of the one-dimensional model extends in the vertical direction. Finite difference methods are used for the spatial discretization and the RK3 for the temporal integration (see section 2.6). At the top boundary z_t, Dirichlet boundary conditions are selected and the quantities keep their initial value:

$$u(z_t) = u_g \ , \quad v(z_t) = v_g \ , \quad e(z_t) = 0 \ . \tag{2.71}$$

At the bottom boundary z_b, Dirichlet conditions are given for the velocity and Neumann conditions for the TKE:

$$u(z_b) = 0\ , \quad v(z_b) = 0\ , \quad e(z_b) = e(z_b + 1) = \left(\frac{u_*}{0.1}\right)^2\ . \tag{2.72}$$

Prandtl conditions are assumed in the surface layer similar to the three-dimensional model (see section 2.7). The Prandtl height z_p is the first grid point above the bottom z_b. For calculation of the vertical momentum flux in the surface layer of the one-dimensional model, equations 2.52 is used. The calculation of the friction velocity differs in the one-dimensional model and is done by:

$$u_* = \begin{cases} \dfrac{\kappa\ |\overline{\vec{v}}(z_p)|}{\ln\left(\frac{z_p}{z_0}\right) + 5Rif\left(\frac{z_p - z_0}{z_p}\right)} & \text{if } Rif \geq 0\ , \\ \\ \dfrac{\kappa\ |\overline{\vec{v}}(z_p)|}{\ln\left(\frac{1+b_m}{1-b_m}\frac{1-a_m}{1+a_m}\right) + 2\ (\arctan(b_m) - \arctan(a_m))} & \text{if } Rif < 0\ , \end{cases} \tag{2.73}$$

with

$$a_m = (1 - 16Rif)^{-1/4} \quad \text{and} \quad b_m = \left(1 - 16Rif\frac{z_0}{z_p}\right)^{-1/4}\ . \tag{2.74}$$

The Richardson flux number is calculated after equation 2.56. The characteristic temperature ϑ_* is calculated by:

$$\vartheta_* = \begin{cases} \dfrac{\kappa\ \left(\overline{\theta}(z_p) - \overline{\theta}(z_b)\right)}{\ln\left(\frac{z_p}{z_0}\right) + 5Rif\left(\frac{z_p - z_0}{z_p}\right)} & \text{if } Rif \geq 0\ , \\ \\ \dfrac{\kappa\ \left(\overline{\theta}(z_p) - \overline{\theta}(z_b)\right)}{\ln\left(\frac{a_h - 1}{a_h + 1}\frac{b_h + 1}{b_h - 1}\right)} & \text{if } Rif < 0 \end{cases} \tag{2.75}$$

with

$$a_h = (1 - 16Rif)^{1/2} \quad \text{and} \quad b_h = \left(1 - 16Rif\frac{z_0}{z_p}\right)^{1/2}\ . \tag{2.76}$$

The data from the one-dimensional non-staggered grid are transferred to the three-dimensional staggered grid levels of the horizontal velocity components and scalar quantities.

2.9. Ocean model

The ocean model is based on the same basic equations and numerical schemes as the atmosphere model. However, some modifications and extensions have to be made due to the different characteristics of ocean and atmosphere. Buoyancy and static stability in the ocean are influenced by the potential temperature and the salinity. Hence, the density is calculated to

replace the potential temperature in the buoyancy and stability terms in the prognostic equations. To reach this, an additional filtered prognostic equation is computed for the salinity S of the ocean, based on equation 2.27:

$$\frac{\partial \overline{S}}{\partial t} = -\frac{\partial \overline{u_k}\,\overline{S}}{\partial x_k} - \frac{\partial \overline{u_k'' S''}}{\partial x_k} + Q_S \,. \tag{2.77}$$

The source and sink term Q_S can be switched on in terms of a surface or bottom salinity flux. The density is calculated from the equation of state for seawater with an algorithm after Jackett et al. (2006). Two different densities are calculated in PALM, the potential density ρ_{pot} and the in-situ density ρ. The in-situ density is calculated after:

$$\rho(S,\theta,p) = \frac{P_n(S,\theta,p)}{P_d(S,\theta,p)} \,, \tag{2.78}$$

where P_n and P_d are polynomials depending on salinity, potential temperature and pressure. The terms and coefficients of the polynomials are given in table A.1 and are taken from Jackett et al. (2006, table A2). The pressure increases with deeper depth and is calculated in the ocean model after the hydrostatic equation:

$$p(z) = p_{surface} + \rho_{surface}\; g\; (z_{surface} - z) \,, \tag{2.79}$$

with $p_{surface} = 1013.25\,\mathrm{hPa}$ and $\rho_{surface} = 1027.62\,\mathrm{kg\,m^{-3}}$. The sea surface is defined at $z_{surface} = 0\,\mathrm{m}$ and the depth z has negative values in the ocean, in contrast to other ocean models where the depths has typically positive values.
To obtain the potential density, the same polynomials are used but without the pressure terms. Hence, the first seven terms and the first ten terms of table A.1 are used for P_n and P_d, respectively. The potential density can be expressed as

$$\rho_{pot}(S,\theta) = \frac{P_n(S,\theta)}{P_d(S,\theta)} \,. \tag{2.80}$$

As mentioned above, the density replaces the potential temperature in some equations. The buoyancy term $+g \cdot \overline{\theta^*}/\theta_0$ in equation 2.24 for the vertical velocity is replaced by $-g \cdot \overline{\rho^*}/\rho_0$ in the ocean. The sign of the buoyancy term changes because buoyancy increases with increasing temperature but decreasing density. In the prognostic equation for the turbulent kinetic energy (Eq. 2.36) and for the mixing length (Eq. 2.35), the potential temperature is exchanged by the potential density.

The sea surface is defined at the model top ($z_t = 0$). The z-axis points from the bottom of the ocean upwards to the sea surface. Neumann conditions are chosen at the top of the model domain for the salinity and both density values (represented by the universal variable Ψ), and for the horizontal velocity components due to the absence of a large scale pressure gradient:

$$\overline{\Psi}(x,y,z_t) = \overline{\Psi}(x,y,z_t - \Delta z) \,, \tag{2.81}$$

$$\overline{u}(x,y,z_t) = \overline{u}(x,y,z_t - \Delta z) \,, \quad \overline{v}(x,y,z_t) = \overline{v}(x,y,z_t - \Delta z) \,. \tag{2.82}$$

At the bottom, Neumann conditions are also selected for all quantities represented by Ψ. Neumann conditions can be used for the horizontal velocity field as well:

$$\overline{\Psi}(x,y,z_b) = \overline{\Psi}(x,y,z_b + \frac{\Delta z}{2}) \,, \tag{2.83}$$

$$\overline{u}(x,y,z_b) = \overline{u}(x,y,z_b + \frac{\Delta z}{2}) \,, \quad \overline{v}(x,y,z_b) = \overline{v}(x,y,z_b + \frac{\Delta z}{2}) \,. \tag{2.84}$$

Boundary conditions of other quantities are equal to the atmospheric case in section 2.7.

For the initialization of the ocean, constant profiles of potential temperature, salinity and the geostrophic flow components are set in the entire model domain. Furthermore, surface fluxes at the top and the bottom can be defined for the heat, salinity and horizontal momentum. The influence of the ABL on the OML and vice versa is implemented via these fluxes as described in the following section.

2.10. Atmosphere-ocean coupling

For investigations of the atmosphere-ocean interaction, a coupling module between the atmosphere model and the ocean model is provided by PALM which exchanges the information of both layers. The coupling allows the investigation of the influence of the atmospheric flow on the oceanic current and vice versa.

The influence of the ABL on the OML is realized by recalculating the atmospheric surface fluxes of momentum, heat and moisture to the oceanic surface fluxes of momentum, heat and salinity. Positive fluxes are directed upwards and negative fluxes downwards for both, atmosphere and ocean. The momentum fluxes at the sea surface are calculated by (e.g. Glazunov and Lykossov, 2003):

$$\overline{w''u''}_o = \frac{\rho_a}{\rho_o}\overline{w''u''}_a \; , \tag{2.85}$$

$$\overline{w''v''}_o = \frac{\rho_a}{\rho_o}\overline{w''v''}_a \; . \tag{2.86}$$

Quantities with an index a refer to the atmosphere and an index o to the ocean, both close to the sea surface.
The heat flux in the ocean is influence by the atmospheric sensible heat flux and latent heat flux. A positive atmospheric sensible heat flux means that the air is heated at the sea surface and thus the ocean loose heat, which is indicated by a positive oceanic heat flux. The atmospheric latent heat flux is positive at the sea surface if water evaporates. The energy, which is needed for the evaporation, is taken from the water and the water temperature decreases. Thus, the oceanic heat flux is calculated by:

$$\overline{w''\theta''}_o = \frac{\rho_a}{\rho_o}\left(\frac{c_{p,a}}{c_{p,o}}\overline{w''\theta''}_a + \frac{l_w}{c_{p,o}}\overline{w''q''}\right) \; . \tag{2.87}$$

The latent heat flux $\overline{w''q''}$ is not marked by an index because it occurs only in the atmosphere. $c_{p,a}$ and $c_{p,o}$ denote the specific heat capacities of air and water at a constant pressure of 1013.25 hPa and are set to the values of $1005\,\mathrm{J\,kg^{-1}K^{-1}}$ and $4218\,\mathrm{J\,kg^{-1}K^{-1}}$, respectively. The specific heat of vaporization l_w is defined to the value of $2.262\,610\,8 \times 10^6\,\mathrm{J\,kg^{-1}}$.
If the atmospheric latent heat flux is positive at the sea surface, the water evaporates but the salt remains in the ocean. Thus, the salinity increases at the sea surface. If the water is mixed downwards, the salinity also increases in deeper depth which is expressed by a negative salinity

flux. Thus, the salinity flux due to evaporation is calculated, according to Steinhorn (1991), by:

$$\overline{w''S''} = -\frac{\rho_a}{\rho_o}\frac{\overline{S}}{1-\overline{S}}\overline{w''q''} \; . \tag{2.88}$$

The signs in equations 2.85 - 2.87 are converse compared to Glazunov and Lykossov (2003) because in PALM the vertical axis starts at the ocean's bottom and points upward so that a negative flux in the atmosphere remains negative in the ocean. In the model of Glazunov and Lykossov (2003) the vertical axis of the ocean starts at the sea surface and points downwards.

The lowest grid points of the atmosphere represent the sea surface which characteristic is defined by the ocean model. Thus, the resolved horizontal velocity components and the potential temperature are exchanged from the ocean model to the atmosphere model:

$$\overline{u}_a(x,y,z_b) = \overline{u}_o(x,y,z_t) \; , \tag{2.89}$$

$$\overline{v}_a(x,y,z_b) = \overline{v}_o(x,y,z_t) \; , \tag{2.90}$$

$$\overline{\theta}_a(x,y,z_b) = \overline{\theta}_o(x,y,z_t) \; . \tag{2.91}$$

The horizontal domain length of both models has to be equal, while the grid length can differ. In case of different grid lengths, a bilinear interpolation is used (M. Gryschka, personal communication 2011). For the interpolation, the condition

$$nx_o = n \; nx_a \tag{2.92}$$

must be satisfied. nx_o are the number of grid points in x-direction of the ocean model and nx_a for the atmosphere model. The same condition is necessary for the y-direction. Condition 2.92 ensures that oceanic grid points are also defined at all positions of atmospheric grid points. Thereby, the conditions $nx_o \geq nx_a$ and $ny_o \geq ny_a$ must be hold. Figure 2.3 illustrates the interpolation between both grids. On the atmospheric grid, a quantity Ψ is defined at the grid points $i \in [0, nx_a - 1]$ and $j \in [0, ny_a - 1]$. The quantity is denoted as $\Psi_a^{i,j}$ (black points in Fig. 2.3b). The oceanic grid has more grid points than the atmospheric grid. Therefore, an additional notation is necessary for the oceanic grid points which are denoted with

$$\Psi_o^{i\cdot d_{nx}+ii, j\cdot d_{ny}+jj} \quad \text{with } ii \in [0, d2_{nx}], jj \in [0, d2_{ny}] \; . \tag{2.93}$$

$d2_{nx}$ and $d2_{ny}$ are the number of oceanic grid points between two atmospheric grid points and are calculated by:

$$d2_{nx} = 2\left\lfloor \frac{d_{nx}}{2} \right\rfloor \quad \text{and} \quad d2_{ny} = 2\left\lfloor \frac{d_{ny}}{2} \right\rfloor \; , \tag{2.94}$$

with

$$d_{nx} = \frac{nx_o}{nx_a} \quad \text{and} \quad d_{ny} = \frac{ny_o}{ny_a} \; . \tag{2.95}$$

The floor function $\lfloor x \rfloor$ is an integer and defined by $\lfloor x \rfloor \leq x < \lfloor x \rfloor + 1$ (Iverson, 1962).
The exchange of information from the ocean grid to the atmosphere grid is given by

$$\Psi_a^{i,j} = \frac{1}{(d2_{nx}+1)(d2_{ny}+1)} \sum_{ii=0}^{d2_{nx}} \sum_{jj=0}^{d2_{ny}} \Psi_o^{i \cdot d_{nx}+ii, j \cdot d_{ny}+jj} \; . \tag{2.96}$$

Thereby, an averaged value over several oceanic grid points is given to an atmospheric grid point. The exchange from the atmospheric grid to the oceanic grid is calculated by

$$\begin{aligned} \Psi_o^{i \cdot d_{nx}+ii, j \cdot d_{ny}+jj} = & \left[\left(\frac{\Psi_a^{i+1,j+1} - \Psi_a^{i+1,j}}{d_{ny}} \cdot jj + \Psi_a^{i+1,j} \right) \right. \\ & \left. - \left(\frac{\Psi_a^{i,j+1} - \Psi_a^{i,j}}{d_{ny}} \cdot jj + \Psi_a^{i,j} \right) \right] \frac{1}{d_{nx}} ii + \left(\frac{\Psi_a^{i,j+1} - \Psi_a^{i,j}}{d_{ny}} \cdot jj + \Psi_a^{i,j} \right) \; . \end{aligned} \tag{2.97}$$

This has the characteristic of an bilinear interpolation.
An optimized using of the coupling module is described in section 2.11.

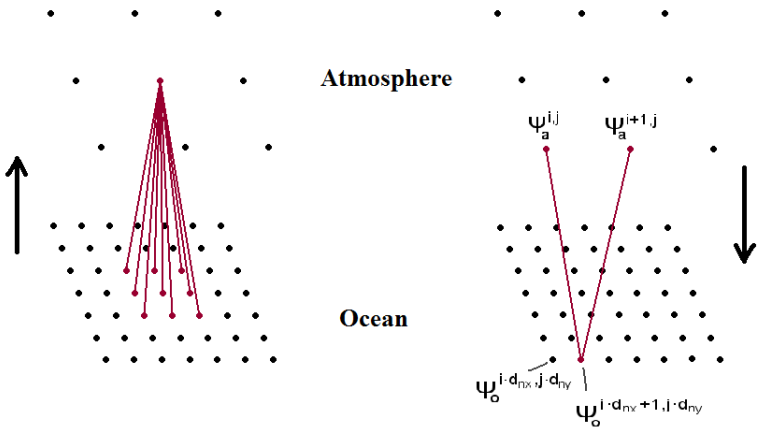

(a)

(b)

Figure 2.3.: Schematic representation of the data exchange between the atmosphere model and the ocean model at the surface during the coupling. The grid length of the ocean grid is smaller than the grid length of the atmospheric grid. (a, left) The average over the colored oceanic grid points is the received value at the colored atmospheric grid point. (a, right) The colored oceanic grid point receives a weighted average value of the colored atmospheric grid points. (b) Schematic representation of the different notation of the oceanic grid. Atmospheric quantities Ψ_a^i are marked with black circles. Oceanic quantities $\Psi_o^{i\cdot d_{nx}+ii}$ are marked with red points. d_{nx} is the ratio of the number of oceanic and atmospheric grid points in x-direction.

2.11. Parallelization

PALM is parallelized for the usage on massive parallel computers to simulate highly turbulent flows on large computational grids with high resolution (Raasch and Schröter, 2001).
For the parallelization, the model domain is decomposed into a number of subdomains which equals the number of utilized processors (PE, processor element). The decomposition can be chosen in one or two horizontal directions. The model domain is uniformly distributed on the PEs. Each PE solves the model equations for its subdomain and needs information of the neighboring PEs. These information are stored on additional grid points at the border of a subdomain (so called ghost border points) and are exchanged after every Runge-Kutta step. The data communication between the PEs is realized with the Message Passing Interface (MPI). Additional information on the parallelization can be found in the documentation of Raasch and Schröter (2001).

The coupling between atmosphere and ocean is based on the parallelization method between the single PEs. Atmosphere and ocean are separated and each PE either belongs to the atmosphere model (PE_a) or to the ocean model (PE_o). The data exchange between both models takes place after each time interval $\Delta t_{coupling}$. The coupling interval has to fulfill the condition:

$$\Delta t_{coupling} \geq max((\Delta t)_a, (\Delta t)_o) \; . \tag{2.98}$$

The data exchange is realized with MPI. Therefore, a two-dimensional field of the size of the whole model domain, $nx \times ny$, is defined on each PE. This field is only non-zero at the respective subdomains of the PEs. The fields of all PEs_a are summarized on one PE_a and the same is carried out in the ocean. The two PEs which contain the whole surface information, one the atmospheric and one the oceanic information, exchange their data. Finally, the one PE_a which contains the oceanic information sends this to each atmospheric PE and the one PE_o which contains the atmospheric information sends this to each oceanic PE.
For atmosphere and ocean model, different numbers of processors #PEs, time steps Δt and numbers of grid points N can be used, which may result in different computational times for calculations over the interval $\Delta t_{coupling}$. For saving computational costs, the load balancing should be optimized for the coupling which means that the work should be evenly distributed on all PEs as effectively as possible so that idle times of PEs are minimized. For reducing the idle time of the PEs, an optimum relationship between #PEs, the expected time step Δt and N can be constructed. A sketch for the following considerations is given in figure 2.4. Under the assumption of an equal time step for atmosphere and ocean, the ratio of #PEs should be equal to the proportion of number of respective grid points (illustrated in Fig. 2.4a):

$$\frac{\#\mathrm{PE}_a}{\#\mathrm{PE}_o} \approx \left.\frac{N_a}{N_o}\right|_{(\Delta t)_a=(\Delta t)_o} \; . \tag{2.99}$$

For different time steps and an equal number of grid points, the ratio of #PEs should be in reverse proportion to the time steps (illustrated in Fig. 2.4b):

$$\frac{\#\mathrm{PE}_a}{\#\mathrm{PE}_o} \approx \left.\frac{(\Delta t)_o}{(\Delta t)_a}\right|_{N_a=N_o} \; . \tag{2.100}$$

The combination of equation 2.99 and 2.100 leads to

$$\frac{\#\mathrm{PE}_a}{\#\mathrm{PE}_o} \approx \frac{(\Delta t)_o N_a}{(\Delta t)_a N_o} \,, \tag{2.101}$$

as an estimation for an optimized load balance of the coupling (M. Gryschka, personal communication 2011).
The advantage of the possibility to use different numbers of grid points and PEs for atmosphere and ocean shall be illustrated by an example. If different scales of turbulence shall be investigated in atmosphere and ocean, different grid lengths should be used so that the finer grid length is not needed for both models, which saves computational costs.
All simulations of the present work were computed on the SGI Altix supercomputers of the North-German Supercomputing Alliance (HLRN[2]) in Hannover and Berlin.

[2]Norddeutscher Verbund für Hoch- und Höchstleistungsrechnen.

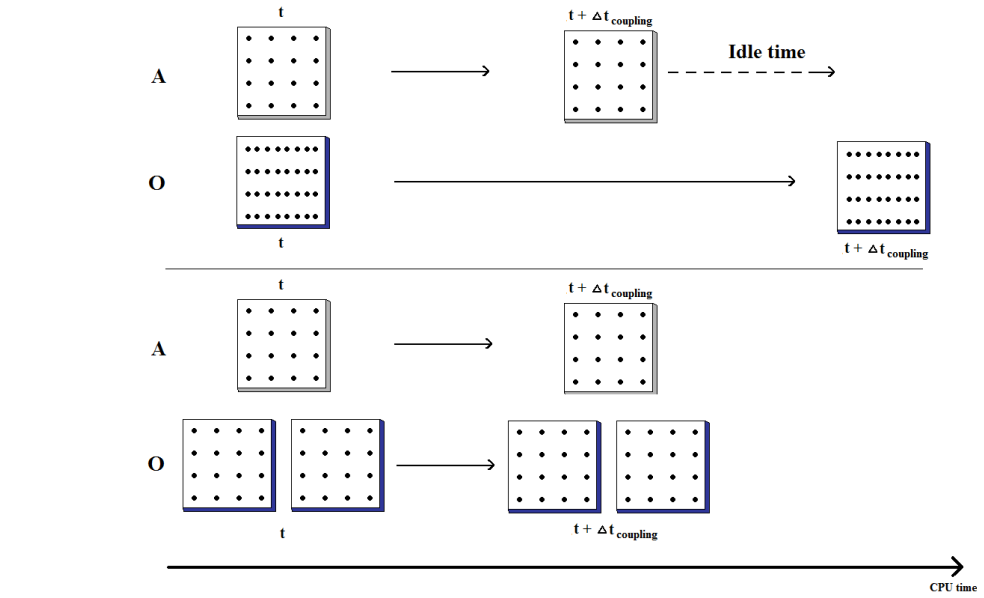

(a) $\Delta t_a = \Delta t_o$

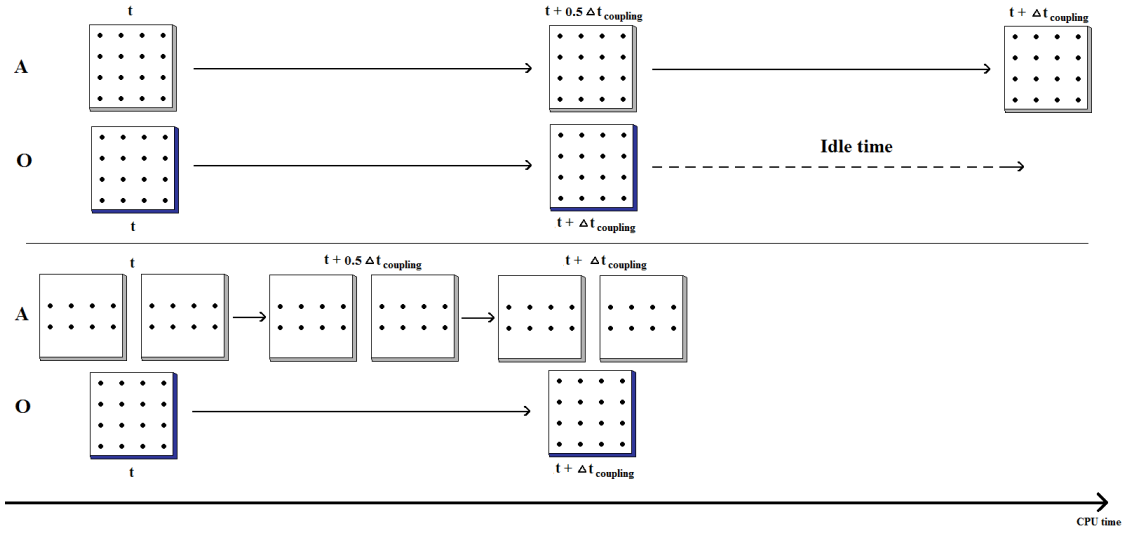

(b) $N_a = N_o$

Figure 2.4.: Schematic representation of an optimized relation between the number of processors #PE, the total number of grid points N and the time step Δt. A square represents one PE, whereby atmospheric processors PEs_a are colored grey and oceanic processors PEs_o are colored blue. The number of dots in one square denotes the number of grid points belonging to the subdomain of the PE. The axis at the bottom represents the past computation time (CPU time). (a, upper part) represents the relation of equation 2.99. The time steps of both models are equal. However, the subdomain of PE_o contains twice as many grid points as the subdomain of PE_a. Thus, PE_o needs more computation time than PE_a for calculating $\Delta t_{coupling}$, resulting in an idle time for PE_a. (Lower part) To avoid these idle times for PE_a, the number of PEs_o can be increased until a subdomain of PE_o contains the same number of grid points as a subdomain of PE_a . (b, upper part) illustrates equation 2.100, with $N_a = N_o$ and $(\Delta t)_a = 0.5(\Delta t)_o$. Hence, PE_a needs twice as much computation time for calculating $\Delta t_{coupling}$ as PE_o. (Lower part) To avoid idle times for PE_o the number of PEs_a can be doubled.

3. Simulations and Results

In a neutrally stratified ABL, the formation of roll vortices depends on wind direction and latitude (e.g. Glazunov, 2010). Using PALM, this effect is investigated and the responsible mechanisms for the roll development are examined in this study. The latitude and wind direction with the strongest roll vortices in the ABL later forms the basis for simulations of the wind driven OML flow which is neutrally stratified. The uncoupled ocean simulations are carried out with a spatially and temporally constant surface stress. General characteristics of the OML are investigated with these simulations. For investigations of the influence of the atmospheric rolls on the ocean, the coupled version of PALM is used with a sufficiently large model domain size and an adequate grid size for atmosphere and ocean to observe roll vortices. The coupled simulation needed a large amount on computational costs and thus only one coupled simulation with roll vortices could be realized during this study. To minimize computational costs, sensitivity studies were carried out for the atmosphere and ocean.

This chapter is divided into three sections. The first section deals with the results of the atmospheric simulations, starting with the description of the setup in section 3.1.1. In section 3.1.2, the effects of latitude and wind direction on the flow stability are analyzed and compared with earlier studies. Sensitivity studies were conducted to investigate the influence of model parameters, such as the model domain size and the grid length, on the observed rolls (see section 3.1.3). The energy budget terms are discussed in section 3.1.4 to identify the responsible mechanisms for the roll development. Earlier investigations showed that the dependence of the roll development on latitude and wind direction is caused by the vertical Coriolis force (e.g. Leibovich and Lele, 1985; Glazunov, 2010). To confirm these observations, simulations without the vertical Coriolis force are analyzed in section 3.1.5 and compared with previous results.
The second section contains simulation results of an OML driven by a spatially and temporally constant surface stress. Section 3.2.1 presents a model validation by comparing results with an LES study of Noh et al. (2004). Afterwards, the physical parameters, such as surface stress, are adjusted to the case which showed the strongest roll vortices in the ABL (see section 3.2.2). These simulation results show if roll vortices caused by IPI and PI also develop in the OML. Sensitivity studies are carried out in the same way as for the atmosphere (see section 3.2.3). All ocean simulations are carried out for freshwater.
Based on the atmospheric and oceanic studies, a coupled simulation is then carried out to investigate the influence of the atmospheric roll vortices on the ocean (see section 3.3).

3.1. The Parallel Instability in the atmospheric boundary layer

3.1.1. Setup

The setup of I. N. Esau (2009, personal communication) is used for the parameter study. Therefore, a neutrally stratified ABL is simulated. The model domain has a size of $L_x \times L_y \times L_z = 20\,480\,\mathrm{m} \times 20\,480\,\mathrm{m} \times 2700\,\mathrm{m}$ with a grid spacing of $\Delta x \times \Delta y \times \Delta z = 40\,\mathrm{m} \times 40\,\mathrm{m} \times 20\,\mathrm{m}$.

ϕ	$5°N$	$45°N$	$90°N$
D	$\approx 888\,\mathrm{m}$	$\approx 315\,\mathrm{m}$	$\approx 260\,\mathrm{m}$
z_i	$\approx 2800\,\mathrm{m}$	$\approx 1000\,\mathrm{m}$	$\approx 825\,\mathrm{m}$
λ_r	$\approx 16.8\,\mathrm{km}$	$\approx 6\,\mathrm{km}$	-

Table 3.1.: Estimated values for the Ekman length D, the boundary layer height z_i and the wavelength of the roll vortices λ_r (after Lilly, 1966) for different latitudes ϕ.

Above $z = 1700\,\mathrm{m}$, Δz is stretched to $40\,\mathrm{m}$ with a constant stretch factor of 1.01 (see section 2.6 for details about the stretched grid). The potential temperature θ is set to a constant value of $300\,\mathrm{K}$. The roughness length is $z_0 = 0.1\,\mathrm{m}$ and the geostrophic wind $|\vec{v}_g| = 5\,\mathrm{m\,s^{-1}}$. The latitude ϕ and the wind direction are varied in the next section (3.1.2), where the latitude has the values $\{5°N, 45°N, 90°N\}$. The simulation time is $24\,\mathrm{h}$.

Some theoretical aspects of the setup shall be considered first. The wavelength of the parallel instability is given by $\lambda_r \approx 19D$ from experimental and theoretical investigations (e.g. Lilly, 1966). The Ekman length D can be calculated by equation 1.7. Therefore, the Coriolis parameter f is calculated for different latitudes with equation 1.3 and for the diffusion coefficient K_m, a typical value of $5\,\mathrm{m^2\,s^{-1}}$ can be assumed in a neutrally stratified ABL (Etling, 2002). The height of the neutrally stratified ABL z_i is estimated by equation 1.12. All results are summarized in table 3.1. An approximation of the wavelength is not given for the pole region because earlier studies indicated no roll vortices for theses latitudes (e.g. Leibovich and Lele, 1985).
For $\phi = \{45°N, 90°N\}$, the model domain size seems to be sufficiently large and the stretched part of the grid lies above z_i. At $\phi = 5°N$, the model domain height is smaller than the estimated boundary layer height z_i. Furthermore, the wavelength estimation indicates that the model domain is sufficiently large to resolve two pairs of rolls at the mid-latitudes, but too small near the equator. Nevertheless, the setup is used for a comparison with results by I. N. Esau (2009, personal communication) but it is modified in section 3.1.3 to allow a better representation of rolls.

3.1.2. Parameter study for different latitudes and wind directions

Earlier investigations (e.g. Leibovich and Lele, 1985; Coleman et al., 1990; Glazunov, 2010) indicate that an easterly flow is more unstable than a westerly flow and that this effect increases for lower latitudes. To confirm this, the latitudes $\phi = \{5°N, 45°N, 90°N\}$, according to I. N. Esau (2009, personal communication), are analyzed.
The used coordinate system (see Fig. 3.1) is equivalent to that in Leibovich and Lele (1985). A westerly geostrophic wind ($u_g = 5\,\mathrm{m\,s^{-1}}$ and $v_g = 0\,\mathrm{m\,s^{-1}}$) is defined as an angle of $\alpha = 0°$ and an easterly geostrophic wind ($u_g = -5\,\mathrm{m\,s^{-1}}$ and $v_g = 0\,\mathrm{m\,s^{-1}}$) is defined as an angle of $\alpha = 180°$ with $\alpha \in [-180°, 180°]$. The investigated wind directions are given in table 3.2. The absolute value of the geostrophic wind $|\vec{v}_g| = 5\,\mathrm{m\,s^{-1}}$ remains constant for all wind directions.

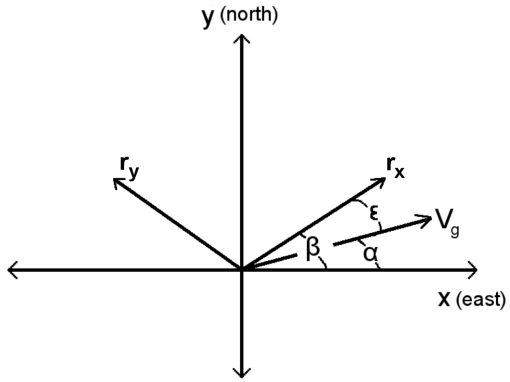

Figure 3.1.: The used coordinate system is equivalent to that in Leibovich and Lele (1985). The x-axis points east and the y-axis north. The r_x-axis is oriented parallel to the roll axis. V_g denotes the atmospheric geostrophic wind or the oceanic surface current. The angle α represents the direction of V_g in relation to the north-east-system. β is the angle between the roll axis and the x-axis and ϵ the band orientation angle between the roll axis and V_g.

For simplification in the following analysis, the cases with a westerly ($\alpha = 0°$) and an easterly ($\alpha = 180°$) geostrophic wind are denoted with W5, W45, W90 and E5, E45, E90, respectively, where the number refers to the latitude.

α	$0°$	$60°$	$120°$	$180°$	$-120°$	$-60°$
u_g	$5\,\mathrm{m\,s^{-1}}$	$2.5\,\mathrm{m\,s^{-1}}$	$-2.5\,\mathrm{m\,s^{-1}}$	$-5\,\mathrm{m\,s^{-1}}$	$-2.5\,\mathrm{m\,s^{-1}}$	$2.5\,\mathrm{ms^{-1}}$
v_g	$0\,\mathrm{m\,s^{-1}}$	$4.33\,\mathrm{m\,s^{-1}}$	$4.33\,\mathrm{m\,s^{-1}}$	$0\,\mathrm{m\,s^{-1}}$	$-4.33\,\mathrm{m\,s^{-1}}$	$-4.33\,\mathrm{m\,s^{-1}}$

Table 3.2.: Simulated geostrophic wind directions and related wind components.

I. N. Esau (2009, personal communication) compared instantaneous horizontal cross-sections of the vertical velocity w at $z = 640\,\mathrm{m}$ for a westerly and an easterly geostrophic wind at $\phi = 5°N$ from LES data of a neutrally stratified ABL (Fig. 3.2a and 3.2b). The figures show that large coherent updraft (blue) and downdraft (yellow/red) zones develop for an easterly but not for a westerly geostrophic wind. Figures 3.2c and 3.2d show the same horizontal cross-sections of the present study. Large coherent updraft (red) and downdraft (blue) zones can also be observed for E5 but not for W5. Similar results are also given by Glazunov (2010) at $\phi = 15°N$ using LES. The coherent updraft and downdraft zones are indicators for roll vortices and the roll axis is oriented along these coherent zones. The roll circulations can be visualized by streamlines based on the deviation from the mean velocity:

$$u_i^* = u_i - \overline{u}_i \; . \tag{3.1}$$

$\overline{u}_i$ is the average of u_i along the x_i-axis. Figure 3.3 presents instantaneous vertical cross-sections of the vertical velocity w and streamlines of (v^*, w^*), both are averaged along the

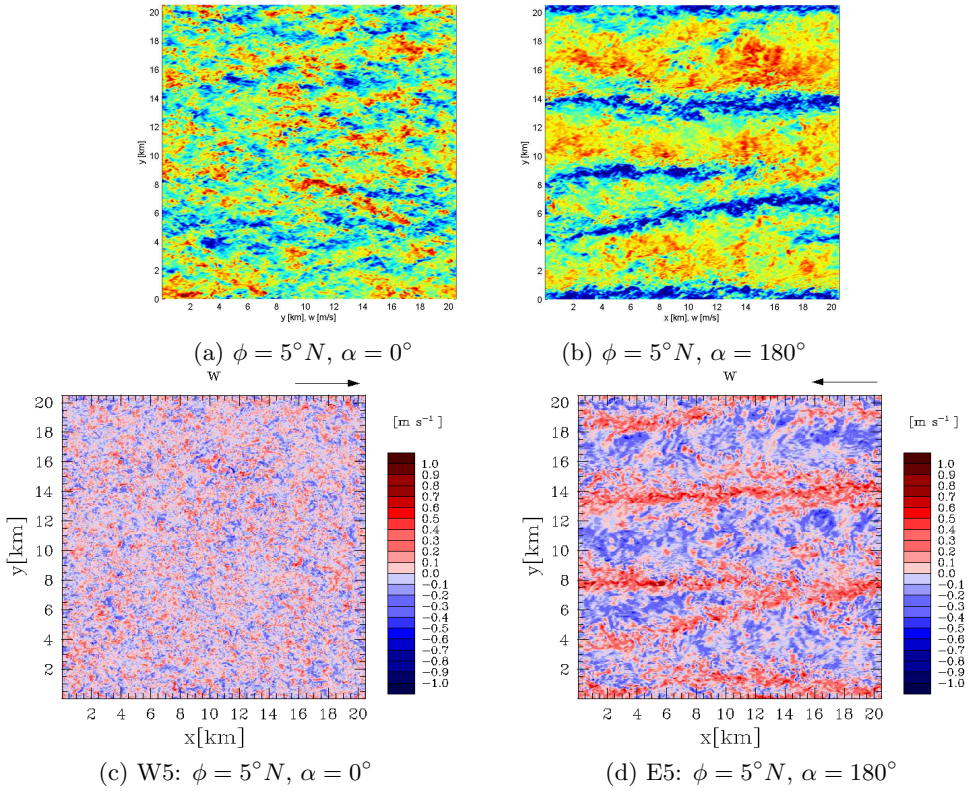

(a) $\phi = 5°N$, $\alpha = 0°$ (b) $\phi = 5°N$, $\alpha = 180°$

(c) W5: $\phi = 5°N$, $\alpha = 0°$ (d) E5: $\phi = 5°N$, $\alpha = 180°$

Figure 3.2.: Instantaneous horizontal cross-sections of the vertical velocity w at $z = 640\,\mathrm{m}$ after 24 h of simulation time. (a, b): Results are from I. N. Esau (2009, personal communication): (a) Westerly and (b) easterly geostrophic wind. (c, d): Results from this study: (c) Westerly and (d) easterly geostrophic wind (marked by the black arrow).

x-axis. The roll structure is visible for E5 (Fig. 3.3b) and shows that the large coherent updraft and downdraft zones are connected to surface convergences and divergences, respectively. The roll wavelength is defined as the width of one roll pair. Hence, the averaged wavelength of all developed rolls can be determined by the model domain length L_y divided by the number of roll pairs or can be estimated by the number of coherent updraft or downdraft zones divided by L_y. For E5 (Fig. 3.3b), the averaged roll wavelength $\overline{\lambda}_r$ is approximately 6800 m. However, the rolls reach the top of the model domain which can affect their wavelength due to their symmetry. For further investigations of this influence see section 3.1.3.1. In case of W5 (Fig. 3.3a), large coherent structures cannot be observed within the flow and the unorganized turbulent structures do not reach the top of the model domain. Overall, figures 3.2 and 3.3 show that the results of this study are in good agreement with earlier investigations.

The roll wavelength λ_r can be also determined from the variance (or energy) spectrum of the vertical velocity component or horizontal velocity component which is perpendicular to the roll axis. To calculate the two-dimensional variance spectrum of w and v, the horizontal cross-section is needed. The spectrum of a horizontal cross-section is based on a two-dimensional FFT. The result of the two-dimensional FFT is a two-dimensional matrix with the real F_{real} and the imaginary F_{imag} part of the Fourier transform which are elements of the frequency

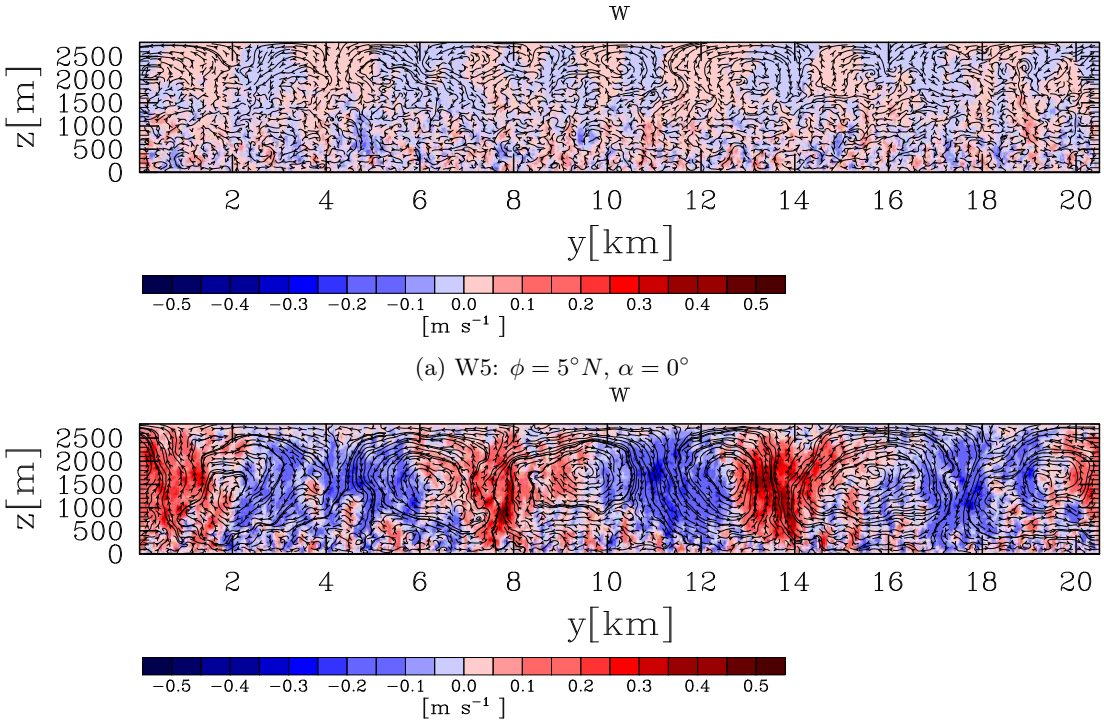

(a) W5: $\phi = 5°N$, $\alpha = 0°$

(b) E5: $\phi = 5°N$, $\alpha = 180°$

Figure 3.3.: Instantaneous vertical cross-sections of the vertical velocity w, averaged along the x-axis, and streamlines of (v^*, w^*) after 24 h of simulation time for (a) a westerly and (b) an easterly geostrophic wind.

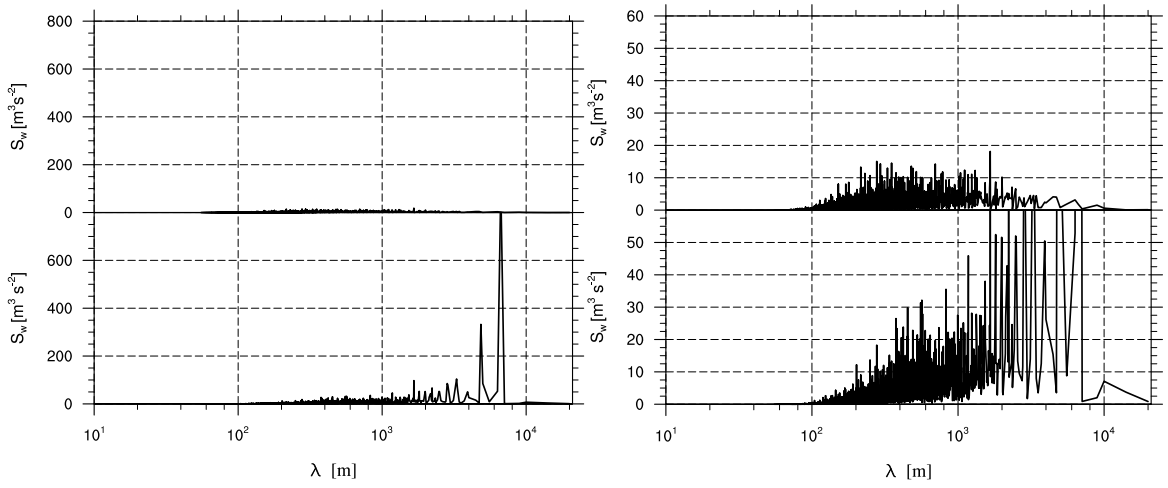

Figure 3.4.: Spectral energy density S_w of the vertical velocity w as a function of the wavelength λ calculated at $z = 1280$ m. The upper spectra are calculated from W5 and the lower spectra from E5. The right spectra is a cut-out of the left spectra for better resolving the energy levels of the smaller wavelengths.

space. For an $N \times N$ cross-section of a quantity Ψ, each of $F_{\Psi,real}$ and $F_{\Psi,imag}$ span an $N \times N$ domain in the frequency space. The frequency domains are divided into four quadrants by the row $N/2$ and column $N/2$ if the field indices are running from zero to $N-1$. The diagonally opposed quadrants are mirror images of each other and the mirrored values of the imaginary part are opposite in sign. This symmetry can be expressed by (Smith, 1997):

$$F_{\Psi,real}(r,c) = F_{\Psi,real}(N-r, N-c) \;, \tag{3.2}$$

$$F_{\Psi,imag}(r,c) = -F_{\Psi,imag}(N-r, N-c) \;, \tag{3.3}$$

considering that the frequency spectrum is periodic and repeating itself every Nth grid point. Thus, $F_\Psi(r,N)$ should be interpreted as $F_\Psi(r,0)$, $F_\Psi(N,c)$ as $F_\Psi(0,c)$ and $F_\Psi(N,N)$ as $F_\Psi(0,0)$. Small wavenumbers are at the outside corner of each quadrant and larger wavenumbers near the center. Thus, the largest wavenumber is at $(N/2, N/2)$ (Smith, 1997). The square of the norm of the complex Fourier transform is (Stull, 1988):

$$|F_\Psi|^2 = F^2_{\Psi,real} + F^2_{\Psi,imag} \;. \tag{3.4}$$

$|F_\Psi|^2$ spans an $N \times N$ domain with the same symmetry properties as the domain of $F_{\Psi,real}$. The wavenumber k is defined as $k = \sqrt{k_x^2 + k_y^2}$. k_x and k_y are the wavenumbers referring to the four outside corners of each quadrant (illustrated in Fig. 24-10 of Smith, 1997). The summation of $|F_\Psi|^2(k)$ over equal wavenumbers k results in the discrete spectral energy $E_\Psi(k)$ (Stull, 1988). The spectral energy density S_Ψ is calculated by (Stull, 1988):

$$S_\Psi(k) = \frac{E_\Psi(k)}{\Delta k} \;, \tag{3.5}$$

where Δk is the difference between neighboring wavenumbers.

The spectral energy density S_w of the vertical velocity is calculated at $z = 1280\,\mathrm{m}$ because the vertical velocity has its highest values in the range of $H/2$ and the vertical extension of the roll vortices H is equal to the model domain height for E5 (see figure 3.3b). For the case W5 and E5, figure 3.4 shows the spectral energy density S_w of the vertical velocity as a function of wavelength λ which is the reciprocal of the wavenumber k. For W5, S_w has no significant peaks at larger wavelengths. For E5, S_w has large peaks at $\lambda = 6660\,\mathrm{m}$ and $\lambda = 4850\,\mathrm{m}$ (values are taken from the data). The value of the largest peak is in good agreement with the value of the visual analysis $\overline{\lambda}_r = 6800\,\mathrm{m}$ given above.

To show that the stability difference between easterly and westerly winds is also valid for other wind directions, horizontal cross-sections of the vertical velocity w for the angles $\alpha = [60°, 120°, -120°, -60°]$ are presented in figure 3.5. The graphic shows that the turbulence is well organized in rolls for wind directions with an easterly component (right) and unorganized for winds with a westerly component (left). The black arrows mark the direction of the geostrophic wind and show that the occurred rolls are aligned to $\vec{v}_g$ ($\epsilon = 0$). The variance spectra of w in figure 3.6 of the four simulations show the same effect as for W5 and E5. The spectra of the simulations with a westerly wind component have no significant peak at larger wavelengths. The spectra with an easterly wind component have the largest peak at a wavelength of 5550 m for $\alpha = -120°$ and 6330 m for $\alpha = 120°$. Hence, the wavelength is in the same range as for E5.

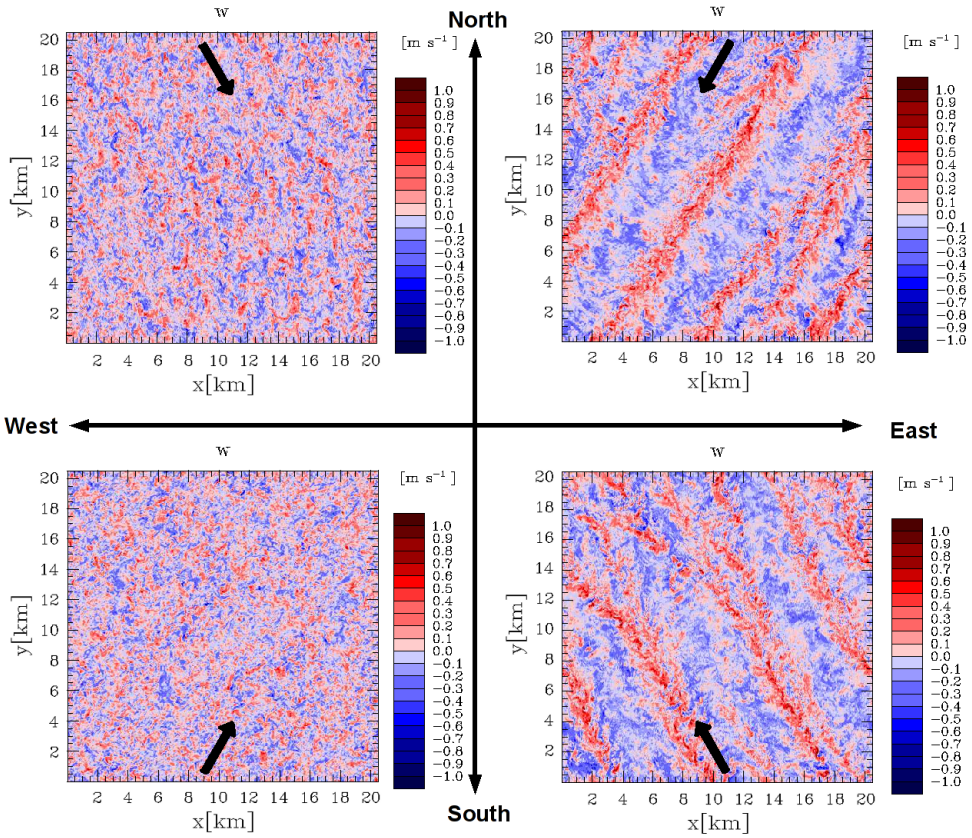

Figure 3.5.: Instantaneous horizontal cross-sections of the vertical velocity w at $z = 640\,\mathrm{m}$ at $\phi = 5°N$ after 24 h of simulation time for different geostrophic wind directions (marked by the black arrow): (Top left) north-northwest wind: $\alpha = -60°$, (top right) north-northeast wind: $\alpha = -120°$, (bottom left) south-southwest wind: $\alpha = 60°$ and (bottom right) south-southeast wind: $\alpha = 120°$.

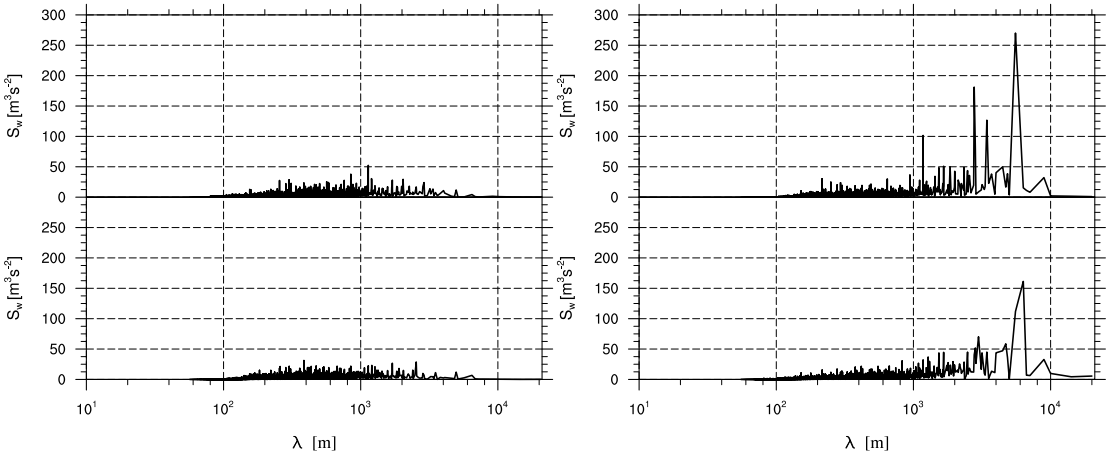

Figure 3.6.: Spectral energy density S_w of the vertical velocity w as a function of the wavelength λ calculated at $z = 1280\,\mathrm{m}$. The spectra are arranged as in figure 3.5.

Earlier investigations (e.g. Leibovich and Lele, 1985; Glazunov, 2010) explained that the difference between an easterly and a westerly wind depends on the vertical Coriolis component which has its maximum at the equator and decreases towards the poles. If the roll development depends on the vertical Coriolis force, it must also decrease towards the poles. Therefore, horizontal cross-sections of the vertical velocity w for the cases W45, E45 and W90, E90 are presented in figure 3.7. The difference of the turbulence organization between an easterly and westerly geostrophic wind is still visible at $45°N$ latitude. However, the organization of updrafts and downdrafts is weaker compared to those for E5 in figure 3.2d and the averaged wavelength is roughly estimated to $4.5\,\mathrm{km} - 5.7\,\mathrm{km}$. The black line in figure 3.7b is adjusted to the roll axis for an estimation of the band orientation angle ϵ. The geostrophic wind flows parallel to the x-axis and the angle between this axis and the black line is 26.5°. Thus, the rolls are deflected to the right of the geostrophic wind with $\epsilon \approx 26.5°$. The mean wind is turned to the left on the northern hemisphere due to the Coriolis force. Thus, it is not clarified why the rolls turned to the right of the geostrophic wind. For W90 and E90, the whole turbulence is unorganized (Fig. 3.7c and Fig. 3.7d). This was expected, as mentioned above, because the vertical Coriolis force is zero at $\phi = 90°N$.
The comparison between the variance spectra S_w of W45 and E45 shows the same results as S_w of W5 and E5 but less strongly (Fig. 3.8a). Larger wavelengths are stronger than smaller wavelengths for E45 but a significant peak does not exist. The difference between the spectra S_w of W90 and E90 is not significant and in both cases, the contribution of wavelengths of the order of 100 m is larger than those of order of 1000 m.

In figure 3.9 the vertical profiles of the mean horizontal wind components are presented for a westerly and an easterly geostrophic wind at different latitudes. The profiles of W45, E45, W90 and E90 show the same characteristics as the ideal Ekman flow (see Fig. 1.1). Starting from the surface, the u-component strongly increases with height and becomes super-geostrophic due to the horizontal Coriolis force at $z \approx 300\,\mathrm{m}$ for W90 and E90, and $z \approx 500\,\mathrm{m}$ for W45 and E45. The v-component also increases with height near the surface, reaches a maximum value at $z \approx 100\,\mathrm{m}$ and decreases to zero above. The typical Ekman profile does not develop near the equator because the horizontal component of the Coriolis force is close to zero. A significant difference in the vertical profiles of the horizontal velocity components occurs between W5 and E5. A smaller vertical gradient of the horizontal velocity components for E5 indicates stronger vertical mixing compared to W5. For W5, the mean horizontal wind becomes geostrophic at $z \approx 1600\,\mathrm{m}$. For E5, the mean horizontal wind does not become geostrophic because the model domain height of 2700 m is not large enough. The stronger vertical mixing can be seen in the vertical profiles of the vertical momentum flux[1] which is calculated by (e.g. Etling, 2002):

$$\overline{w\vec{v}_h} = \sqrt{\overline{wu}^2 + \overline{wv}^2}\ . \tag{3.6}$$

Figure 3.10 presents these profiles for different latitudes. The vertical mixing for E5 is stronger than for W5 and the mixing for E45 is stronger than for W45. The vertical mixing does not significantly differ for E90 and W90. Hence, the difference of vertical mixing between an easterly and a westerly geostrophic wind decreases with increasing latitude. The stronger vertical mixing occurs in the same cases where roll vortices developed because rolls develop in case of E5 and E45 (stronger vertical mixing) while rolls do not develop in case of W5 and W45

[1]For a physical momentum flux, the term has to be multiplied by density. In the following velocity fluxes are also called momentum fluxes.

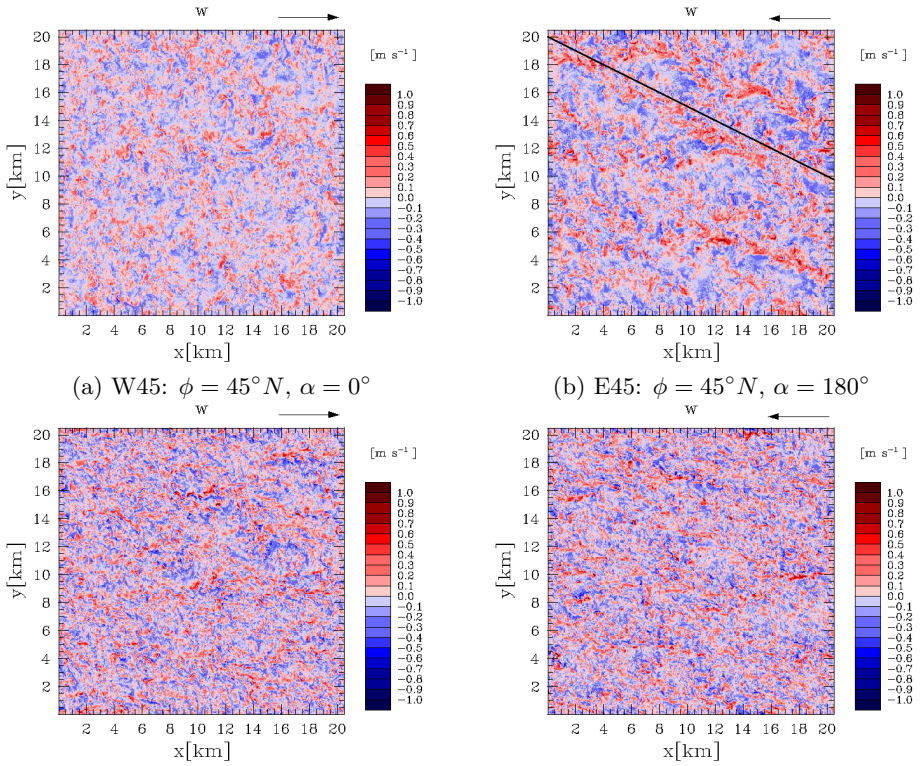

(a) W45: $\phi = 45°N$, $\alpha = 0°$

(b) E45: $\phi = 45°N$, $\alpha = 180°$

(c) W90: $\phi = 90°N$, $\alpha = 0°$

(d) E90: $\phi = 90°N$, $\alpha = 180°$

Figure 3.7.: Instantaneous horizontal cross-sections of the vertical velocity w after 24 h of simulation time. (a,b): At $z = 640$ m for (a) a westerly and (b) an easterly geostrophic wind. (c,d): At $z = 320$ m for (c) a westerly and (d) an easterly geostrophic wind. The black line in (b) is used for an estimation of ϵ (see text for more details).

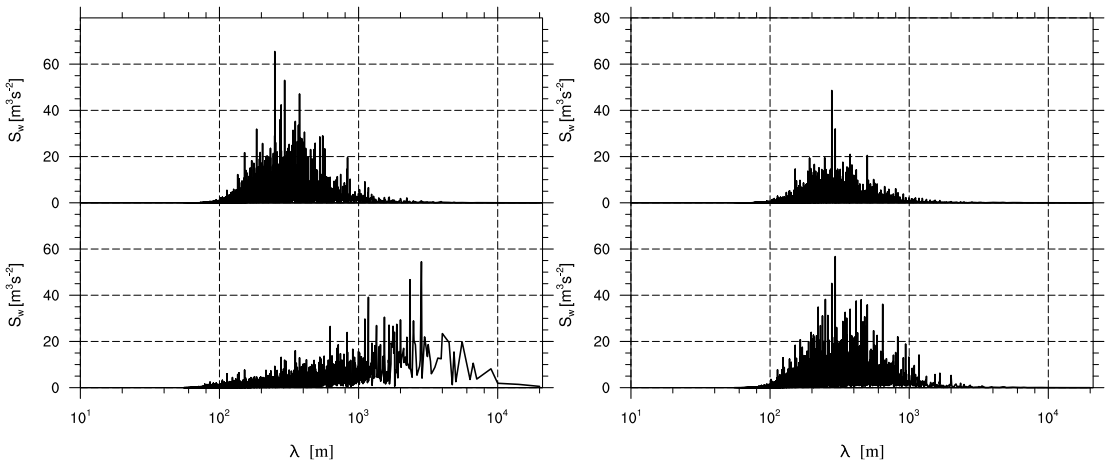

(a) $\phi = 45°N$

(b) $\phi = 90°N$

Figure 3.8.: Spectral energy density S_w of the vertical velocity w as a function of the wavelength λ calculated at (a) $z = 1280$ m (b) $z = 320$ m. The upper spectra are for a westerly geostrophic wind and the lower spectra for an easterly geostrophic wind.

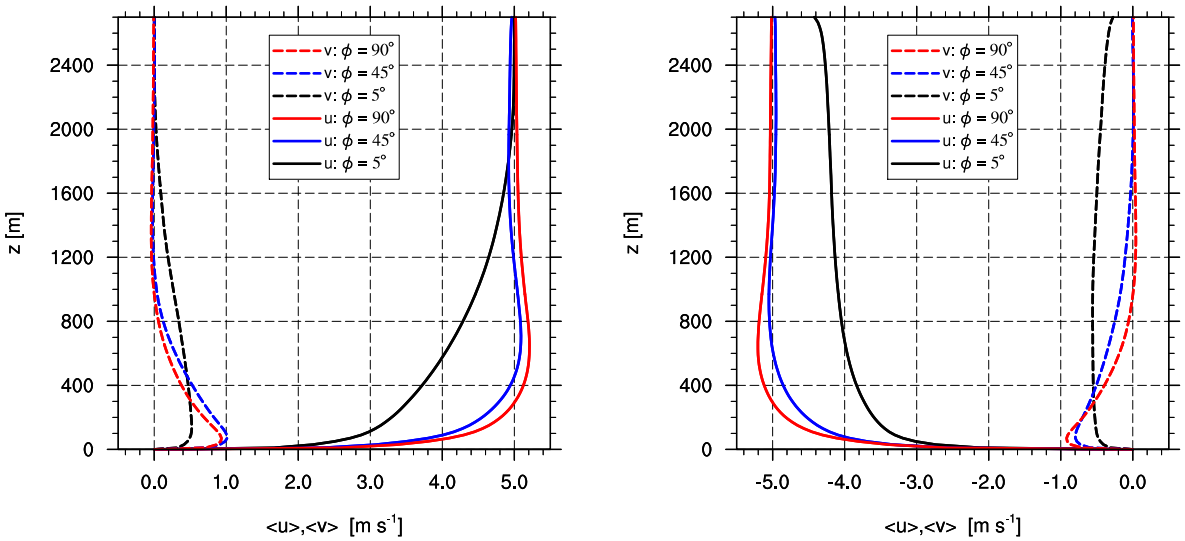

(a) W: $\alpha = 0°$ (b) E: $\alpha = 180°$

Figure 3.9.: Vertical profiles of the mean horizontal wind components $\overline{u}$ and $\overline{v}$ (or $< u >$ and $< v >$) at different latitudes for (a) a westerly and (b) an easterly geostrophic wind.

(weaker vertical mixing). In the cases W90 and E90, rolls do not occur within the ABL and a difference between the wind directions cannot be observed in the vertical mixing. However, it is not clarified if rolls increase the vertical mixing and further detailed studies are necessary.

In a neutrally stratified ABL, the boundary layer height z_i can be defined as the height where the vertical momentum flux decreases to 10 % of its surface value (e.g. Kraus, 2008). The values for z_i are calculated from the vertical profiles in figure 3.10 and are presented in table 3.3. A significant difference in z_i can be seen comparing W5 and E5 as well as W45 and E45. The difference of z_i between W90 and E90 is small. These results indicate that the development of roll vortices increase z_i.

For a comparison between theory and simulation results of this study, the estimated values of z_i and λ_r of section 3.1.1 are listed in table 3.3 as well. Comparing z_i, it is evident, that the value of W5 is significantly smaller than the estimated value. This is also the case for W45. However, the value of E45 is larger than the estimated value. The values of E90 and W90 are close to the estimated z_i for this latitude. The differences between theoretical estimations and calculation from simulation data can be explained by the Ekman flow. For the theoretical estimation, a quasi-laminar Ekman flow is assumed with a constant turbulent diffusion coefficient. The simulations produce a turbulent Ekman flow where K_m is not constant with high. An other aspect is that the turbulence production differs for the wind direction and the latitude which is also not considered in the theoretical estimation. The difference of the vertical transport between westerly and easterly geostrophic flows is also not considered in models where the whole turbulence spectrum is parameterized. For example, the one-dimensional model of PALM exclude this effect because the turbulent diffusion coefficient of the parameterization does not depend on the wind direction. The parameterization of this effect in one-dimensional ABL models is discussed by (Glazunov, 2010).

The wavelength of the observed rolls shall be compared with those from the estimation

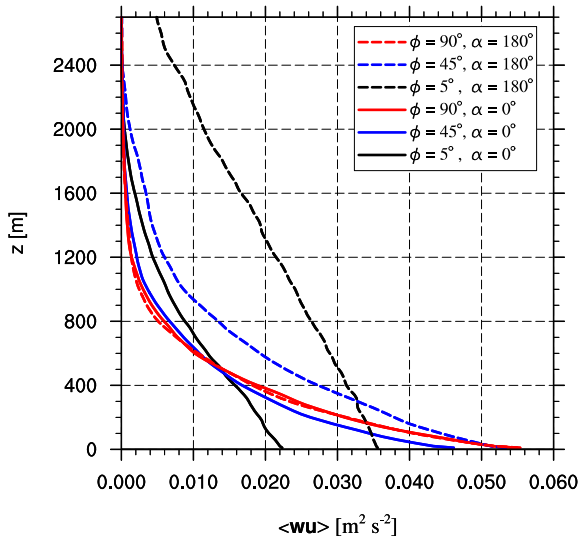

Figure 3.10.: Vertical profiles of the total vertical momentum flux at different latitudes for westerly and easterly winds.

ϕ	$5°N$	$45°N$	$90°N$
Westerly flow	$z_i \approx 1540\,\mathrm{m}$	$z_i \approx 940\,\mathrm{m}$	$z_i \approx 840\,\mathrm{m}$
Easterly flow	$z_i > 2700\,\mathrm{m}$, $\overline{\lambda}_r \approx 6.6\,\mathrm{km}$	$z_i \approx 1280\,\mathrm{m}$, $\overline{\lambda}_r \approx 4.5\,\mathrm{km} - 5.7\,\mathrm{km}$	$z_i \approx 800\,\mathrm{m}$
Estimation	$z_i \approx 2800\,\mathrm{m}$, $\lambda_r \approx 16.8\,\mathrm{km}$	$z_i \approx 1000\,\mathrm{m}$, $\lambda_r \approx 6\,\mathrm{km}$	$z_i \approx 825\,\mathrm{m}$

Table 3.3.: Boundary layer height z_i and averaged wavelength of roll vortices $\overline{\lambda}_r$ from the simulation data and the theoretical values of the estimation in section 3.1.1.

$\lambda \approx 19D$ by Lilly (1966). The averaged wavelength of the simulated rolls $\overline{\lambda}_r$ is similar for E5 and E45 and is close to the estimated value for $\phi = 45°N$. The estimated value at $\phi = 5°N$ is larger than the observed roll vortices. However, the horizontal domain was not large enough to observe rolls with a wavelength of 16.6 km. The possible influence of the domain size is further investigated in section 3.1.3.2.

Earlier investigations show that the larger instability of an easterly geostrophic wind compared to a westerly affects the surface stress which has also an effect on the OML. Figure 3.11 provides the surface stress for different wind directions of various studies. Coleman et al. (1990) calculated the surface stress at $\phi = 45°N$ and showed that the value of u_* for a westerly geostrophic wind is reduced by 6 % of the value for an easterly geostrophic wind (see Fig. 3.11a). Glazunov (2010) calculated a difference of 7 %−8 % at $45°N$ latitude. I. N. Esau (2009, personal communication) extended these results for further latitudes and wind directions (see Fig. 3.11b) and illustrated that the difference between an easterly and a westerly geostrophic wind increases with decreasing latitude. Figure 3.11c shows the results of this study. The difference between E45 and W45 is 7 % at $\phi = 45°N$ which suits with the values above. At $\phi = 5°N$ the difference between E5 and W5 is 21 %.

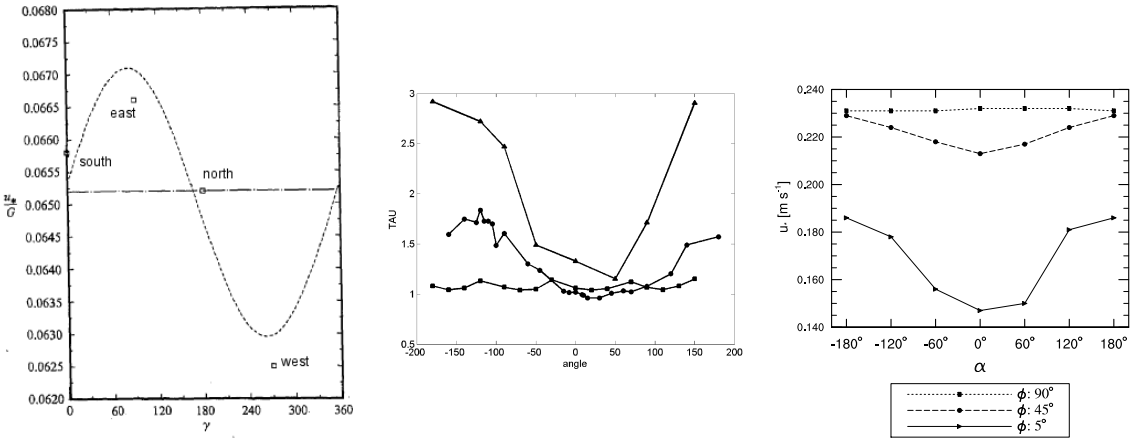

(a) Coleman et al. (1990) (b) I. N. Esau (2009, personal communication) (c) Present study

Figure 3.11.: Dependence of the surface stress in the ABL on wind direction α (or γ) and latitude ϕ. (a) The spatially averaged friction velocity normalized by the geostrophic wind at $\phi = 45°N$ for four wind directions, together with an interpolation function (Coleman et al., 1990). (b) Normalized surface stress τ at $\phi = 5°N$ (triangles), $\phi = 45°N$ (circles) and $\phi = 90°N$ (squares) (I. N. Esau 2009, personal communication). (c) The spatially averaged friction velocity u_* of the present study.

The difference of the surface stress between an easterly and a westerly geostrophic wind is caused by a higher turbulence production, organized as well as unorganized, due to the vertical Coriolis force (Glazunov, 2010). That the unorganized turbulence is also responsible for the difference between a westerly and an easterly flow can be seen in the studies of Coleman et al. (1990) and Zikanov et al. (2003). Both studies show an difference between the flow regimes without roll structures in their solutions. Zikanov et al. (2003) argued that the vertical component of the Coriolis force influence the turbulence production in two ways. First, the Coriolis term is a source/sink term in the dynamic equation for $\overline{u'w'}$ and $\overline{v'w'}$ and hence influence the shear production terms in equation 1.16. Second, the Coriolis terms redistributes the TKE between the horizontal and vertical components of the TKE. A detailed explanation can be found in Zikanov et al. (2003).
The influence of the rolls on the surface stress can be seen in figure 3.12. For W5, areas with larger values (red) and smaller values (blue) of u_* are unorganized (Fig. 3.12a) and for E5, these areas are organized in large bands due to the roll vortices (Fig. 3.12b). A comparison of the variance spectrum of the friction velocity S_{u_*} show that the influence of the roll vortices is presented at the surface. Large peaks in S_{u_*} are presented between wavelengths of 6000 m and 10 000 m. These peaks are caused by the roll vortices and are not presented in case of W5. At the sea surface, the bands of stronger and weaker surface stress form convergence and divergence zones and the effect on a wind driven ocean current is investigated in section 3.3 in the coupled atmosphere-ocean simulation.

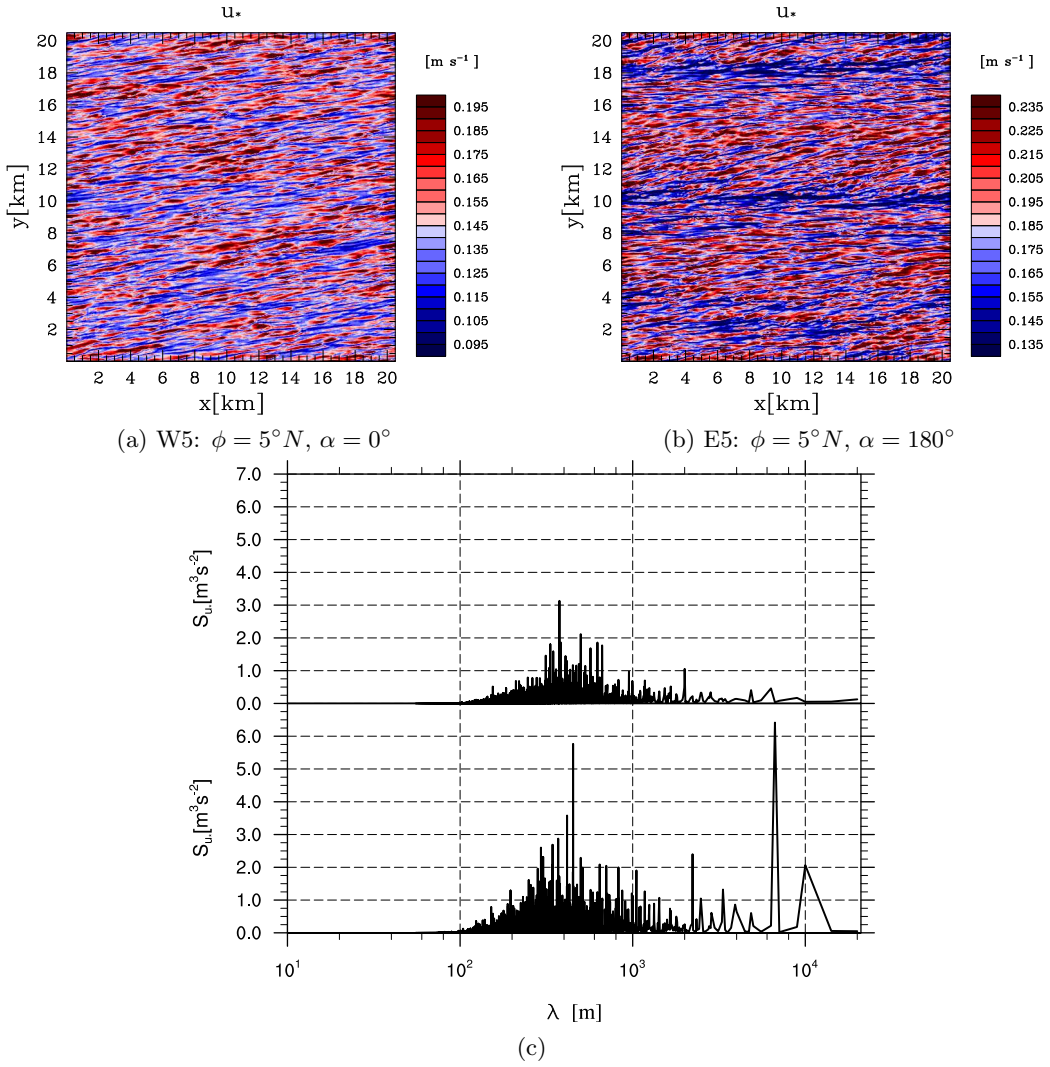

(a) W5: $\phi = 5°N$, $\alpha = 0°$ (b) E5: $\phi = 5°N$, $\alpha = 180°$

(c)

Figure 3.12.: (a, b) Instantaneous horizontal cross-sections of the friction velocity $u_{*,a}$ at the surface after 24 h of simulation time. It should be noted that the scales are different for W5 and E5. (c) Spectral energy density S_{u_*} of the friction velocity u_* as a function of the wavelength λ calculated from the cross-sections shown above. The upper spectrum is based on the data of W5 and the lower spectrum of E5.

3.1.3. Sensitivity study

The roll characteristics can be influenced by the model domain size or the grid resolution. An enlargement of the domain size or a higher grid resolution needs more computational time. Therefore, the influence of these parameters shall be investigated in the following and an optimized setup will be created for further investigations. The sensitivity studies are conducted with the case E5 of section 3.1.2 because this case shows the strongest roll development.

3.1.3.1. Height of the atmospheric boundary layer

For E5 of the previous section, the developed roll vortices reach the top of the model domain $L_z = 2700\,\mathrm{m}$ (see Fig. 3.3b). Hence, the model domain could affect the roll wavelength λ_r, the vertical extension of the roll vortices and their band orientation angle. To investigate this impact, two simulations are carried out with a model domain height of $L_z = 5220\,\mathrm{m}$ and $L_z = 7140\,\mathrm{m}$. The vertical grid length Δz is 20 m and above $z = 1700\,\mathrm{m}$, Δz is stretched to a maximum value of 40 m for saving computational time.

Figure 3.13 shows that the roll vortices reach the top of the model domain for $L_z = 5220\,\mathrm{m}$ and $L_z = 7140\,\mathrm{m}$, i.e. the roll vortices have different heights H. Some roll vortices ranges over the whole vertical model domain and other are smaller. One interesting observation is that roll vortices can develop above each other. For example, this can be observed between $x = 0\,\mathrm{km}$ and $x = 4\,\mathrm{km}$ in figure 3.13b. Figure 3.14 shows the spectral energy density of the vertical velocity S_w for $L_z = 5220\,\mathrm{m}$ and $L_z = 7140\,\mathrm{m}$. A comparison with S_w from the simulation E5 with $L_z = 2700\,\mathrm{m}$ (Fig. 3.4) reveals that the largest spectral peak is at a wavelength of 6660 m for all three model domain heights. However, for $L_z = 5220\,\mathrm{m}$ and $L_z = 7140\,\mathrm{m}$, a large peak is presented at a wavelength of 10 000 m which is also found in S_{u_*} at the surface for $L_z = 2700\,\mathrm{m}$ (see Fig. 3.12c).

An influence of the model domain height can be avoided with a temperature inversion as a physical boundary. The inversion height is defined at $z_{inv} = 3000\,\mathrm{m}$. Starting from this height, the potential temperature increases with $3\,\mathrm{K}/100\,\mathrm{m}$. The height z_{inv} is sufficiently large so that the wavelength of the roll vortices is not affected, as shown by the results above. At $\phi = 45°N$ and $\phi = 90°N$, z_{inv} is larger than z_i (see Tab. 3.3) and does not affect the flow of the ABL.
To examine the influence of the inversion, all simulations of the previous sections are repeated. In these simulations, Δz is 40 m in the entire boundary layer and is stretched within the inversion layer, so that the whole model domain L_z is 3960 m.
The so-called inertial oscillation is induced by the increasing of turbulence at the beginning of the simulation. In larger heights, the flow is braked by the friction due to the stronger turbulence and the flow becomes subgeostrophic. The Coriolis force acts then as a restoring force and the flow oscillates around the geostrophic value. The period of the inertial oscillation is:

$$\tau_i = \frac{2\pi}{f} \,. \tag{3.7}$$

At $\phi = 5°N$, the period of the inertial oscillation τ_i is approximately 138 h. This oscillation has no influence on the roll development and structure (Dubos et al., 2008). However, it delays the reaching of a stationary state. To reduce this delay, a one-dimensional precursor run (see

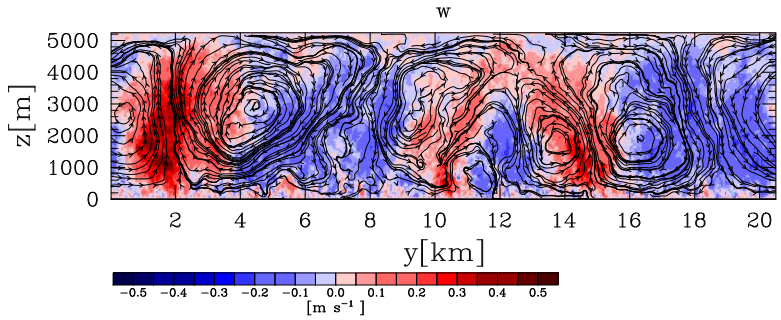

(a) E5: $\phi = 5°N$, $\alpha = 180°$

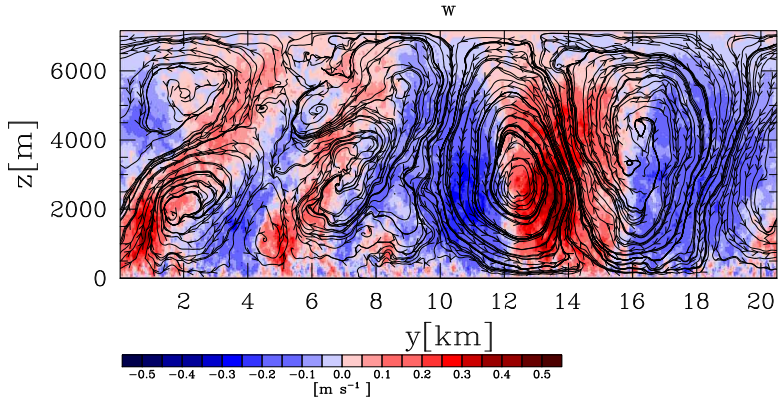

(b) E5: $\phi = 5°N$, $\alpha = 180°$

Figure 3.13.: Instantaneous vertical cross-sections of the vertical velocity w after 24 h of simulation time with a model domain height of (a) $L_z = 5220\,\text{m}$ and (b) $L_z = 7140\,\text{m}$.

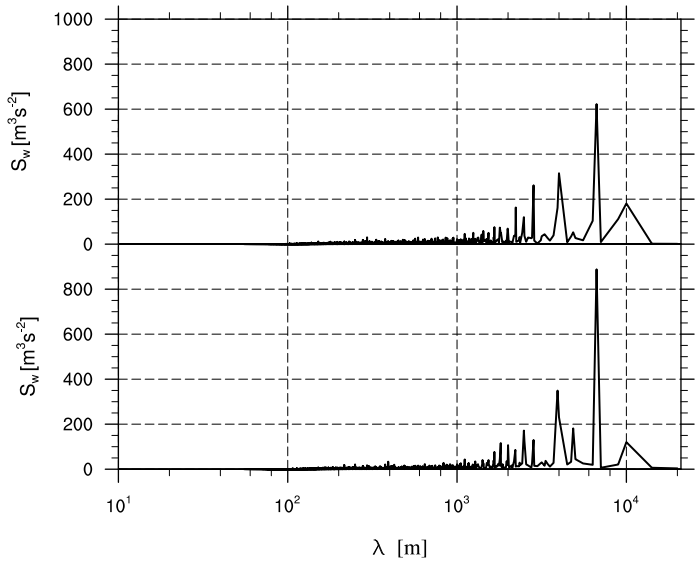

Figure 3.14.: Spectral energy density S_w of the vertical velocity w as a function of the wavelength λ calculated at $z = 1280\,\text{m}$. The spectra are arranged as in figure 3.13.

section 2.8) is used with a simulation time of 80 days for generation of a stationary wind profile. For additionally damping the inertial oscillation in the three-dimensional model, a Rayleigh damping is used within the inversion layer (see section 2.7).
Figure 3.15 shows the cross-sections of the vertical velocity for westerly and easterly winds with all modifications mentioned above. Comparing figure 3.15 with 3.2 shows that the flows have the same characteristics. For an easterly wind, the spectrum of the vertical velocity at $z = 1280\,\mathrm{m}$ is presented in figure 3.16. The largest spectral peak is at a wavelength of 6660 m. Hence, the visual analysis and the spectrum shows that the wavelength of the roll vortices is not affected by the modifications of the setup.
As shown in section 3.1.2, the wind direction has an influence on the surface stress. The averaged friction velocity u_* in E5 is 21 % larger than in W5. The difference in u_* is 7 % between E45 and W45 and vanishes for E90 and W90. This effect should remain with the modified setup. Figure 3.17a compares u_* from simulations with the setup of section 3.1.2 (black) and the modified setup (blue). The latter shows a difference between easterly and westerly winds of 17.4 % at $\phi = 5°N$, 4.4 % at $\phi = 45°N$ and nearly no difference at $\phi = 90°N$. Furthermore, the averaged friction velocity at $\phi = 5°N$ is larger for all wind directions with the modified setup.
The time series of the resolved-scale turbulent kinetic energy E^* (normalized by the number of grid points) of the setup in section 3.1.2 (black) and of the modified setup in this section (blue) are compared in figure 3.18 for the case E5. The black curve indicates that the flow reaches a stationary state after approximately 16 h of simulation time and the blue curve indicates a stationary flow after approximately 13 h of simulation time. Hence, the modified setup reaches a stationary state faster due to the one-dimensional precursor run and the Rayleigh damping as described above.
All further simulations are carried out with the modified setup.

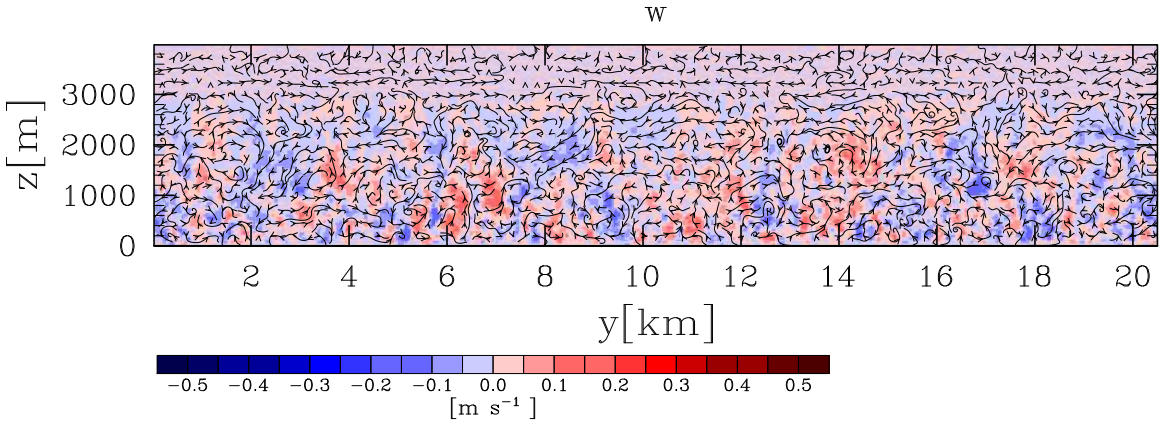

(a) W5: $\phi = 5°N$, $\alpha = 0°$

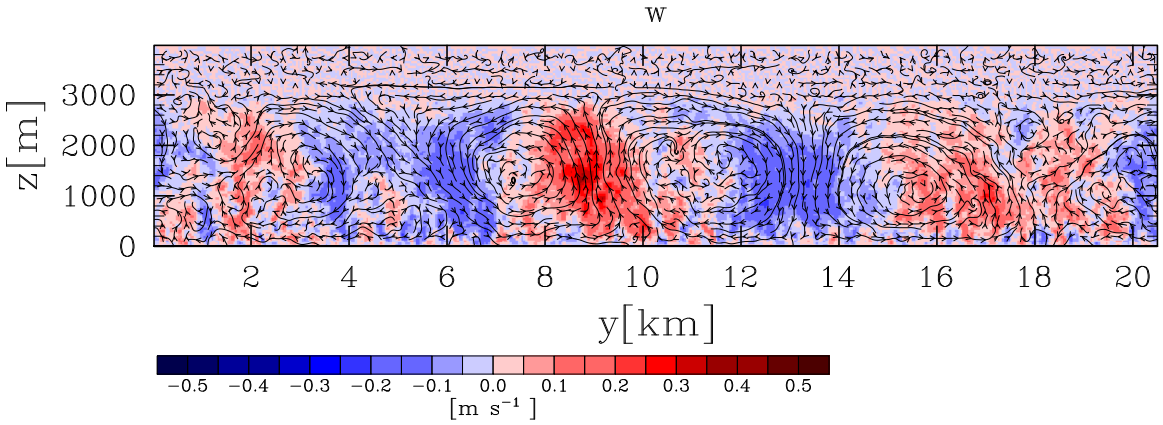

(b) E5: $\phi = 5°N$, $\alpha = 180°$

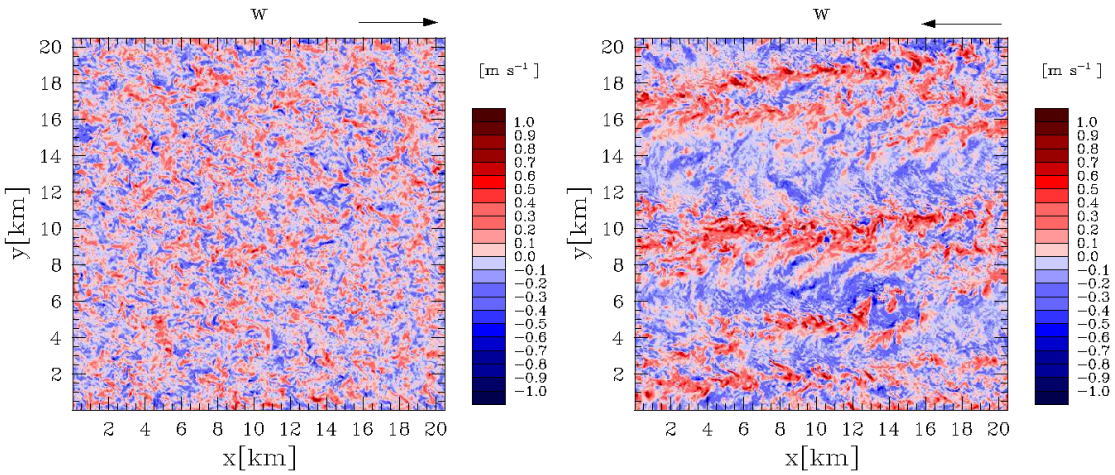

(c) W5: $\phi = 5°N$, $\alpha = 0°$ (d) E5: $\phi = 5°N$, $\alpha = 180°$

Figure 3.15.: Instantaneous cross-sections of the vertical velocity w after 24 h of simulation time. (a, b): Vertical cross-sections for (a) a westerly and (b) an easterly geostrophic wind. (c, d): Horizontal cross-sections at $z = 640$ m for (c) a westerly and (d) an easterly geostrophic wind (marked by the black arrow).

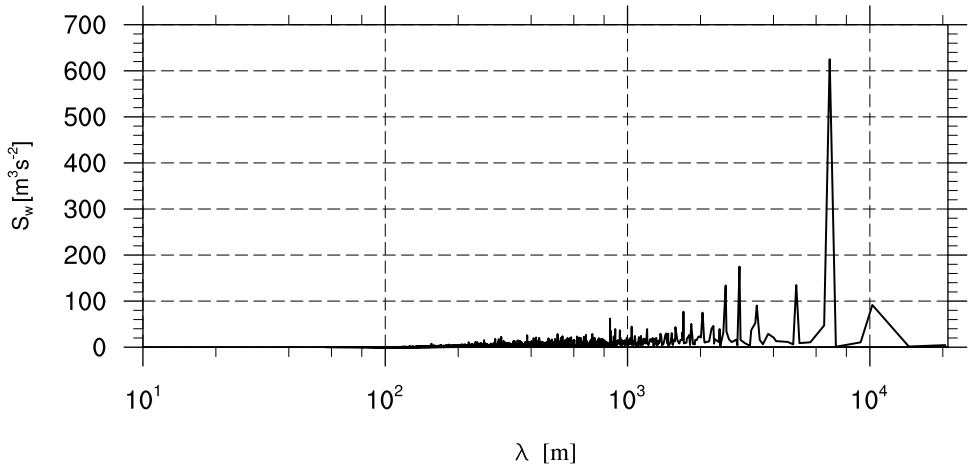

Figure 3.16.: Spectral energy density S_w of the vertical velocity w as a function of the wavelength λ calculated at $z = 1280\,\mathrm{m}$ for an easterly wind.

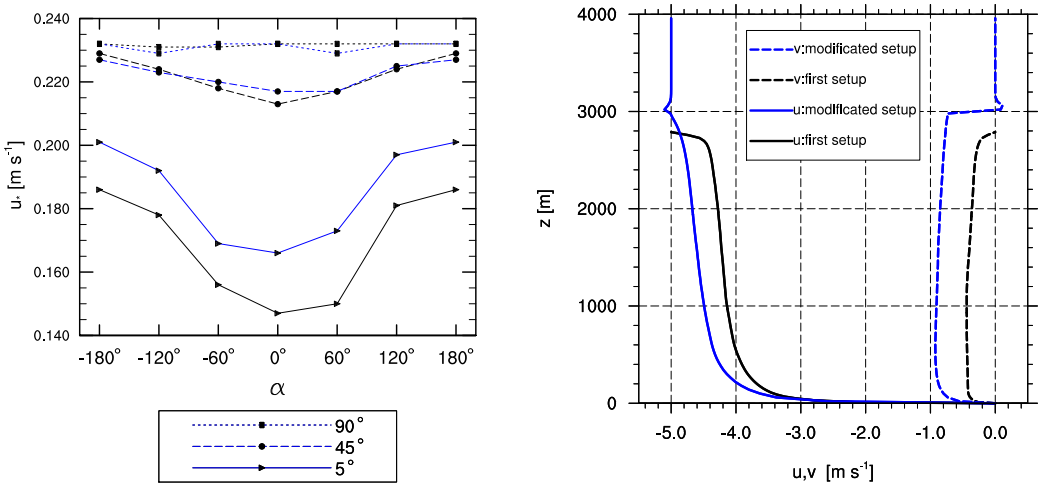

Figure 3.17.: (a) The spatially averaged friction velocity for different latitudes and wind directions with and without the inversion layer. (b) Profiles of the horizontal velocity components for different heights.

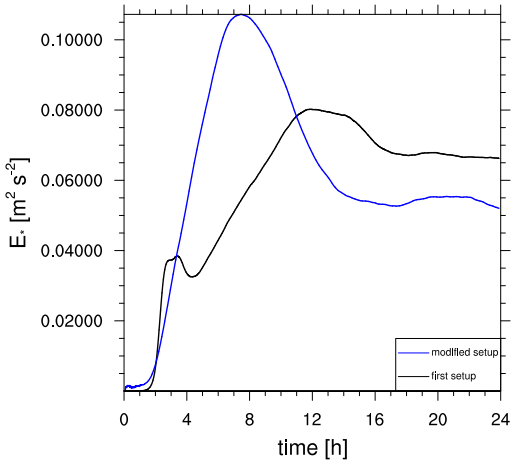

Figure 3.18.: Time series of the resolved-scale turbulent kinetic energy E^* (normalized by the number of grid points) for two different setups.

3.1.3.2. Size of the horizontal model domain

The horizontal domain sizes is varied because the estimation by Lilly (1966) leads to a wavelength of 16.8 km (see Tab. 3.3) at $\phi = 5°N$. This wavelength can hardly seen clearly with a model domain size of $L_x \times L_y = 20\,\text{km} \times 20\,\text{km}$. With the modified setup of the previous section, the horizontal model domain size of case E5 is enlarged to $L_x \times L_y = 40\,\text{km} \times 40\,\text{km}$ and $L_x \times L_y = 80\,\text{km} \times 80\,\text{km}$, both with a horizontal grid length of $\Delta x = \Delta y = 40\,\text{m}$.
Figure 3.19 presents horizontal cross-sections of the vertical velocity. These cross-section do not reveal larger roll wavelengths than in the previous sections. The visual analysis reveals an averaged wavelength $\overline{\lambda}_{r,40} \approx 6600\,\text{m}$ and $\overline{\lambda}_{r,80} \approx 7200\,\text{m}$, which confirms the averaged wavelength of the smaller horizontal domain size $\overline{\lambda}_{r,20} \approx 6600\,\text{m}$. The spectral energy density S_w is presented in figure 3.20. For a horizontal model domain sizes of 40 km, S_w has significant peaks at wavelengths between 3000 m and 6800 m and for a horizontal model domain sizes of 80 km, S_w has significant peaks at wavelengths between 3700 m and 8200 m. The results of the visual and spectral analysis are in good agreement. The results show that a horizontal domain size of 20 km is sufficiently large for resolving atmospheric roll vortices.
The most striking result of these data is that the estimation $\lambda_r \approx 19D$ by Lilly (1966) cannot be verified by these results at $\phi = 5°$ because the largest observed wavelength is 8200 m which is about half of the estimated value of 16.8 km.

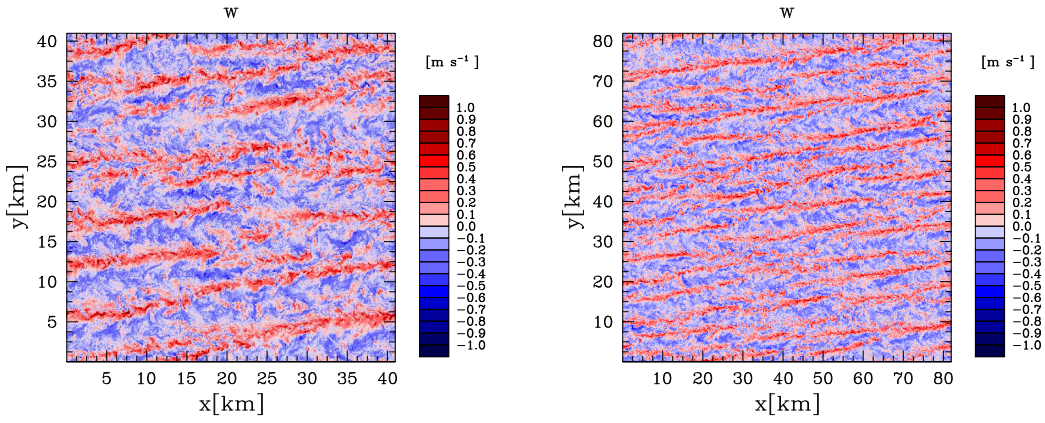

(a) E5: $\phi = 5^\circ N$, $\alpha = 180^\circ$ (b) E5: $\phi = 5^\circ N$, $\alpha = 180^\circ$

Figure 3.19.: Instantaneous horizontal cross-sections of the vertical velocity w at $z = 640\,\mathrm{m}$ after 24 h of simulation time with a horizontal model domain size of (a) $L_x \times L_y = 40\,\mathrm{km} \times 40\,\mathrm{km}$ and (b) $L_x \times L_y = 80\,\mathrm{km} \times 80\,\mathrm{km}$.

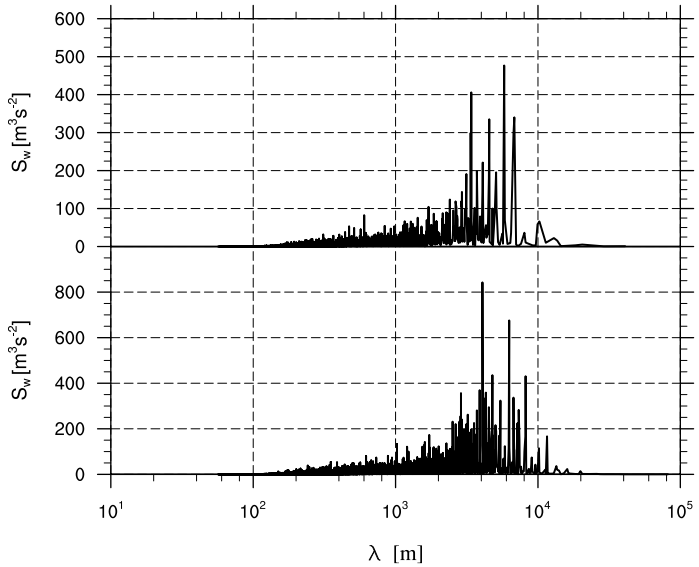

Figure 3.20.: Spectral energy density S_w of the vertical velocity w as a function of the wavelength λ calculated at $z = 1280\,\mathrm{m}$ with a horizontal model domain size of (a) $L_x \times L_y = 40\,\mathrm{km} \times 40\,\mathrm{km}$ and (b) $L_x \times L_y = 80\,\mathrm{km} \times 80\,\mathrm{km}$.

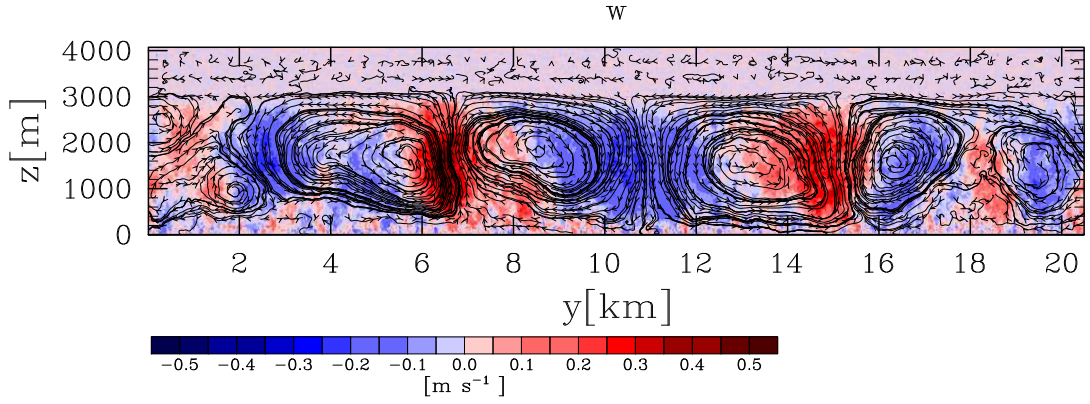

(a) $\phi = 5°N$, $\alpha = 180°$

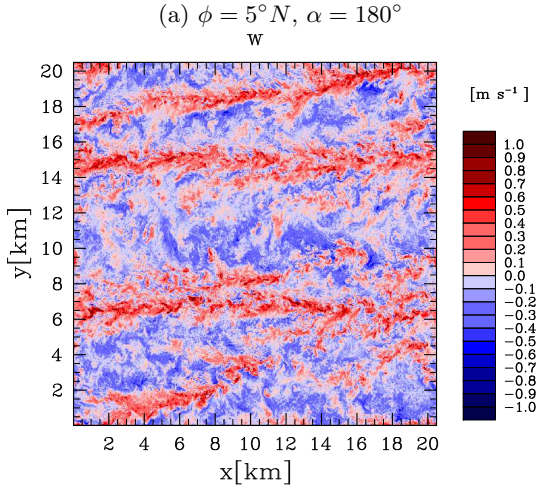

(b) $\phi = 5°N$, $\alpha = 180°$

Figure 3.21.: Instantaneous cross-sections of the vertical velocity w after 24 h of simulation time with a grid resolution of 20 m. (a) Vertical cross-section and (b) horizontal cross-section at $z = 640$ m.

3.1.3.3. Grid resolution

For the investigation of the influence of the grid resolution, the case E5 is calculated with the modified setup and a grid resolution of $\Delta x_i = 20$ m in all directions, instead of 40 m as in the previous sections. As can be seen from the vertical and horizontal cross-sections of the vertical velocity in figure 3.21, the averaged wavelength is about 6.6 km which is similar to the wavelength with $\Delta x_i = 40$ m. The spatially averaged friction velocity u_* is calculated to the value 0.2 ms^{-1} and has the same value as for $\Delta x_i = 40$ m. Hence, a grid length of 40 m in all directions is sufficiently small for the coupled simulation.

3.1.4. Calculation and analysis of the energy budget terms

The IPI is expressed in the energy budget equations 1.17 and 1.18 by the terms $-\overline{w^*u^*}\frac{\partial\overline{u}}{\partial z}$ and $-\overline{w^*v^*}\frac{\partial\overline{v}}{\partial z}$. As described in section 1.4, the term $-\overline{w^*v^*}\frac{\partial\overline{v}}{\partial z}$ produces cross-roll energy $e^*_\perp$ and supports the formation of roll vortices. The term $-\overline{w^*u^*}\frac{\partial\overline{u}}{\partial z}$ contributes to the along-roll component of the roll energy $e^*_\parallel$ and cannot induce roll vortices on its own. Energy redistribution between $e^*_\parallel$ and $e^*_\perp$ is accomplished by the Coriolis force which is denoted by the terms $-f\overline{u^*v^*}$ and $f^*\overline{u^*w^*}$ (see Eq. 1.18) and is known as PI. Using the modified setup, the energy budget terms of the IPI and PI are calculated for the cases W5, E5, W45 and E45 to investigate the conditions for the roll development.

On the left-hand side of figure 3.22, vertical profiles of the mean horizontal velocity components $\overline{u}$ and $\overline{v}$ are shown for the cases W5 and E5. The profiles are inverted for E5 for a better comparison. The terms of the IPI and PI are presented in the center column for the case E5 and on the right-hand side for the case W5. The first row shows profiles after one minute of simulation time in the three-dimensional simulation. The velocity profiles (Fig. 3.22a) are equal for E5 and W5 because they are characterized by the one-dimensional precursor run which parameterized the whole vertical transport (see section 2.8). As mentioned in section 3.1.2, this parameterization does not consider the difference between a westerly and an easterly flow. In both cases, the production term of the along-roll component of the roll energy $-\overline{w^*u^*}\frac{\partial\overline{u}}{\partial z}$ is one order of magnitude larger than the other terms. The term $-f\overline{u^*v^*}$ is negligibly small near the equator. $f^*\overline{u^*w^*}$ is positive for E5 and negative for W5 (Fig. 3.22b and 3.22c). This indicates that the vertical component of the Coriolis force redistributes kinetic energy from $e^*_\parallel$ to $e^*_\perp$ in case of E5 which supports the roll development and vice versa in case of W5. After 6 h of simulation time, a difference can be observed between the velocity profiles of W5 and E5 (Fig. 3.22d). The profiles show that the mixing of the ABL is stronger for E5 than for W5. The energy redistribution due to the vertical component of the Coriolis force $f^*\overline{u^*w^*}$ exceeds the shear production term $-\overline{w^*v^*}\frac{\partial\overline{v}}{\partial z}$ between 100 m and 1000 m (Fig. 3.22e). For W5, the Coriolis term $f^*\overline{u^*w^*}$ is negative (Fig. 3.22f). Connecting these observations with those of the cross-sections for E5 (Fig. 3.15b and 3.15d) and W5 (Fig. 3.15a and 3.15c) leads to the conclusion that the vertical component of the Coriolis force contributes to the roll development in E5.
Comparing figures 3.22g and 3.22j reveals that the flow has reached a stationary state. The velocity profiles of E5 indicate a well mixed state (Fig. 3.22j) which leads to $\frac{\partial\overline{v}}{\partial z} \approx 0$. Hence, the shear production due to $-\overline{w^*v^*}\frac{\partial\overline{v}}{\partial z}$ is nearly zero in most parts of the ABL (Fig. 3.22k). The developed rolls are maintained by the redistribution of kinetic energy from $e^*_\parallel$ to $e^*_\perp$ by the vertical component of the Coriolis force $f^*\overline{u^*w^*}$ (Fig. 3.22k). For W5, the shear production term $-\overline{w^*v^*}\frac{\partial\overline{v}}{\partial z}$ is larger than for E5 (Fig. 3.22h and 3.22k) but the negative term $f^*\overline{u^*w^*}$ indicates that the vertical component of the Coriolis force counteracts the roll development. Hence, roll vortices are not developed for W5 (see Fig. 3.15c).

Figure 3.23 shows the same quantities as figure 3.22 for E45 and W45 after 20 h of simulation time. The temporal evolution is similar to that of E5 and W5 and the differences between E45 and W45 can be discussed at the stationary state. The mixing of the boundary layer is slightly stronger for E45 than for W45 (Fig. 3.23a). However, this difference is smaller compared to that between E5 and W5. The stronger mixing for E45 can be traced back to

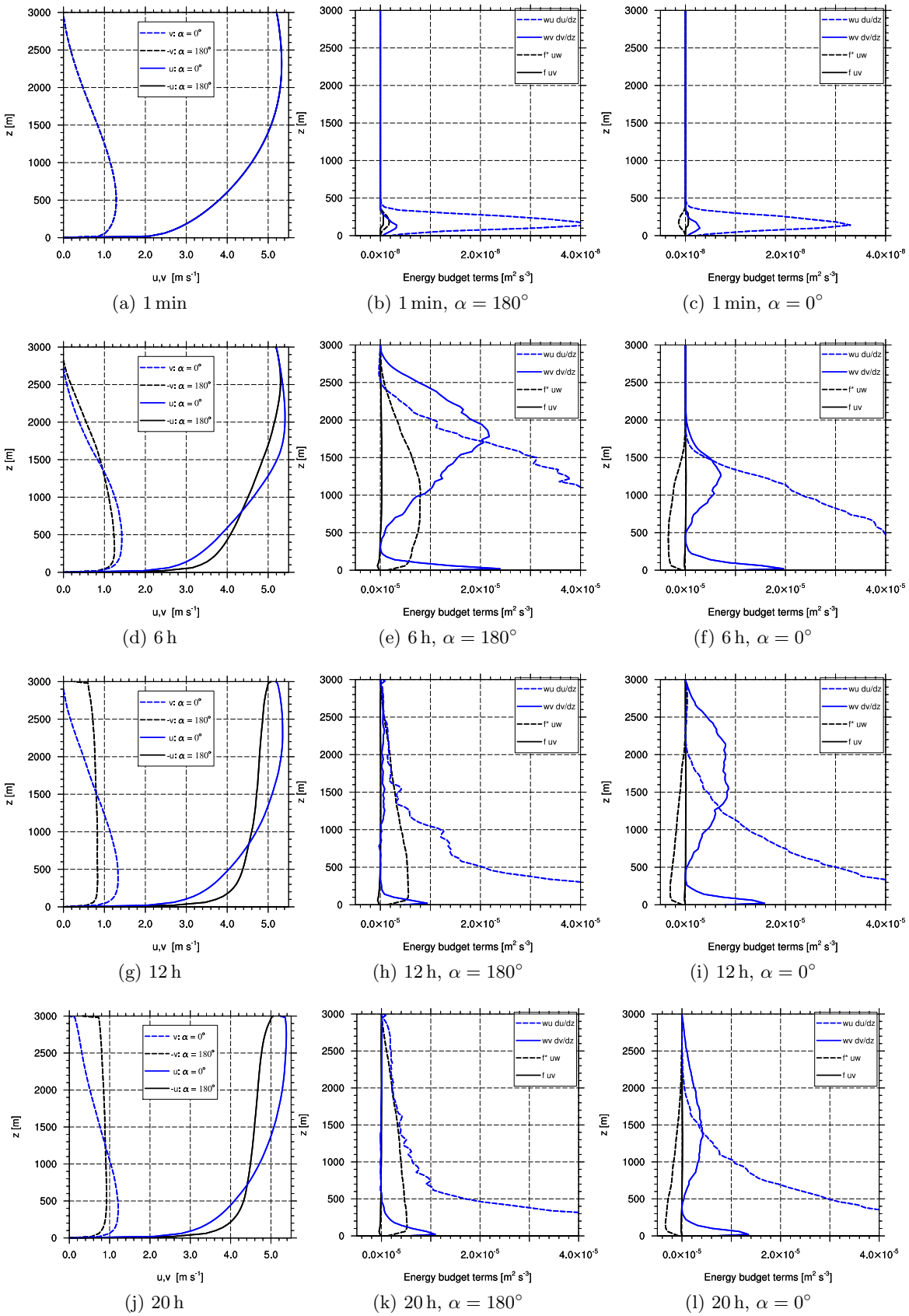

(a) 1 min (b) 1 min, $\alpha = 180°$ (c) 1 min, $\alpha = 0°$

(d) 6 h (e) 6 h, $\alpha = 180°$ (f) 6 h, $\alpha = 0°$

(g) 12 h (h) 12 h, $\alpha = 180°$ (i) 12 h, $\alpha = 0°$

(j) 20 h (k) 20 h, $\alpha = 180°$ (l) 20 h, $\alpha = 0°$

Figure 3.22.: Vertical profiles at $\phi = 5°N$ at four different times. (Left) horizontal velocity components for an easterly (inverted) and a westerly geostrophic wind. (Center) energy budget terms for an easterly and (right) a westerly geostrophic wind.

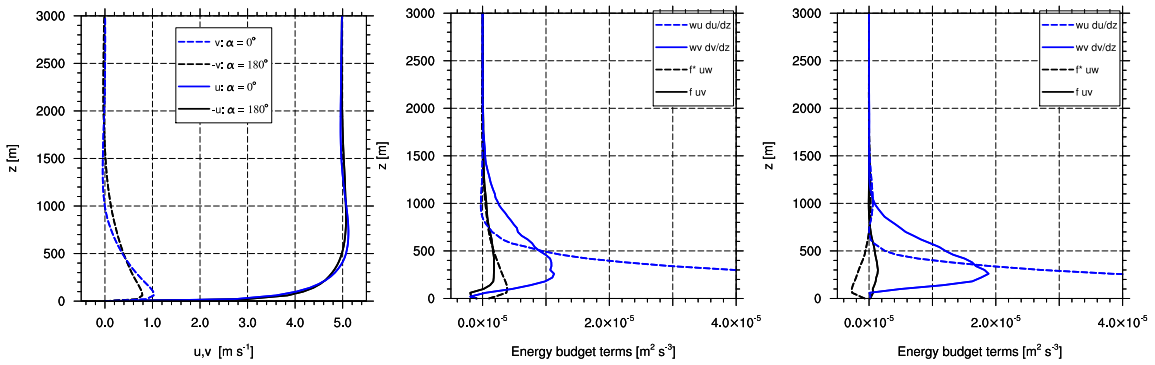

(a) 20 h (b) 20 h, $\alpha = 180°$ (c) 20 h, $\alpha = 0°$

Figure 3.23.: Vertical profiles at $\phi = 45°$ after 20 h of simulation time. (Left) horizontal velocity components for an easterly (inverted) and a westerly geostrophic wind. (Center) energy budget terms of the IPI and PI for an easterly and (right) a westerly geostrophic wind.

the stronger turbulence, roll vortices as well as unorganized turbulence, compared to W45 (see Fig. 3.7). Furthermore, the difference between the vertical profiles of the energy budget terms of E45 (Fig. 3.23b) and W45 (Fig. 3.23c) is smaller than between E5 and W5. The Coriolis term $f^*\overline{u^*w^*}$ is positive for E45 and negative for W45 but their value is smaller compared to E5 and W5 because f^* decreases with increasing latitude and is zero at the poles. The term with the horizontal component of the Coriolis force $-f\overline{u^*v^*}$ is positive for both cases. The vertical component of the Coriolis force is responsible for the different turbulence development between westerly and easterly winds, while it seems that the horizontal Coriolis component has no influence. As a consequence, this difference vanish at $\phi = 90°$ because the vertical component of the Coriolis force is zero.
These data reveal that the developed rolls in E5 and E45 are produced by the IPI and PI. The vertical component of the Coriolis force is the important part of the PI. For W5 and W45, the vertical component of the Coriolis force counteracts the roll development. For further verification of the influence of the vertical Coriolis force on the roll evolution, E5 and W5 are simulated with $f^* = 0\,\mathrm{s}^{-1}$ and the results are presented in the following section.

3.1.5. Effect of the vertical Coriolis force

The influence of the PI on the roll development is investigated for E5 and W5, where the term $-f\overline{u^*v^*}$ is insignificant compared to $f^*\overline{u^*w^*}$. f^* is set to zero and the effect of the PI becomes negligible small. The horizontal component of the Coriolis force is required for the evolution of an Ekman flow (see section 1.3).
Figure 3.24 provides horizontal and vertical cross-sections of the vertical velocity w for E5 and W5 with $f^* = 0\,\mathrm{s}^{-1}$. Roll vortices are not developed and the turbulence is unorganized in both cases. A comparison between the horizontal cross-section of the vertical velocity w from W5 with and without f^* (Fig. 3.2c and 3.24c) shows that the vertical velocity is higher for the latter case. This points to the fact that more turbulence is generated without the vertical

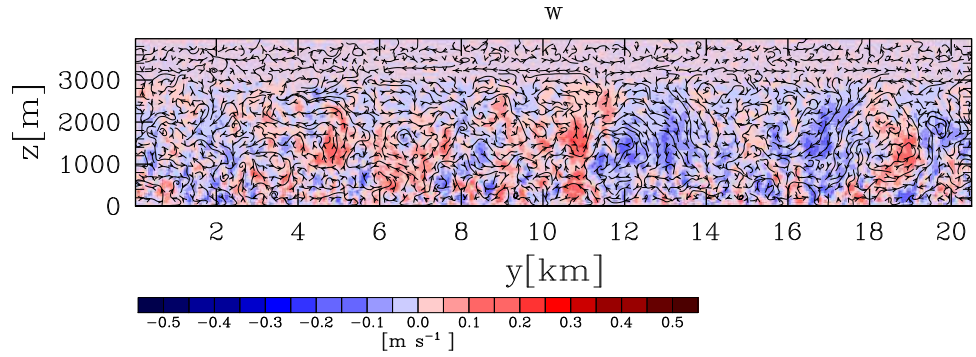

(a) $\phi = 5°N$, $\alpha = 0°$

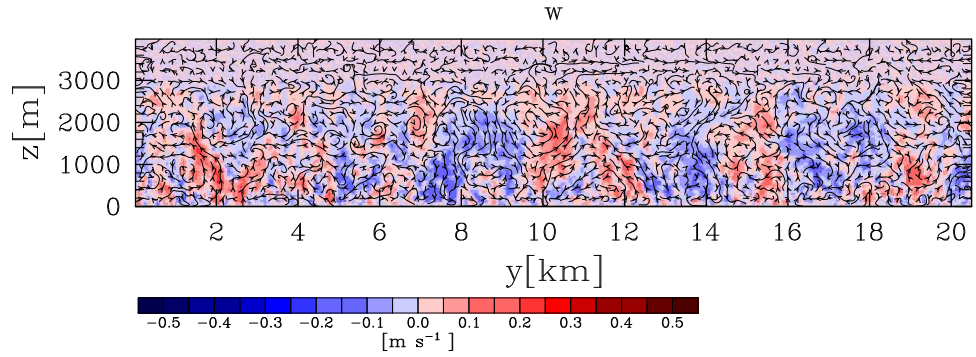

(b) $\phi = 5°N$, $\alpha = 180°$

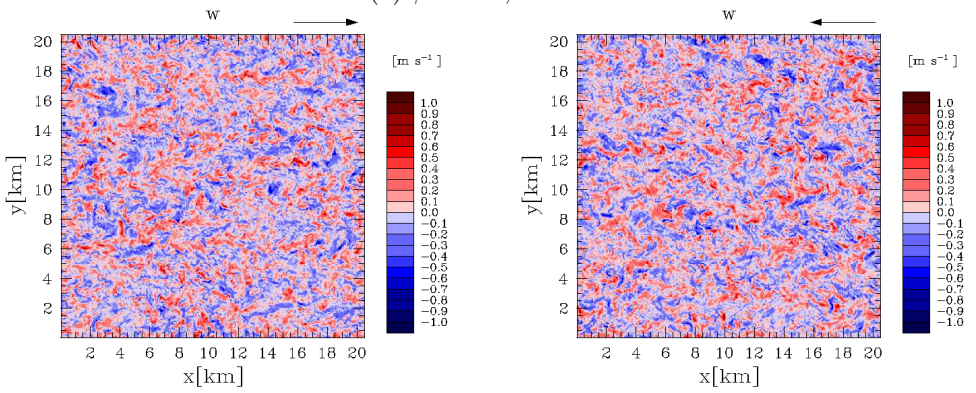

(c) $\phi = 5°N$, $\alpha = 0°$ (d) $\phi = 5°N$, $\alpha = 180°$

Figure 3.24.: Instantaneous cross-sections of the vertical velocity w after 24 h of simulation time without the vertical Coriolis force. (a, b): Vertical cross-sections at $x = 10$ km for (a) a westerly and (b) an easterly geostrophic wind. (c, d): Horizontal cross-sections at $z = 640$ m for (c) a westerly and (d) an easterly geostrophic wind (marked by the black arrow).

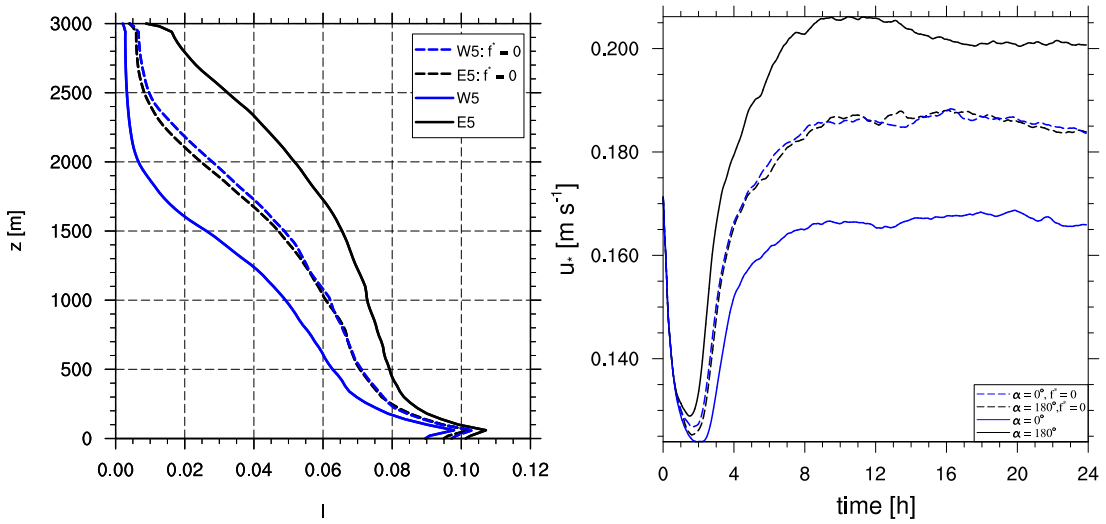

Figure 3.25.: (Left) vertical profiles of the turbulence intensity I and (right) time series of the friction velocity for E5 and W5 with and without the vertical Coriolis force.

Coriolis force for W5. The intensity of turbulence I can be calculated by (Stull, 1988):

$$I = \frac{\sigma_{|\vec{v}|}}{|\vec{v}|} = \frac{\sqrt{\frac{1}{3}(\overline{u^{*2}} + \overline{v^{*2}} + \overline{w^{*2}})}}{\sqrt{\overline{u}^2 + \overline{v}^2 + \overline{w}^2}} = \frac{\sqrt{\frac{2}{3}e^*}}{\sqrt{\overline{u}^2 + \overline{v}^2 + \overline{w}^2}} \,. \tag{3.8}$$

$\sigma_{|\vec{v}|}$ is the standard deviation of $|\vec{v}|$ and is defined as the square root of the variance (e.g. Stull, 1988). Figure 3.25a shows the vertical profiles of I for E5 and W5 with and without vertical component of the Coriolis force. The turbulence intensity is similar for E5 and W5 without the vertical component of the Coriolis force. Considering this force, I increases for E5 and decreases for W5. This effect can also be observed for the averaged friction velocity which is presented in figure 3.25b. These data lead to the conclusion that the vertical Coriolis force increases the turbulence production for an easterly wind which increases the averaged friction velocity. For a westerly wind, the vertical Coriolis force decreases the turbulence production which decreases the averaged friction velocity.

3.2. Simulation of the ocean mixed layer

3.2.1. Model validation

For the model validation, a neutrally stratified wind driven OML without wave breaking and Langmuir circulation is simulated and compared with LES results by Noh et al. (2004) who used the same setup. The model domain size is $L_x \times L_y \times L_z = 300\,\mathrm{m} \times 300\,\mathrm{m} \times 80\,\mathrm{m}$ with a grid length Δx_i of 1.25 m in all directions. The potential temperature is set to 300 K and the salinity to zero in the entire model domain. The ocean is driven by a spatially and temporally constant momentum flux at the sea surface with $\overline{wu}_{0,o} = 1 \times 10^{-4}\,\mathrm{m^2\,s^{-2}}$ and $\overline{wv}_{0,o} = 0\,\mathrm{m^2\,s^{-2}}$. The friction velocity $u_{*,o}$ is calculated by:

$$u_*^2 = \sqrt{\overline{wu}_0^2 + \overline{wv}_0^2}\,, \tag{3.9}$$

and has the value $0.01\,\mathrm{m\,s^{-1}}$. The simulation is carried out for $\phi = 55°N$, and the simulation time is 8 h.

Figure 3.26 shows vertical profiles of the mean horizontal velocity which are averaged over the last 600 s of the simulation time. The figure compares results of the present study with results by Noh et al. (2004) and shows that the profiles are similar. The amount of both velocity components is maximal at the sea surface where the OML is driven by the wind stress. Although $\overline{wv}_{0,o}$ is zero the ocean current is deflected in y-direction caused by the Coriolis force. In the first 10 m below the sea surface, the u component strongly decreases with depth. Beneath, the velocity gradient is smaller and both velocity components are close to zero at a depth of approximately 60 m. Near the surface, the gradient of the v component is smaller due to the absence of a surface stress in the y-direction. Figure 3.27 compares vertical and horizontal cross-sections of the vertical velocity w between the simulation of the present study and Noh et al. (2004). The magnitude of w is equal and the turbulence is unorganized in both simulations.
The comparison with the study by Noh et al. (2004) shows that the ocean version of PALM can reproduce a neutrally stratified wind driven Ekman flow within the OML.

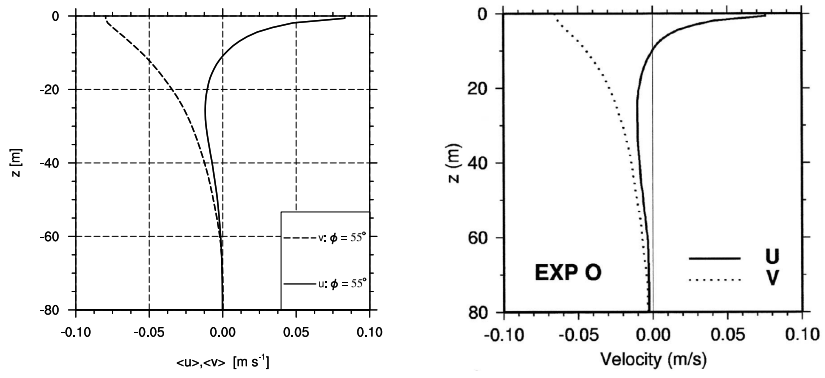

(a) Present study (b) Noh et al. (2004)

Figure 3.26.: Vertical profiles of the mean horizontal velocity components at $\phi = 55°N$ after 8 h of simulation time. The profiles are averaged over the last 600 s of simulation time. "EXP O" in (b) marks the case without Langmuir circulation and wave breaking.

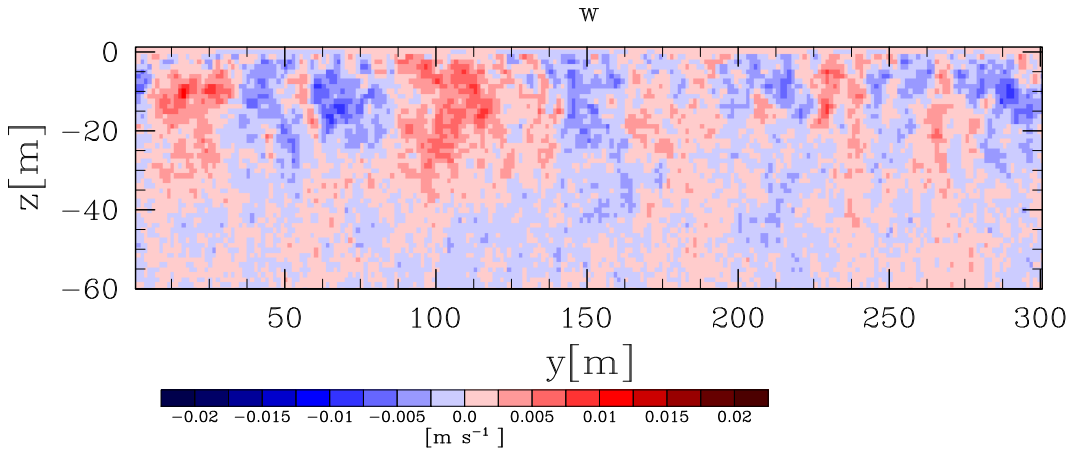

(a) Present study

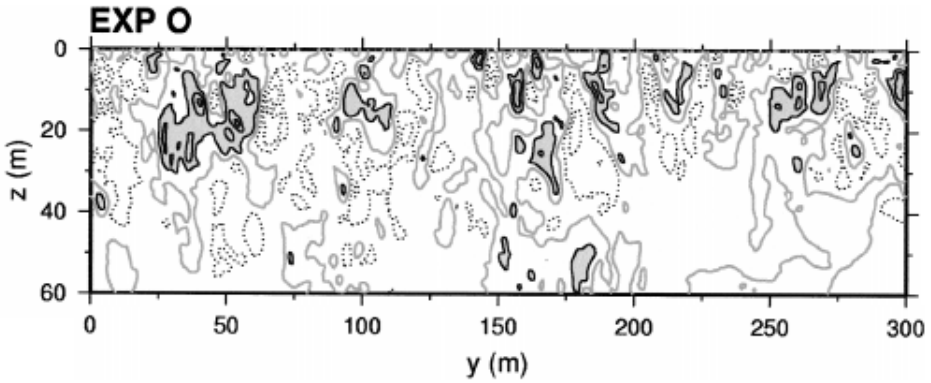

(b) (Noh et al., 2004)

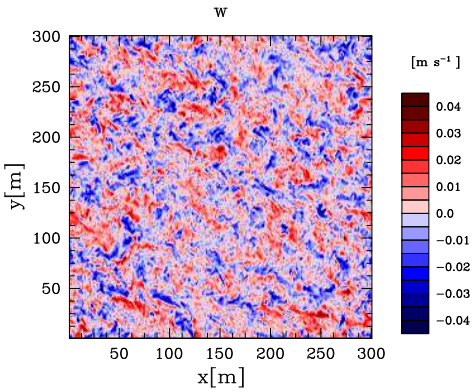

(c) Present study

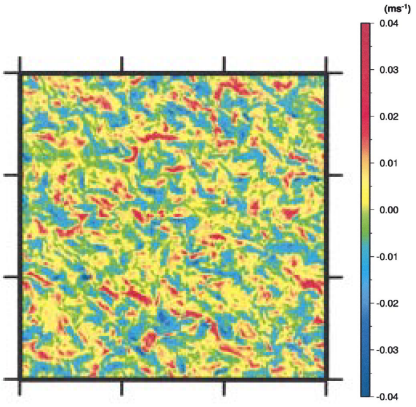

(d) Noh et al. (2004)

Figure 3.27.: Instantaneous cross-sections of the vertical velocity w after 8 h of simulation time. (a,b) Vertical cross-sections averaged along the x-axis. It should be noted that the values on the z-axis differs between both studies. For the present study, the values are negative and for Noh et al. (2004), these values are positive. (b) Solid lines represent downward and dotted lines upward motions. Contour levels are $0.01\,\mathrm{m\,s^{-1}}$. The grey line marks zero. Downward regions exceeding $0.01\,\mathrm{m\,s^{-1}}$ are shaded. (c,d) Horizontal cross-sections at $z = -10\,\mathrm{m}$ and $z = 10\,\mathrm{m}$, respectively.

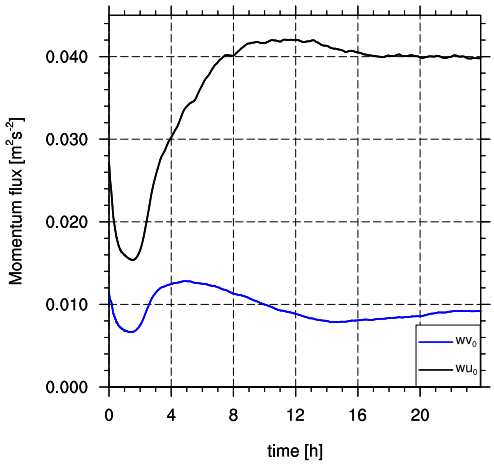

Figure 3.28.: Time series of the horizontally averaged momentum flux at the sea surface of the atmospheric simulation E5.

3.2.2. General results

In preparation for the coupled simulation, the setup of the model validation, described in section 3.2.1, is adjusted to the situation with the strongest roll vortices in the atmosphere. This case is at $\phi = 5°N$ for an easterly wind (E5), as shown in section 3.1.2. The components of the horizontally averaged vertical momentum flux at the surface $\overline{wu}_{0,a}$ and $\overline{wv}_{0,a}$ are taken from that simulation and used as spatially and temporally constant surface stress for all following oceanic simulations. The time series of $\overline{wu}_{0,a}$ and $\overline{wv}_{0,a}$ from the atmospheric simulation E5 are shown in figure 3.28. These values have to be multiplied by ρ_a/ρ_o as indicated in equation 2.85 and 2.86. Hence, the momentum fluxes are $\overline{wu}_{0,o} = 4 \times 10^{-5}\,\mathrm{m^2\,s^{-2}}$ and $\overline{wv}_{0,o} = 9 \times 10^{-6}\,\mathrm{m^2\,s^{-2}}$, resulting in a friction velocity of $u_{*,o} = 6.4 \times 10^{-3}\,\mathrm{m\,s^{-1}}$, which is one order of magnitude smaller than the validation simulation in section 3.2.1. The surface stress is reduced because it is adjusted to the values of the atmospheric simulation E5 in section 3.1.2. The model domain size is $L_x \times L_y \times L_z = 480\,\mathrm{m} \times 480\,\mathrm{m} \times 160\,\mathrm{m}$ with a grid length Δx_i of 1.25 m in all directions. The vertical model domain size is extended compared to the previous simulation because the depth of the Ekman layer increases with decreasing latitudes (e.g. Stewart, 2008). The simulation time is 24 h.

Figure 3.29a shows the vertical profiles of the mean horizontal velocity components $\overline{u}$ and $\overline{v}$. The mean horizontal flow strongly decreases within the first 15 m below the sea surface. The mean value of the u component is larger than the mean value of the v component because $\overline{wu}_{0,o}$ is larger than $\overline{wv}_{0,o}$. Beneath $z = -15\,\mathrm{m}$, the horizontal velocity varies slightly down to the model bottom which indicates a well mixed boundary layer. Furthermore, the velocity profiles indicate that the OML depth is larger than the model domain because the mean horizontal velocity is not zero at the bottom of the model domain. For a comparison, the Ekman depth D, determined from laboratory experiments, can be estimated by (e.g. Thorpe, 2005):

$$D = 0.4\frac{u_*}{f}\,. \tag{3.10}$$

f is calculated using equation 1.3. At $\phi = 5°N$, f is $1.27 \times 10^{-5}\,\mathrm{s^{-1}}$ which leads to $D \approx 200\,\mathrm{m}$. Hence, the large Ekman depth of the simulated flow is in agreement with laboratory exper-

iments. Further investigations on the Ekman depth are not done in this study because the depth of 200 m cannot be realized for the coupled simulation due to the large amount of computational costs .
Figure 3.29b provides the time series of the resolved-scale turbulent kinetic energy E^* (normalized by the number of grid points). The energy increases in the first 22 hours and then starts to decrease. This is a first sign for a stationary state but a longer simulation time would be necessary for a clear statement. Anyhow, the time series shows the long time scales for reaching a stationary state at this latitude. A longer simulation time is not carried out because the coupled simulation needs a large amount of computational costs so that a simulation time of 24 h is too long for the coupled simulation. Instead, sensitivity studies are shown in section 3.2.3 for reducing the computational costs of the coupled simulation.

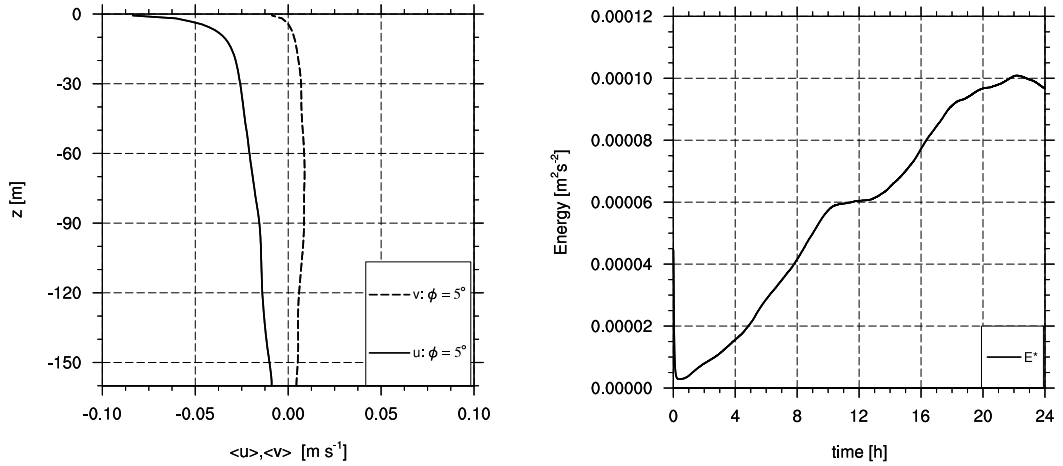

(a) (b)

Figure 3.29.: (a) vertical profiles of the mean horizontal velocity components at $\phi = 5°$ after 24 h of simulation time. (b) time series of the resolved-scale turbulent kinetic energy E^* (normalized by the number of grid points).

Figure 3.30 shows instantaneous cross-sections of the vertical velocity w and streamlines of (v^*, w^*). Strong coherent upwelling zones (red) and downwelling zones (blue) can be observed in the vertical cross-sections after 12 h and 24 h of simulation time (Fig. 3.30a and 3.30b). A comparison between the two times shows that these coherent structures grow with time and their vertical extension ranges over the entire model depth at $t = 24$ h. Figures 3.30c - 3.30e presents horizontal cross-sections of w in three different depths which reveal that the upwelling and downwelling zones are oriented in long bands. Hence, roll structures are developed which are comparable to roll vortices in the ABL. The spatially averaged wavelength of all roll pairs $\overline{\lambda}_r$ is 240 m at $t = 24$ h.
Figure 3.31 shows variance spectra of the vertical velocity after 12 h and 24 h of simulation time. At $t = 12$ h, S_w has peaks at wavelengths between 30 m and 116 m at $z = 15$ m and between 50 m and 116 m at $z = 85$ m (Fig. 3.31a). At $t = 24$ h, the peaks of S_w are at $\lambda = 240$ m and $\lambda = 110$ m which is in good agreement with the visual analysis. The comparison between $t = 12$ h and $t = 24$ h shows that the roll vortices are not completely developed at $t = 12$ h. Comparing the oceanic roll wavelength with the atmospheric roll wavelength reveals

that the atmospheric wavelength is one order of magnitude larger than the oceanic wavelength.

It should be noted that the rolls develop without waves at the sea surface. Hence, they cannot be termed as Langmuir circulation after the theory of Craik and Leibovich (1976). Instead, it is supposed that the dynamical instability mechanisms, such as IPI and PI, are responsible for the roll circulations and that the vertical Coriolis force has the same effect as in the ABL. Figure 3.32 presents the energy budget terms referring to the IPI and PI after 12 h and 24 h of simulation time. The terms are multiplied with the density ρ_o in order to be comparable with the atmosphere. At both times, the first 10 m below the sea surface are dominated by the IPI with the term $-\overline{w^*v^*}\frac{\partial \overline{v}}{\partial z}$ which becomes insignificant in greater depths. The vertical component of the Coriolis force, denoted by the term $f^*\overline{u^*w^*}$, dominates below $z = -10\,\mathrm{m}$ and transports the energy from $e^*_{\parallel}$ to $e^*_{\perp}$. The energy of $e^*_{\parallel}$ is produced by the flow shear along the roll axis, denoted by the term $-\overline{w^*u^*}\frac{\partial \overline{u}}{\partial z}$. This shows that the roll vortices in the OML are produced by the IPI and PI.

Zikanov et al. (2003)[2] also investigated a neutrally stratified wind driven OML without wave breaking and Langmuir circulation for different latitudes and wind directions using LES. They showed that the vertical mixing of momentum has a maximum for north-east winds and a minimum for south-west winds and that the difference between these extrema increases with decreasing latitudes. Zikanov et al. (2003) showed that the influence of the vertical component of the Coriolis force on the unorganized turbulence production is responsible for this effect. In contrast to this study, Zikanov et al. (2003) did not observe large coherent structures in the flow which might be caused by the coarse grid resolution. The grid length of Zikanov et al. (2003) varied with latitude and their smallest grid length was approximately 8 m. The influence of the grid resolution on the development of large coherent structures is investigated in the following section.

3.2.3. Sensitivity study

The aim of this study is a coupled atmosphere-ocean simulation with a horizontal domain size of 20 km in both horizontal directions which is sufficiently large to resolve roll vortices in the ABL. With a grid length of 1.25 m, one horizontal layer in the ocean contains 2.56×10^8 grid points. With 128 grid layers in the vertical direction, this results in 3.28×10^{10} grid points. To reach a stationary state, a simulation time of approximately 22 h is necessary as shown in the previous section. To minimize the total number of grid points and the simulation time for reaching a stationary state, a sensitivity study with various OML depths and grid resolutions is carried out.

3.2.3.1. Depth of the ocean mixed layer

To eliminate an effect of the vertical model domain size on the flow characteristics, a temperature inversion of 5 K/100m is defined below the OML. This inversion represents the seasonal thermocline in the deep ocean. The inversion depth z_{inv} is varied to find the minimum depth

[2]The angle of the wind direction γ should be replaced by $-\gamma$ for a correct reading of the paper by Zikanov et al. (2003). Therefore, the terms “west” and “east” should be interchanged in their text. This circumstance was already recognized by Gerkema et al. (2008).

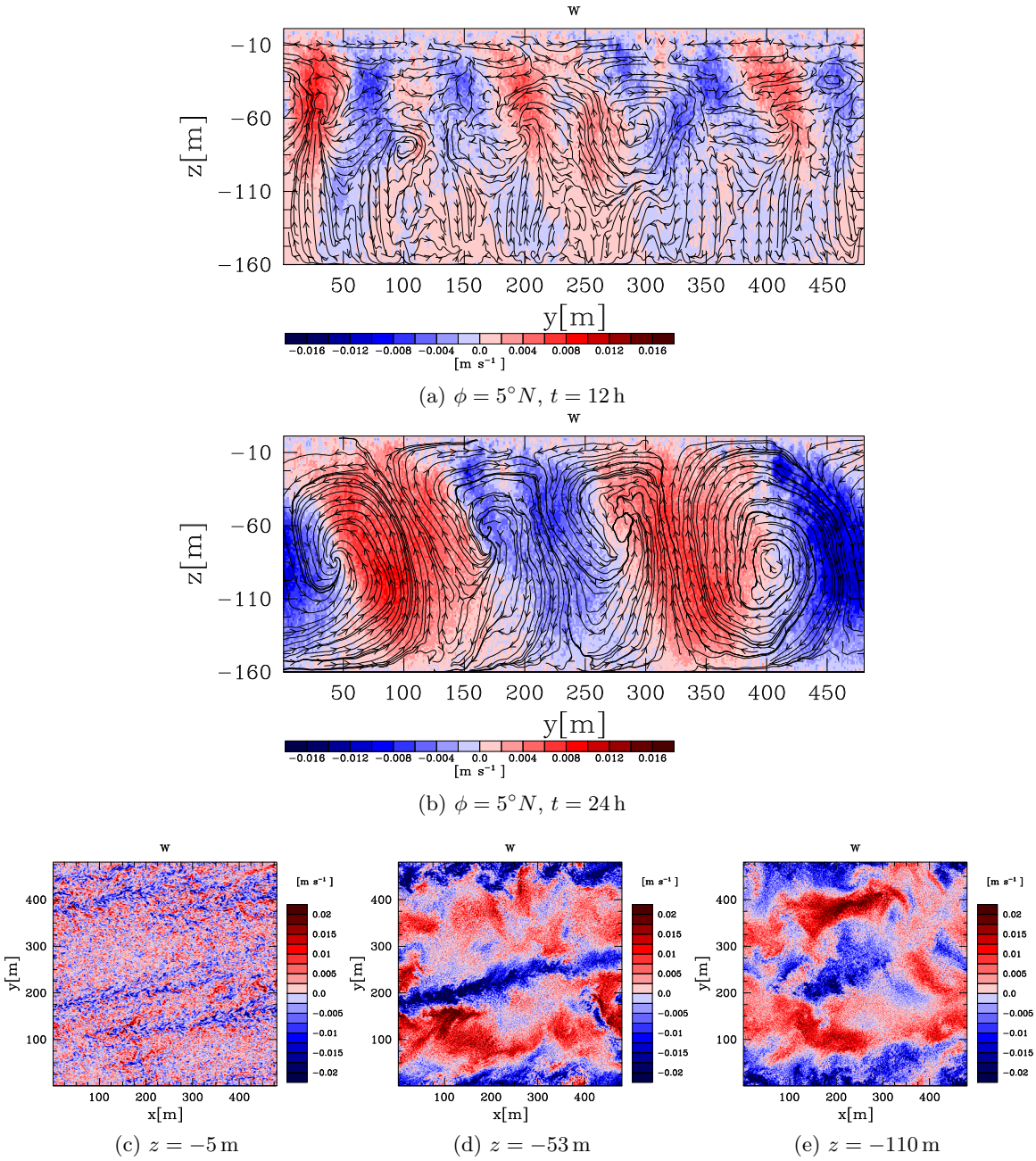

(a) $\phi = 5°N$, $t = 12\,\mathrm{h}$

(b) $\phi = 5°N$, $t = 24\,\mathrm{h}$

(c) $z = -5\,\mathrm{m}$ (d) $z = -53\,\mathrm{m}$ (e) $z = -110\,\mathrm{m}$

Figure 3.30.: Instantaneous cross-sections of the vertical velocity w. (a, b) vertical cross-sections averaged along the x-axis and streamlines of (v^*, w^*) after (a) 12 h and (b) 24 h of simulation time. (c-e) horizontal cross-sections after 24 h of simulation time at different depths.

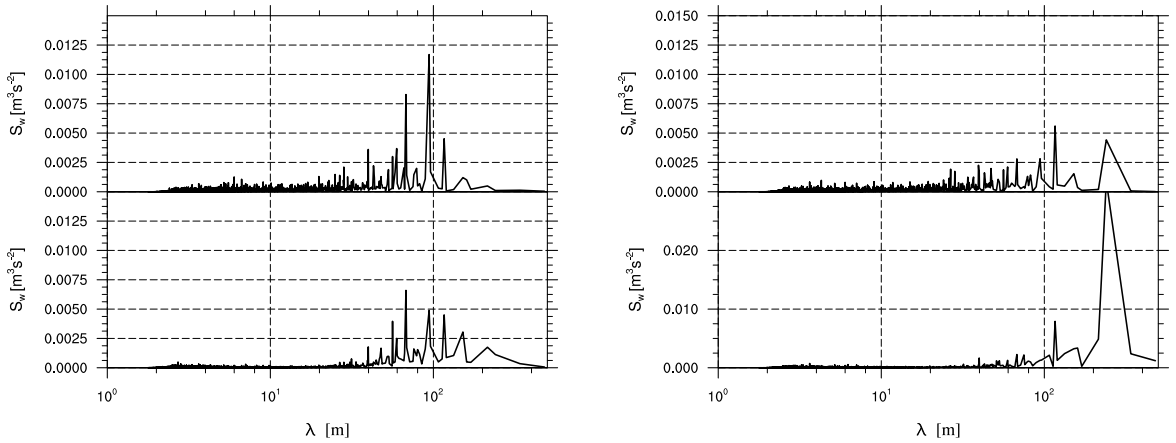

Figure 3.31.: Spectral energy density S_w of the vertical velocity w as a function of the wavelength λ calculated at $z = -15\,\mathrm{m}$ at $\phi = 5°N$ after (a) 12 h and (b) 24 h of simulation time. Upper spectra are taken at $z = 15\,\mathrm{m}$ and lower spectra at $z = 85\,\mathrm{m}$.

where roll vortices develop. Therefore, three simulations are carried out with the setup given in section 3.2.2 with different vertical domain sizes. The simulations have a model domain depth of $L_z = 40\,\mathrm{m}$, $L_z = 50\,\mathrm{m}$ and $L_z = 60\,\mathrm{m}$ with an OML depth of 30 m, 40 m and 50 m, respectively. The simulation time is 12 h.

Figure 3.33a shows vertical profiles of the mean horizontal velocity components. A well mixed OML is indicated by the profiles in all three cases. The time series of E^* in figure 3.33b reveals that the maximum is shifted to the right of the time axis with increasing OML depth. Hence, the time for reaching a stationary state increases with increasing OML depth. The difference between neighboring maxima is approximately one hour. This result show that reducing the OML depth provides the advantage of reducing the time for reaching a stationary state, which saves computational costs.

Comparison of the instantaneous cross-sections of different OML depths (Fig. 3.34) shows that the turbulence organization increases with larger OML depths. For $z_{inv} = -30\,\mathrm{m}$ (Fig. 3.34d), the bands of downwelling zones are not coherent over the whole model domain along the x-axis, while this is the case for $z_{inv} = -40\,\mathrm{m}$ and $z_{inv} = -50\,\mathrm{m}$ (Fig. 3.34e and 3.34f). The difference between the three inversion depths is also visible in the spectral energy density S_w in figure 3.35. The largest peak of S_w is at $\lambda = 116\,\mathrm{m}$ for $z_{inv} = -40\,\mathrm{m}$ and $z_{inv} = -50\,\mathrm{m}$, whereas S_w has not a statistically significant peak for $z_{inv} = -30\,\mathrm{m}$. The wavelength $\lambda = 116\,\mathrm{m}$ resulting from the spectral peaks are in good agreement with an visual analysis of the wavelength in figures 3.34e and 3.34f. The results show that an OML depth of $z_{inv} = -30\,\mathrm{m}$ is not adequate under the given circumstances for producing clear roll structures. Hence, an OML depth of 40 m is necessary for the production of roll vortices in a neutrally stratified Ekman flow.

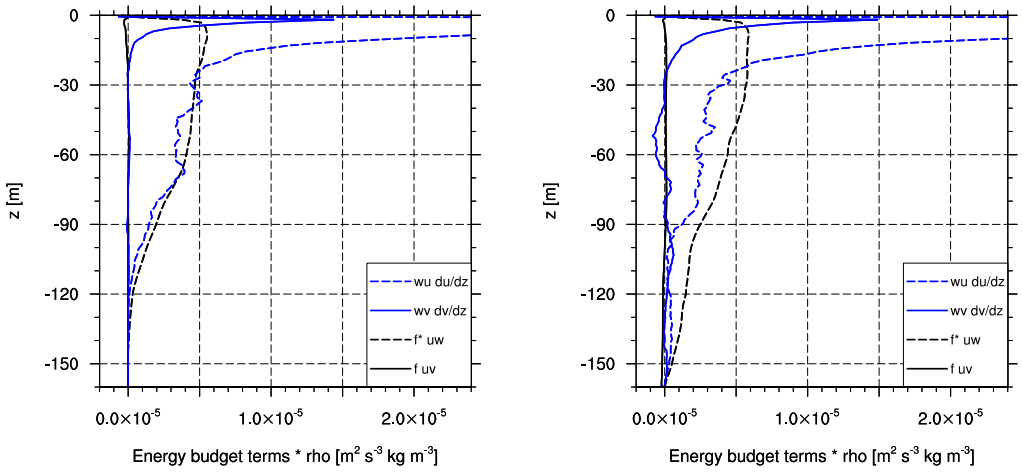

(a) $t = 12\,\mathrm{h}$ (b) $t = 24\,\mathrm{h}$

Figure 3.32.: Energy budget terms of the IPI and PI at $\phi = 5°N$.

3.2.3.2. Grid resolution

The total number of grid points of a simulation can be reduced by a lower grid resolution. To investigate the influence of the grid resolution on the roll development, Δx_i is varied to the values 1 m, 1.25 m and 1.5 m in all directions. The model domain size is $L_x \times L_y \times L_z = 240\,\mathrm{m} \times 240\,\mathrm{m} \times 60\,\mathrm{m}$ with a temperature inversion of $5\,\mathrm{K}/100\mathrm{m}$ at a depth of 50 m.

Figure 3.36 shows the cross-sections of the vertical velocity w of the three simulations with different grid resolutions. Comparing the vertical and horizontal cross-sections reveals that the roll vortices can be identified in the whole model domain with a grid resolution of 1 m and 1.25 m. Only one vortex pair can be seen in the cross-sections for a grid resolution of 1.5 m and in the other part of the domain, large coherent structures cannot be observed. Hence, a grid resolution of 1.25 m is nearly the coarsest resolution for observations of large coherent structures in the OML. It should be noted that these results confirm the assumption that the grid length used by Zikanov et al. (2003) was not small enough for observating large coherent structures in the OML.

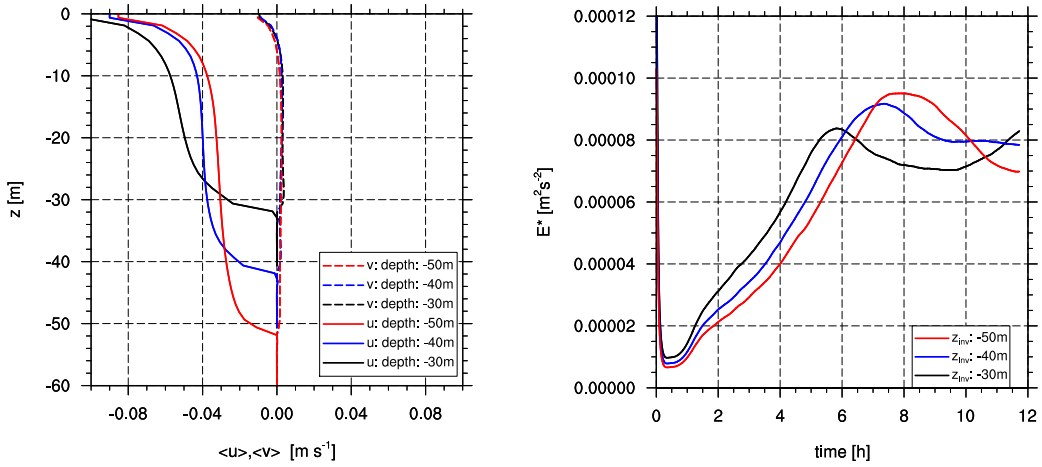

(a) (b)

Figure 3.33.: (a) Vertical profiles of the mean horizontal velocity components $\overline{u}$ and $\overline{v}$ after 12 h of simulation time and (b) time series of the resolved-scale turbulent kinetic energy E^* (normalized by the number of grid points) at $\phi = 5°$ for different OML depths.

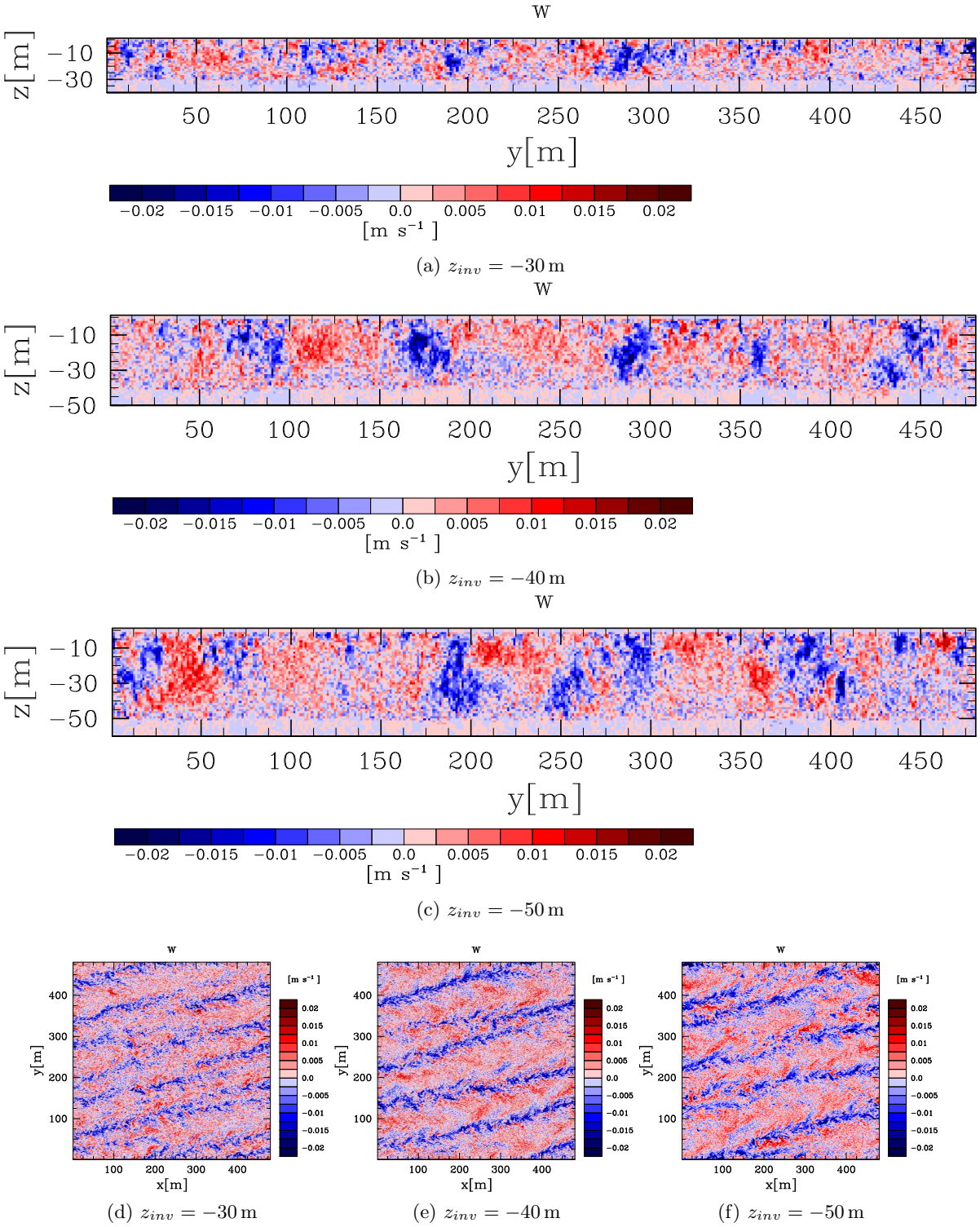

(a) $z_{inv} = -30\,\mathrm{m}$

(b) $z_{inv} = -40\,\mathrm{m}$

(c) $z_{inv} = -50\,\mathrm{m}$

(d) $z_{inv} = -30\,\mathrm{m}$

(e) $z_{inv} = -40\,\mathrm{m}$

(f) $z_{inv} = -50\,\mathrm{m}$

Figure 3.34.: Instantaneous cross-sections of the vertical velocity w after 12 h of simulation time for different OML depths. (a, b, c) Vertical cross-sections at $x = 225\,\mathrm{m}$. (d, e, f) Horizontal cross-sections at $z = 15\,\mathrm{m}$.

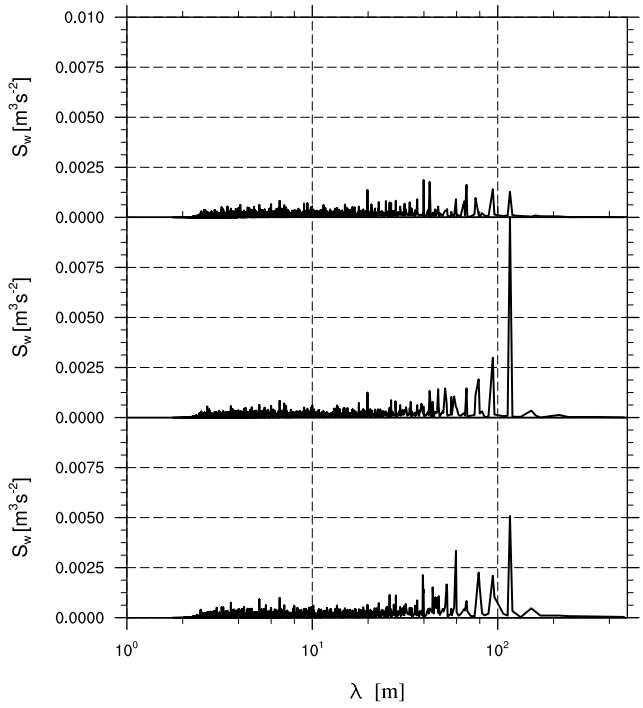

Figure 3.35.: Spectral energy density S_w of the vertical velocity w as a function of the wavelength λ calculated at $z = -15\,\mathrm{m}$ at $\phi = 5°N$ for different OML depths. The spectra refer to figure 3.34a - 3.34c.

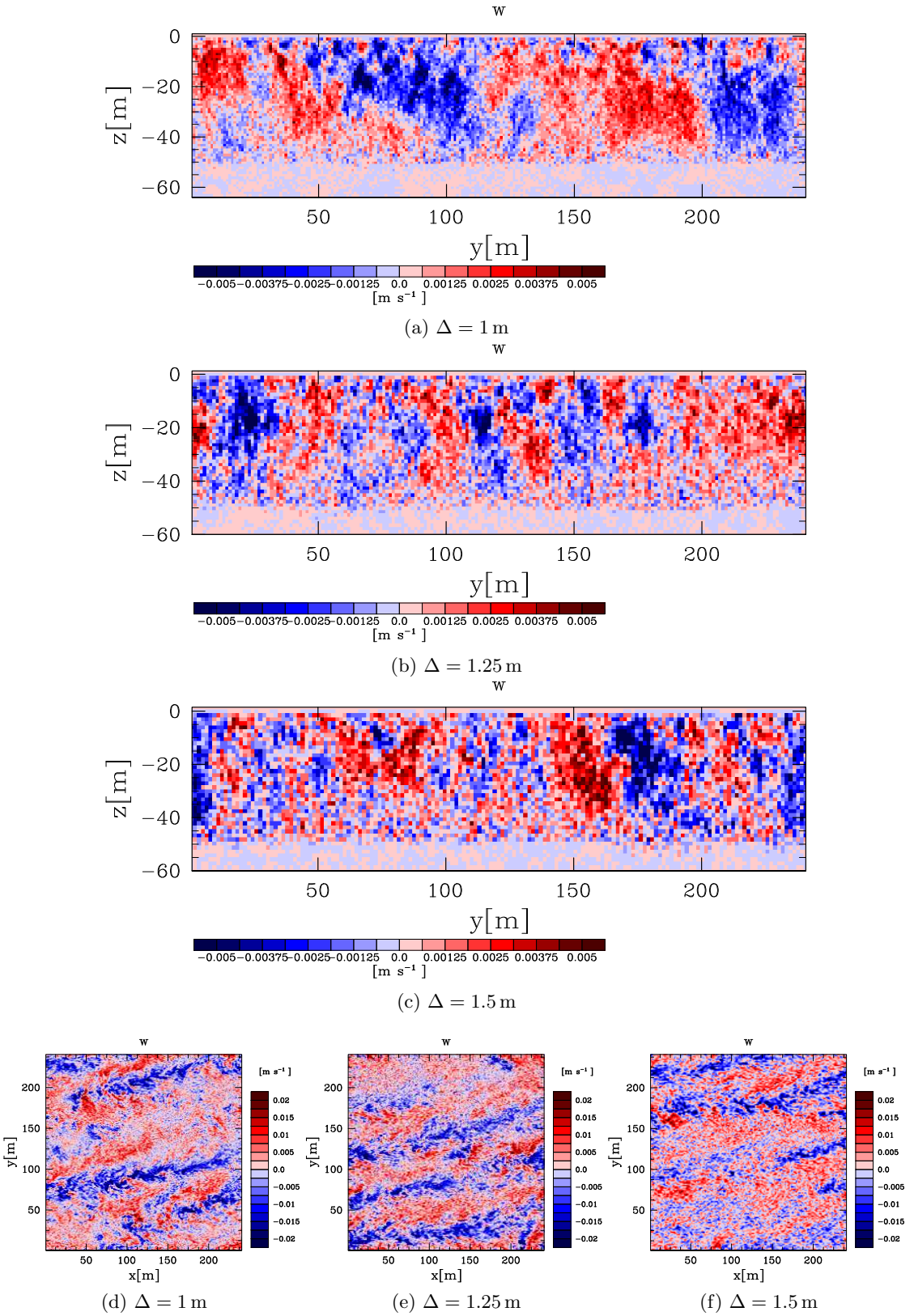

(a) $\Delta = 1\,\mathrm{m}$

(b) $\Delta = 1.25\,\mathrm{m}$

(c) $\Delta = 1.5\,\mathrm{m}$

(d) $\Delta = 1\,\mathrm{m}$

(e) $\Delta = 1.25\,\mathrm{m}$

(f) $\Delta = 1.5\,\mathrm{m}$

Figure 3.36.: Instantaneous cross-sections of the vertical velocity w at $\phi = 5°N$ after 12 h of simulation time for different grid resolutions. (a, b, c) Vertical cross-sections at $x = 225\,\mathrm{m}$. (d, e, f) Horizontal cross-sections at $z = 15\,\mathrm{m}$.

3.3. The Parallel Instability in the coupled atmosphere-ocean system

The influence of atmospheric roll vortices on the oceanic flow structure is investigated in this section. Therefore, two questions shall be examined. Do atmospheric roll vortices with wavelengths between 5 km and 10 km induce oceanic roll vortices of the same wavelength? Do atmospheric roll vortices affect oceanic roll structures with wavelengths of about 100 m?

3.3.1. Setup

The setup of the coupled atmosphere-ocean simulation is based on the atmospheric and oceanic studies of section 3.1 and 3.2, especially on the sensitivity studies. A neutrally stratified atmospheric Ekman flow at $\phi = 5°$ with an easterly geostrophic wind is used for the coupled simulation because the roll vortices develop parallel to the x-axis, which simplifies the analysis. The simulation is divided into two parts: an uncoupled precursor run, where the atmospheric and oceanic flow is simulated without a data exchange at the sea surface, and the coupled simulation. The uncoupled precursor run is simulated until the resolved-scale turbulent kinetic energy E^* reaches a stationary state in both flows. The simulation time of the uncoupled precursor run is 12 h and 7 h for the coupled simulation, resulting in a total simulation time of 19 h. The coupling interval $\Delta t_{coupling}$ is 30 s in order that the interval is larger than the time steps of the atmosphere model and the ocean model (see Fig. 3.37).
The setup has to fulfill several model and system limitations and hence the model parameters slightly differ from those in section 3.1 and 3.2. The horizontal model domain size is $L_x = L_y = 19\,440$ m. The atmospheric model has a vertical extension of $L_z = 3686$ m. The grid length Δx_i is 36 m in all spatial directions. The ABL is bounded by a temperature inversion of 3 K/100 m above $z_{inv} = 3000$ m. Within the inversion layer, the vertical grid length Δz is stretched to a value of 40 m. Thus, the total number of grid points in the atmosphere N_a is 2.9×10^7 . Below the inversion layer, the potential temperature has a constant value of 300 K. The geostrophic wind components are $u_g = -5\,\mathrm{ms}^{-1}$ and $v_g = 0\,\mathrm{ms}^{-1}$. The roughness length z_0 is set to 0.1 m. This is an unrealistic value for the roughness length over the ocean. Typical values for the ocean are 0.001 m (e.g. Stull, 1988). The value in the present study is chosen for comparison with the results by I. N. Esau (2009, personal communication) and is not changed during the whole study. For reducing the simulation time for reaching a stationary state in the atmosphere, a one-dimensional precursor run is used with a simulation time of 80 days and Rayleigh damping is used within the inversion layer (see section 2.8 and 2.7, respectively). For the ocean model, L_z is 72 m and the grid length Δx_i is 1.2 m in all spatial directions. The OML depth is defined to 60 m and is bounded by a temperature inversion of 5 K/100 m. The total number of grid points in the ocean N_o is 1.57×10^{10} . During the uncoupled precursor run, the ocean is driven by a constant momentum flux at the sea surface, with the same values as in section 3.2.2: $\overline{wu}_{0,o} = 4 \times 10^{-5}\,\mathrm{m^2\,s^{-2}}$ and $\overline{wv}_{0,o} = 9 \times 10^{-6}\,\mathrm{m^2\,s^{-2}}$, resulting in a friction velocity of $u_{*,o} = 6.4 \times 10^{-3}\,\mathrm{m\,s^{-1}}$.

The number of PEs is optimized after equation 2.101 to reduce idle times during the coupled simulation (see section 2.11). Therefore, the total number of grid points and the time steps is needed of the atmosphere and ocean. The time steps are estimated from previous simulations. Figure 3.37 presents time series of Δt_a and Δt_o from the atmospheric simulation E5 in section 3.1.4, and from the oceanic simulation in section 3.2.3.1 with $z_{inv} = -50$ m. The grid lengths

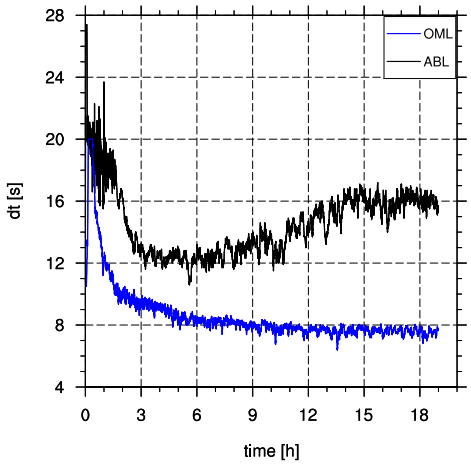

Figure 3.37.: Time series of atmospheric and oceanic time steps. The data are taken from simulations of section 3.1.4 and 3.2.3.1.

of these simulations are 40 m for the atmosphere and 1.25 m for the ocean. These grid lengths are larger than the used values for the coupled simulation and thus the time steps of the coupled simulation are smaller due to the CFL criterion, described in section 2.6. However, the values of the estimated time steps are adequate for the estimation of the optimum number of processors. The time averaged values of the time steps are $\Delta t_a \approx 15.7\,\mathrm{s}$ and $\Delta t_o \approx 7.6\,\mathrm{s}$. The average is calculated over the last 7 h in figure 3.37 which is equal to the coupling period. Inserting these values into equation 2.101 yields to

$$\frac{\#\mathrm{PE}_a}{\#\mathrm{PE}_o} \approx 8.9 \times 10^{-4} \approx \frac{1}{1100}\,. \tag{3.11}$$

For the choice of the number of PEs, the computer architecture should be considered. On the SGI Altix supercomputers of the HLRN, a node contains eight PEs, which share their memory. Because the computational time is billed per node, the used number of PEs should be a multiple of eight. The maximum number of processors is 2048 that could be used for this study. Further limitations are given by the used FFT method in PALM for solving the Poisson equation 2.45. Considering all limitations leads to the use of 8 PEs for the atmospheric flow and 1800 PEs for the oceanic flow. This gives a ratio of 4.4×10^{-3} and thus is larger as the calculated value in equation 3.11 which means that the atmospheric flow is calculated faster than the oceanic flow. This configuration ensures that the eight atmospheric PEs remain idle till the ocean model reaches the coupling interval $\Delta t_{coupling}$ and not vice versa. This saves computational costs because it is negligible if 8 PEs are running idle compared with 1800 PEs running idle.
For the 12 h of precursor run, the CPU-time of 1808PEs $\times$ 55 h were needed. For the coupling, the number of processors had to be reduced to 900 PEs for the ocean due to a memory overflow. As described in section 2.11 the complete field have to be defined on each PE which needs a large amount of memory. Because 8 PEs share their memory on the HLRN system, the memory per PE could be increased by reducing the number of PEs. Thus, for the 7 h of coupling, the used CPU-time was 908PEs $\times$ 85 h. Altogether, the coupled simulation needed 176 000 h of CPU-time and were extremely expensive.

3.3.2. Results

First of all, the difference between the uncoupled ocean simulation and the coupled ocean simulation should be explained. The uncoupled oceanic precursor run is driven by a constant friction velocity of $6.4 \times 10^{-3}\,\mathrm{m\,s^{-1}}$. During the coupled simulation, the ocean is driven by friction velocity of the atmosphere model. A snapshot of the friction velocity $u_{*,o}$ of the atmospheric simulation after 12 h of simulation time is presented in figure 3.38a. The friction velocity is not constant in space and exhibits local gradients. The vertical profiles of the components of the spatially and temporally averaged vertical momentum flux of atmosphere and ocean are taken during the coupled simulation and shown in figure 3.38b. The profiles reveal that the horizontally averaged surface values of $\rho_o\overline{wu}_{0,o}$ and $\rho_o\overline{wv}_{0,o}$ are equal to the values of the uncoupled oceanic precursor run, as it was intended. For the ocean model, the difference between the precursor run and the coupled simulation is that local gradients of the friction velocity are considered during the coupling.
The organized coherent areas with larger and smaller values of $u_{*,o}$ in figure 3.38a develop due to atmospheric roll vortices, as shown in section 3.1.2. These gradients produce large scale convergence and divergence zones at the ocean surface and hence can affect the flow within the OML. For an analysis of the influence of atmospheric roll vortices on the oceanic flow, results at the beginning of the coupling at $t = 12\,\mathrm{h}$ are compared to the results after 7 h of coupling time at $t = 19\,\mathrm{h}$. A coupling time of 7 h should be sufficient for observing an adjustment of the oceanic flow to signals of atmospheric roll vortices because the oceanic roll vortices are also developed in the first 7 h of simulation time in the uncoupled precursor run.

The time series of the resolved-scale turbulent kinetic energy E^* (normalized by the number of grid points) is given in figure 3.39. The time axis is divided into a positive and a negative part. Negative values represent the uncoupled simulation and positive values the coupled simulation. The ocean flow reaches a stationary state at the end of the precursor run. Comparing with results of section 3.1 and 3.2, the atmosphere reaches their stationary state after 15 h of simulation time during the coupled simulation. However, rolls are already developed after 12 h of simulation time.

Figure 3.40 presents horizontal cross-sections of the cross-roll velocity component v at the sea surface from the ocean simulation and shows a part of the model domain. A comparison between the cross-section at the beginning of the coupled simulation (Fig. 3.40a) and after 7 h of coupling (Fig. 3.40b) reveals that the values of v is more positive (red) at $t = 19\,\mathrm{h}$ than at $t = 12\,\mathrm{h}$. The spatially averaged profiles of v indicate this too (see figure 3.40c). The variability of the velocity component is caused by the inertial oscillation in the ocean and not by the coupling. Figure 3.40b shows larger areas with smaller bands of negative (red) or positive (blue) values of v which are wider than the other. Two of these larger areas, one with wider bands of positive values of v and one with wider bands of negative values of v, can be identified between 9 km and 16 km in y-direction. The wavelength of this superior structures is of the order of the atmospheric roll wavelength. Figure 3.40a does not show such areas. This is a first indication of an influence of the atmosphere on the ocean.

For further investigations, variance spectra are calculated after 12 h (left), 13 h (center) and 19 h (right) of simulation time (see figure 3.41). The upper spectra are calculated from the friction velocity in the atmosphere and the lower three spectra are calculated from the horizontal velocity component v in the ocean at the surface $z = 0\,\mathrm{m}$, in a depth of 2.4 m

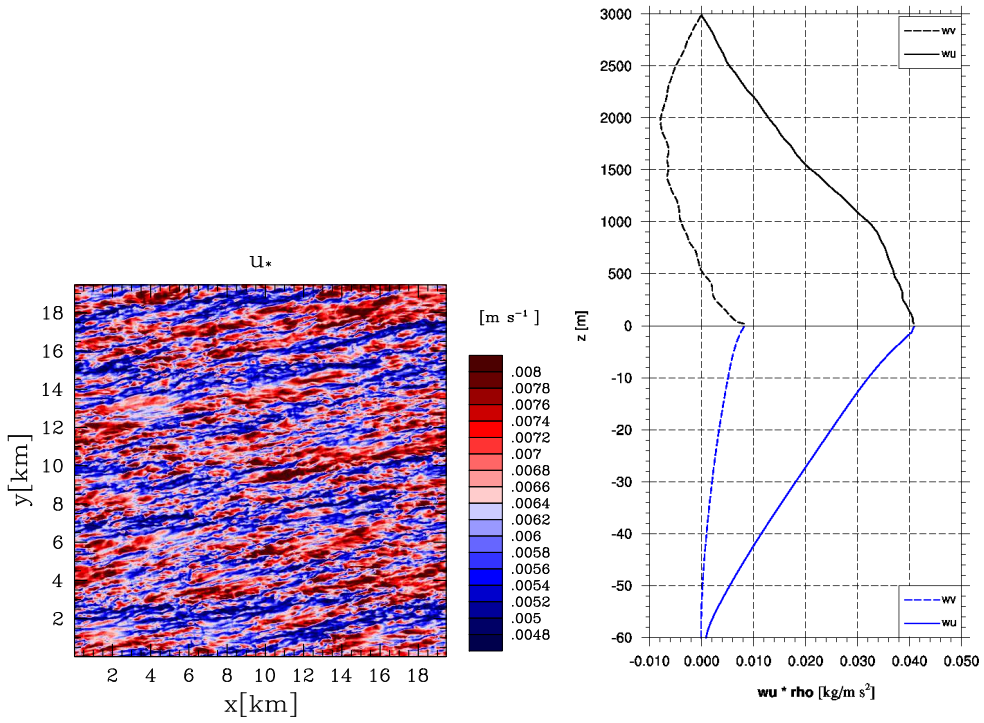

(a) (b)

Figure 3.38.: (a) Instantaneous horizontal cross-section of the friction velocity $u_{*,o}$ after 12 h of simulation time. The snapshot is taken from the atmospheric simulation and the values are multiplied by the factor $\sqrt{\rho_a/\rho_o}$. (b) Vertical profiles of the vertical momentum flux $\rho\overline{wu}$ and $\rho\overline{wv}$ during the coupling for atmosphere and ocean. The profiles are taken after 2 h of the coupling start time and averaged over an interval of 600 s. It should be noted that the scale of the vertical axis varies between atmosphere (above $z = 0$) and ocean (below $z = 0$).

and 9.6 m. At the beginning of the coupling at $t = 12$ h, S_{u_*} has local maxima at larger wavelengths, whereby the largest local maximum is at $\lambda = 6000$ m. S_v has no maxima at larger wavelengths at the beginning of the coupling. The range of the dominant oceanic wavelengths is between 60 m and 150 m for all three depths. After 1 h of coupling, S_v shows significant maxima at wavelengths between 3000 m and 8000 m at the surface, which can be traced back on the influence of the atmospheric roll vortices. In a depth of 9.6 m, an influence of the atmospheric roll vortices cannot be observed. After 19 h of simulation time, spectral peaks of S_v are between 3000 m and 10 000 m at the surface. In $z = -2.4$ m these maxima are decreased and in $z = -9.6$ m a small signal is left at $\lambda = 10\,000$ m. The spectra show that the atmospheric roll vortices induce coherent structures from the same wavelengths in the upper 10 m of the ocean but the signal in 10 m is very weak even after 7 h of coupling. Below this depth, the atmospheric roll vortices has no significant influence. Furthermore, the spectra S_v show that the oceanic roll vortices with a wavelength of approximately 100 m are not destroyed by the atmospheric roll vortices (Fig. 3.41).
The atmospheric spectra S_{u_*} shows that the spectral energy of the roll vortices decrease during the coupling. This may be explained by the fact that the atmospheric flow does reach a

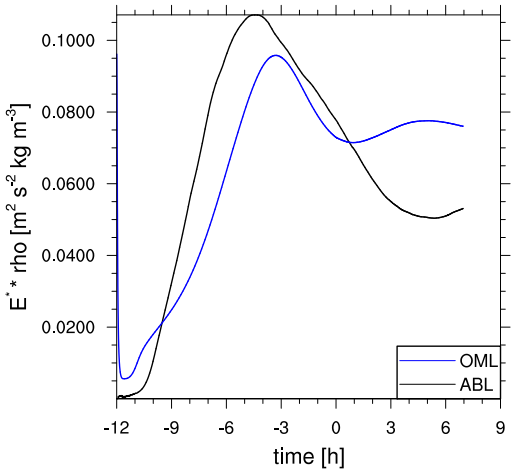

Figure 3.39.: Time series of the resolved-scale turbulent kinetic energy E^* (normalized by the number of grid points) of the ABL and OML flow.

stationary state during the coupling and not at the beginning as it is shown in figure 3.39.

Why the induced structures does not develop over the whole OML can be explained by the movement of the atmospheric rolls perpendicular to the roll axis. If the rolls drift across the ocean surface, the convergence and divergence zones at the surface move in the same way. Figure 3.42 illustrates the movement of the atmospheric rolls during the coupled simulation. The roll vortices move southward with a velocity of approximately $2.5\,\mathrm{km\,h^{-1}} \approx 0.7\,\mathrm{m\,s^{-1}}$. This is close to the value of the mean wind speed component $\overline{v}$ in this direction. Due to the higher viscosity in water, the adjustment time of the ocean is larger than the drifting time of the atmospheric roll vortices. For a comparison, the velocity of the ocean current is one order of magnitude smaller than the phase velocity of the atmospheric rolls. Thus, the ocean current is too slow for reacting on the atmospheric rolls in larger depths.

In general, the simulations show that the atmospheric roll vortices induce coherent structures in the OML. However, the influence is limited to the near surface area if the atmospheric rolls drift with a mean wind which is faster than the ocean current. Stationary roll vortices in the ABL might induce coherent structures extending over the whole OML. In a neutrally stratified ABL, the roll vortices are produced by the IPI and PI and need the mean wind for the roll development and thus, the rolls always have a phase speed. Stationary roll vortices are developed during cold-air outbreaks as shown by Gryschka et al. (2008). Such a case can be used for further investigations of this topic.

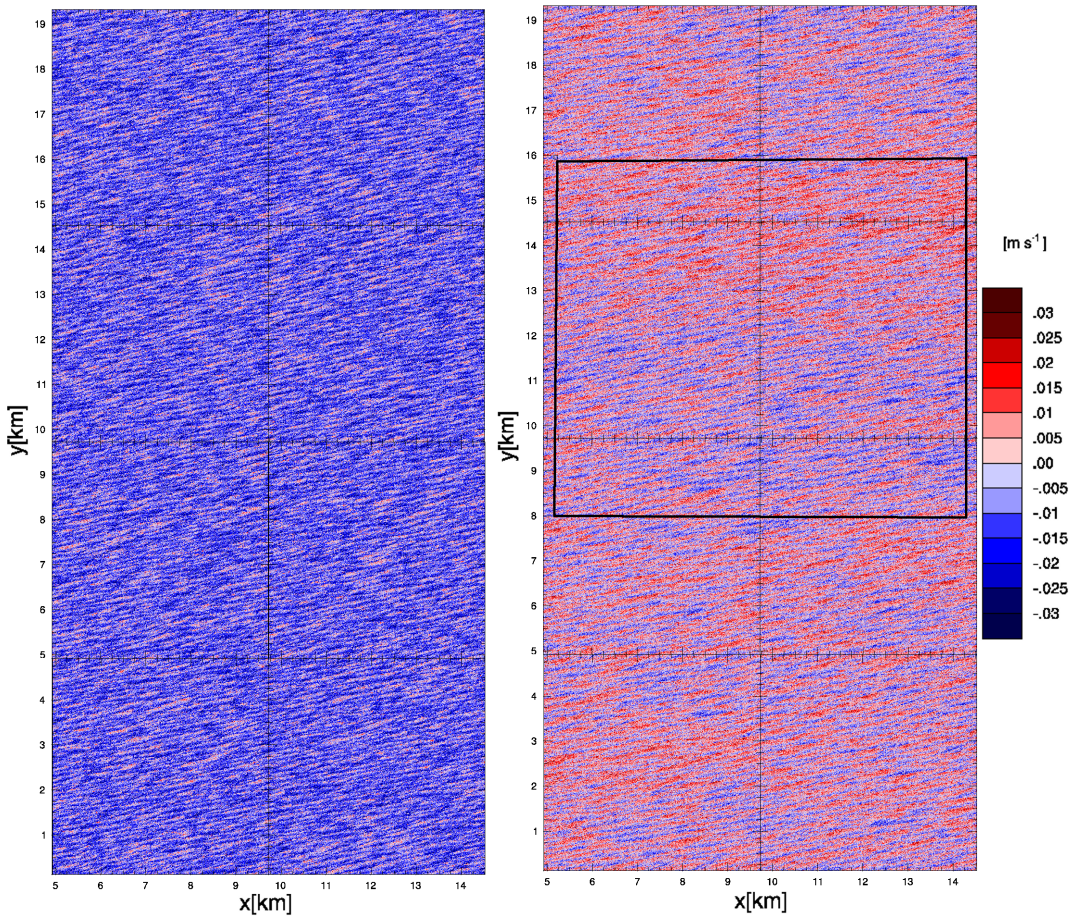

(a) t = 12 h (b) t = 19 h

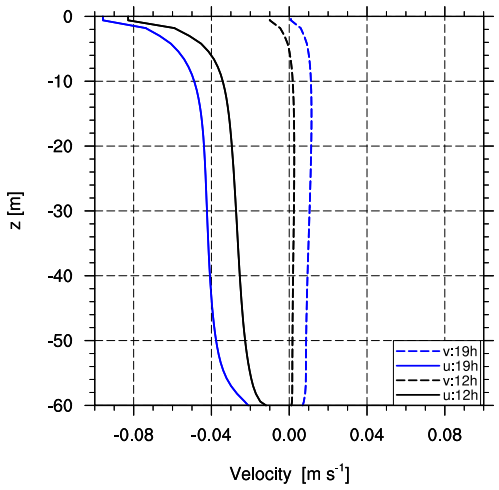

(c)

Figure 3.40.: Instantaneous horizontal cross-sections of the horizontal velocity component v in the ocean at $z = 0\,\mathrm{m}$ after (a) 12 h and (b) 19 h of simulation time. (c) Vertical profiles of the mean horizontal velocity components $\overline{u}$ and $\overline{v}$.

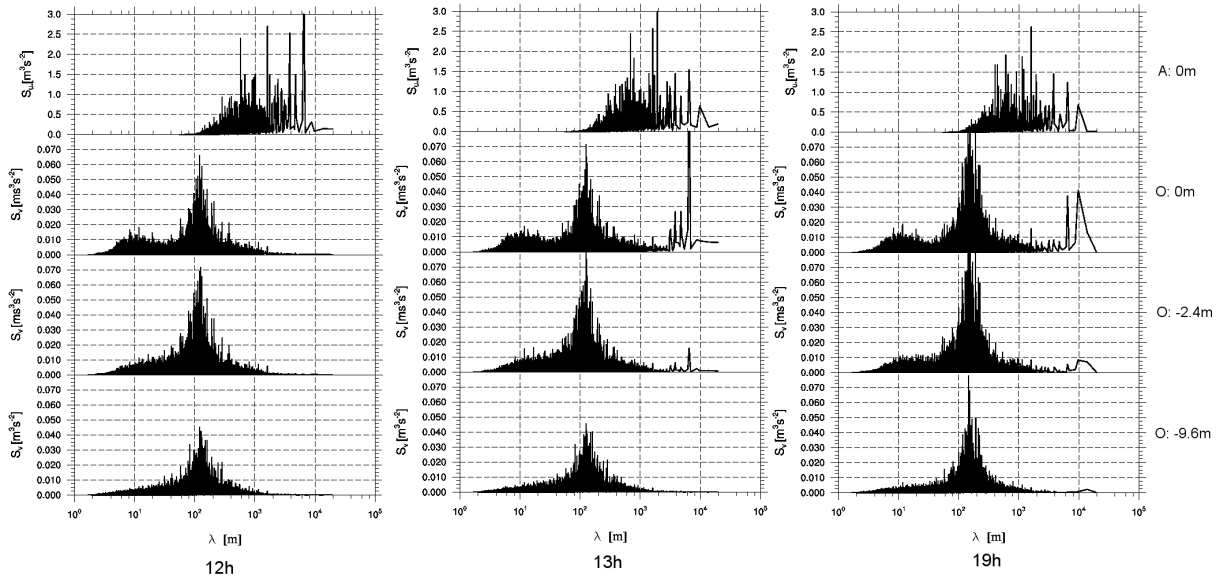

Figure 3.41.: Spectral energy density as a function of the wavelength λ calculated after 12 h (left), 13 h (center) and 19 h (right) of simulation time. The upper spectra result from the friction velocity u_* of the atmospheric simulation. The lower three spectra are calculated from the horizontal velocity component v of the ocean simulation for different depths.

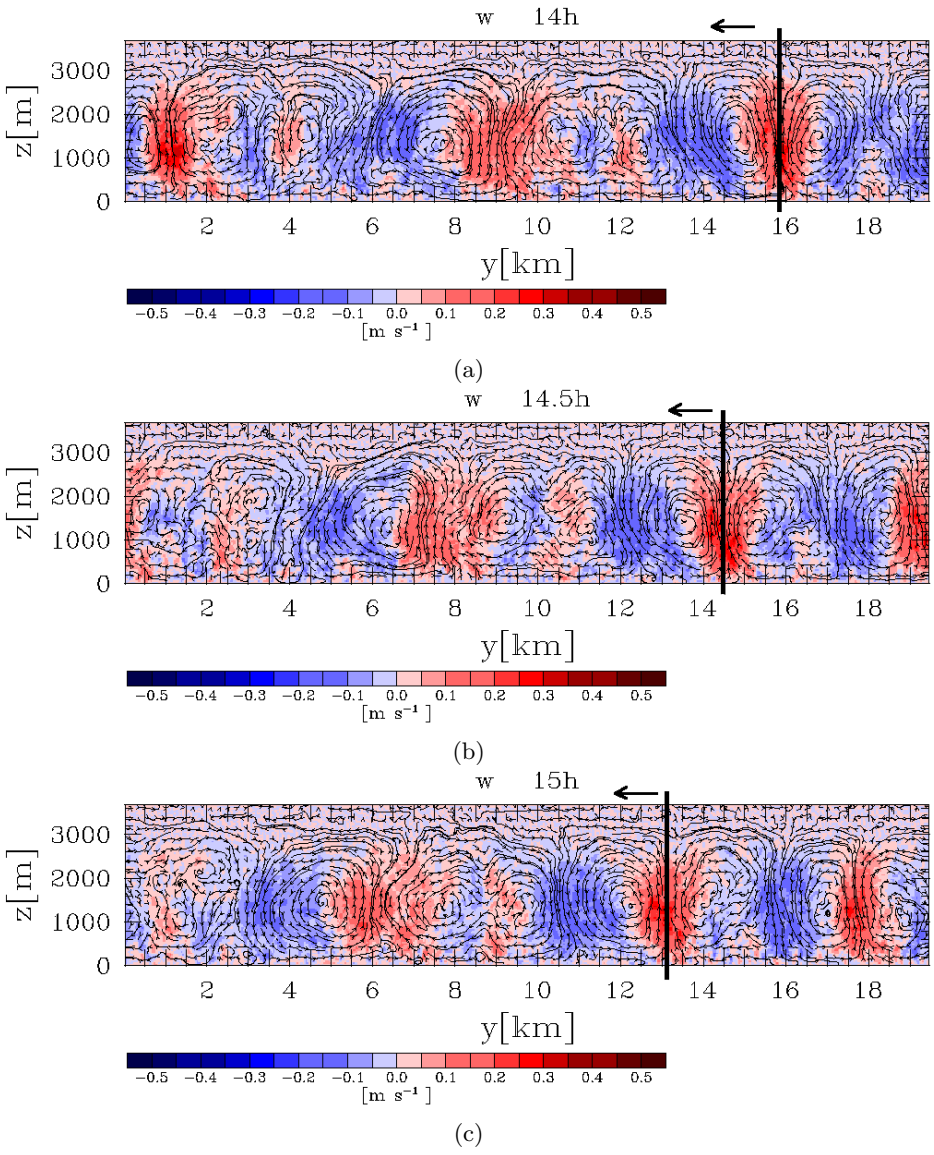

Figure 3.42.: Instantaneous vertical cross-sections of the vertical velocity w, averaged along the x-axis, and streamlines of (v^*, w^*). The snapshots are taken in 30 min intervals. For estimating the roll movement perpendicular to their roll axis, an updraft area of one roll pair is marked by a black line. The black arrow points in the direction of the movement. The distance between the black line in (a) and (b) is approximately 1.25 km as well as between (b) and (c). Hence, the rolls move approximately 2.5 km per hour.

4. Summary and Conclusion

The main purpose of the current study is to investigate if atmospheric roll vortices can induce large coherent structures in the ocean mixed layer (OML) which have the same wavelengths as the atmospheric roll vortices. With the LES model PALM, uncoupled and coupled simulations are carried out for atmosphere and ocean, simulating a neutrally stratified Ekman flow. The roll vortices develop in the Ekman flow due to the inflection point instability (IPI) and parallel instability (PI). The wavelength of the roll vortices varies for the atmospheric rolls and the oceanic rolls. Typical wavelengths are of several kilometers in the atmosphere and of several hundred meters in the ocean. Both length scales have to be resolved in the coupled simulation which requires a large amount of grid points and computational time.

A parameter study of the atmospheric boundary layer (ABL) shows that the roll axes are oriented along the mean horizontal wind. The wavelength is determined visually and by spectral analysis. Both methods reveal that the roll wavelength ranges between 4 km and 8 km within the ABL. The parameter study also shows that the roll development depends on latitude and wind direction. The rolls develop only in easterly wind regimes and not in westerly wind regimes. The roll vortices are more distinct at lower latitudes and do not develop at the pole region. These results are in agreement with studies by I. N. Esau (2009, personal communication) and Glazunov (2010) who supposed that this effect is attributable to the vertical component of the Coriolis force. The effect of the Coriolis force on the roll development is called parallel instability and was first described by Lilly (1966). In this study, the energy budget terms of the IPI, producing roll energy by shear, and PI, redistributing roll energy from the along-roll to the cross-roll component by the Coriolis force, are calculated to distinguish between both mechanisms and to support the theory of Lilly (1966). It is shown that the vertical Coriolis force has a similar amount of energy as the shear production term. If the ABL is well-mixed and reaches its stationary state, the shear production term along the roll axis and the redistribution term of the vertical Coriolis force maintain the developed roll vortices. It is also shown that in a flow without the vertical component of the Coriolis force, roll vortices do not develop.
Sensitivity studies of the effect of the model domain size on the roll vortices are carried out to save computational costs in the coupled simulation. The sensitivity studies show that the roll vortices can reach a vertical extent of 7 km and that roll pairs can develop one above an other. However, the real ABL would never reach such heights.

The ocean simulations show that roll vortices develop in the OML at lower latitudes due to the PI. By calculating the energy budget terms of the IPI and PI it is shown that the vertical Coriolis force has the same influence as on the ABL flow. A sensitivity study reveals that the wavelength of the roll vortices ranges between 120 m and 240 m, depending on the OML depth, and that an OML depth of 40 m is at least necessary for the roll development. A sensitivity study of the grid resolution leads to the result that a grid length of 1.25 m is a limiting value for resolving large coherent structures. This result may explain, why Zikanov et al. (2003) could not find roll vortices in their simulation results of a wind driven Ekman

flow in the ocean. Their smallest grid resolution was approximately 8 m.

The coupled atmosphere-ocean simulation is divided into two phases. During the first phase, atmosphere and ocean were not coupled until roll vortices developed in both flows. In the second phase, the coupling was activated. Spectra of the velocity component v show wavelengths between 6 km and 10 km at the sea surface at the end of the coupled simulation. These wavelengths are not presented at the beginning of the coupling. Thus, the large wavelength can be traced back to the atmospheric roll vortices. However, the effect strongly decreases below the sea surface. In a depth of 10 m the signal is negligibly small after 7 h of coupling. The coherent structures caused by the atmospheric roll vortices have only a small vertical extend because the atmospheric roll vortices drift with the mean wind perpendicular to their roll axis. The atmospheric rolls move with a velocity of $0.7\,\mathrm{ms}^{-1}$ over the sea surface and the ocean is too slow to react on the constant changes.
The results show that the atmospheric roll vortices induce large coherent structures in the OML. However, the effect is limited to the near sea surface region because of the drift of the atmospheric roll vortices. The effect of the atmospheric roll vortices on the ocean should be more distinct in stationary roll situations. Stationary roll vortices can be observed during cold-air outbreaks as shown by Gryschka et al. (2008). However, the model domain size of their study is five times larger than the coupled simulation of the current study.
The flow structure at the sea surface shows that the oceanic roll vortices with a wavelength of 100 m are still present and the coherent circulation caused by atmospheric roll vortices is superimposed to the smaller roll vortices caused by the PI in the ocean. However, further studies are necessary for the investigation of the interaction between both roll systems.

Appendix

A. Polynomials for calculation of the sea water density

$P_n(S,\theta,p)$	Coefficients	$P_d(S,\theta,p)$	Coefficients
Constant	$9.998\,408\,554\,484\,934\,7 \times 10^{2}$	Constant	1.0
θ	$7.347\,162\,586\,098\,158\,4 \times 10^{0}$	θ	$7.281\,521\,011\,332\,709\,1 \times 10^{-3}$
θ^2	$-5.321\,123\,179\,284\,176\,9 \times 10^{-2}$	θ^2	$-4.478\,726\,546\,198\,392\,1 \times 10^{-5}$
θ^3	$3.649\,243\,910\,981\,454\,9 \times 10^{-4}$	θ^3	$3.385\,100\,296\,580\,243\,0 \times 10^{-7}$
S	$2.588\,057\,102\,399\,139\,0 \times 10^{0}$	θ^4	$1.365\,120\,238\,975\,857\,2 \times 10^{-10}$
$S\theta$	$-6.716\,828\,278\,669\,235\,5 \times 10^{-3}$	S	$1.763\,212\,666\,904\,037\,7 \times 10^{-3}$
S^2	$1.920\,320\,205\,576\,015\,1 \times 10^{-3}$	$S\theta$	$-8.806\,658\,325\,120\,647\,4 \times 10^{-6}$
p	$1.179\,826\,374\,043\,036\,4 \times 10^{-2}$	$S\theta^3$	$-1.883\,268\,943\,480\,489\,7 \times 10^{-10}$
$p\theta^2$	$9.892\,021\,926\,639\,911\,7 \times 10^{-8}$	$S^{3/2}$	$5.746\,377\,674\,543\,209\,7 \times 10^{-6}$
pS	$4.699\,664\,277\,175\,473\,0 \times 10^{-6}$	$S^{3/2}\theta^2$	$1.471\,627\,547\,224\,233\,4 \times 10^{-9}$
p^2	$-2.586\,218\,707\,515\,435\,2 \times 10^{-8}$	p	$6.710\,324\,628\,565\,189\,4 \times 10^{-6}$
$p^2\theta^2$	$-3.292\,141\,400\,796\,066\,2 \times 10^{-12}$	$p^2\theta^3$	$-2.446\,169\,800\,702\,458\,2 \times 10^{-17}$
		$p^3\theta$	$-9.153\,441\,760\,428\,906\,2 \times 10^{-18}$

Table A.1.: Terms and coefficients of the polynomials $P_n(s,\theta,p)$ and $P_d(S,\theta,p)$ that define the rational function equation of state used in PALM (see Eq. 2.78 and 2.80). The table is taken from Jackett et al. (2006, table A2).

Bibliography

Aelbrecht, D., G. C. D'Hieres, and D. Renouard, 1999: Experimental study of the Ekman layer instability in steady or oscillating flows. *Cont. Shelf Res.*, **19**, 1851–1867.

Arakawa, A. and V. R. Lamb, 1977: Computational design of the basic dynamical processes of the UCLA general circulation model. *Methods Comput. Phys.*, **16**, 173–263.

Berkooz, G., P. Holmes, and J. L. Lumley, 1993: The proper orthogonal decomposition in the analysis of turbulent flows. *Annu. Rev. Fluid Mech.*, **25**, 539–575.

Blackadar, A. K., 1962: The vertical distribution of wind and turbulent exchange in a neutral atmosphere. *J. Geophys. Res.*, **67**, 3095–3102.

Brown, R. A., 1972: On the inflection point instability of a stratified Ekman boundary layer. *J. Atmos. Sci.*, **29**, 850–859.

Brown, R. A., 1980: Longitudinal instabilities and secondary flows in the planetary boundary layer: A review. *Rev. Geophys. Space Phys.*, **18**, 683–697.

Brümmer, B., 1985: Strucutre, dynamics and energetics of boundary layer rolls from KonTur aircraft observations. *Beitr. Phys. Atmos.*, **58**, 237–254.

Chen, W., M. L. Banner, E. J. Walsh, J. B. Jensen, and S. Lee, 2001: The southern ocean waves experiment. Part II: Sea surface response to wind speed and wind stress variations. *J. Phys. Oceanogr.*, **31**, 174–198.

Chorin, A. J., 1968: Numerical solution of the Navier-Stokes equations. *Math. Comput.*, **22**, 745–762.

Coleman, G. N., J. H. Ferziger, and P. R. Spalart, 1990: A numerical study of the turbulent Ekman layer. *J. Fluid Mech.*, **213**, 313–348.

Courant, R., K. Friedrich, and H. Lewy, 1928: Über die partiellen Differenzengleichungen der mathematischen Physik. *Math. Ann.*, **100**, 32–74.

Craik, A. D. D. and S. Leibovich, 1976: A rational model for Langmuir circulations. *J. Fluid Mech.*, **73**, 401–426.

Deardorff, J. W., 1972: Numerical investigation of neutral and unstable planetary boundary layers. *J. Atmos. Sci.*, **29**, 91–115.

Deardorff, J. W., 1980: Stratocumulus-capped mixed layers derived from a three-dimensional model. *Bound.-Layer Meteor.*, **18**, 495–527.

Detering, H. W. and D. Etling, 1985: Application of the E - ϵ turbulence model to the atmospheric boundary layer. *Bound.-Layer Meteor.*, **33**, 113–133.

Drobinski, P., R. A. Brown, P. H. Flamant, and J. Pelon, 1998: Evidence of organized large eddies by ground-based doppler lidar, sonic anemometer and sodar. *Bound.-Layer Meteor.*, **88**, 343–361.

Drobinski, P. and R. C. Foster, 2003: On the origin of near-surface streaks in the neutrally-stratified planetary boundary layer. *Bound.-Layer Meteor.*, **108**, 247–256.

Dubos, T., C. Barthlott, and P. Drobinski, 2008: Emergence and secondary instability of Ekman layer rolls. *J. Atmos. Sci.*, **65**, 2326–2342.

Dyer, A. J., 1974: A review of flux-profile relationships. *Bound.-Layer Meteor.*, **7**, 363–372.

Ekman, V. W., 1905: On the influence of the earth's rotation on ocean currents. *Ark. Mat. Astron. Fys.*, **2**, 1–53.

Esau, I. N., 2003: The Coriolis effect on coherent structures in planetary boundary layers. *J. Turbulence*, **4**, 17.

Etling, D., 1971: The stability of an Ekman boundary layer flow as influenced by the thermal stratification. *Beitr. Phys. Atmos.*, **44**, 168–186.

Etling, D., 2002: *Theoretische Meteorologie: Eine Einführung*. Springer-Verlag, 354 pp.

Etling, D. and R. A. Brown, 1993: Roll vortices in the planetary boundary layer: A review. *Bound.-Layer Meteor.*, **65**, 215–248.

Etling, D. and F. Wippermann, 1975: On the instability of a planetary boundary layer with Rossby-number similarity. *Bound.-Layer Meteor.*, **9**, 341–360.

Faller, A. J., 1963: An experimental study of the instability of the laminar Ekman boundary layer. *J. Fluid Mech.*, **15**, 560–576.

Faller, A. J., 1965: Large eddies in the atmospheric boundary layer and their possible role in the formation of cloud rows. *J. Atmos. Sci.*, **22**, 176–184.

Faller, A. J. and R. E. Kaylor, 1966: A numerical study of instability of the laminar Ekman boundary layer. *J. Atmos. Sci.*, **23**, 466–480.

Foster, R. C., 1997: Structure and energetics of optimal Ekman layer pertubations. *J. Fluid Mech.*, **333**, 97–123.

Fröhlich, J., 2006: *Large eddy Simulation turbulenter Strömungen*. B.G. Teubner Verlag, 414 pp.

Garratt, J. R., 1992: *The atmospheric boundary layer*. Cambridge University Press, 316 pp.

Gerkema, T., J. T. F. Zimmerman, L. R. M. Maas, and H. van Haren, 2008: Geophysical and astrophysical fluid dynamics beyond the traditional approximation. *Rev. Geophys.*, **46**, 33.

Glazunov, A. V., 2010: On the effect that the direction of geostrophic wind has on turbulence and quasiordered large-scale structures in the atmospheric boundary layer. *Izv. Acad. Sci. USSR, Atmos. Oceanic Phys.*, **46**, 727–747.

Glazunov, A. V. and V. N. Lykossov, 2003: Large-eddy simulation of interaction of ocean and atmospheric boundary layers. *Russ. J. Numer. Anal. Math. Model.*, **18**, 279–295.

Glendening, J. W., 1996: Lineal eddy features under strong shear conditions. *J. Atmos. Sci.*, **53**, 3430–3449.

Gryschka, M., C. Dre, D. Etling, and S. Raasch, 2008: On the influence of sea-ice inhomogeneities onto roll convection in cold-air outbreaks. *Geophys. Res. Lett.*, **35**, L23 804.

Iverson, K. E., 1962: *A programming language*. John Wiley & Sons Inc, 286 pp.

Jackett, D. R., T. J. McDougall, R. Feistel, D. G. Wright, and S. M. Griffies, 2006: Algorithms for density, potential temperature, conservative temperature, and the freezing temperature of seawater. *J. Atmos. Oceanic Technol.*, **23**, 1709–1728.

Klemp, J. B. and D. K. Lilly, 1978: Numerical simulation of hydrostatic mountain waves. *J. Atmos. Sci.*, **35**, 78–107.

Kolmogorov, A. N., 1941: The local structure of turbulence in incrompressible viscous fluid for very large Reynolds numbers. *Dokl. Akad. Nauk. SSSR.*, **32**, 299–303, Reprinted in: Proc. R. Soc. Lond. A 434, 9-13 (1991).

Kolmogorov, A. N., 1942: The equations of turbulent motion in an incompressible fluid. *Izv. Acad. Sci. USSR, Phys.*, **6**, 56–58.

Kraus, E. B. and J. A. Businger, 1994: *Atmosphere-ocean interaction*. Oxford University Press, 362 pp.

Kraus, H., 2008: *Grundlagen der Grenzschicht-Meteorologie*. 1, Springer Verlag, 214 pp.

Langmuir, I., 1938: Surface motion of water induced by wind. *Science*, **87**, 119–123.

Leibovich, S., 1983: The form and dynamics of Langmuir circulations. *Annu. Rev. Fluid Mech.*, **15**, 391–427.

Leibovich, S. and S. K. Lele, 1985: The influence of the horizontal component of earth's angular velocity on the instability of the Ekman layer. *J. Fluid Mech.*, **150**, 41–87.

LeMone, M. A., 1973: The structure and dynamics of horizontal roll vortices in the planetary boundary layer. *J. Atmos. Sci.*, **30**, 1077–1091.

LeMone, M. A., 1976: Modulation of turbulence energy by longitudinal rolls in an unstable planetary boundary layer. *J. Atmos. Sci.*, **33**, 1308–1320.

Lilly, D. K., 1966: On the instability of Ekman boundary flow. *J. Atmos. Sci.*, **23**, 481–494.

Mason, P. J. and D. J. Thomson, 1987: Large-eddy simulation of the neutral-static-stability planetary boundary. *Quart. J. Roy. Meteor. Soc.*, **113**, 413–443.

Moeng, C.-H. and P. P. Sullivan, 1994: A comparison of shear- and buoyancy-driven planetary boundary layer flows. *J. Atmos. Sci.*, **51**, 999–1022.

Monin, A. S. and A. M. Obukhov, 1954: Basic laws of turbulent mixing in the surface layer of the atmosphere. *Tr. Geofiz. Inst., Akad. Nauk SSSR*, **24**, 163–187.

Noh, Y., H. S. Min, and S. Raasch, 2004: Large eddy simulation of the ocean mixed layer: The effects of wave breaking and Langmuir circulation. *J. Phys. Oceanogr.*, **34**, 720–735.

Patrinos, A. A. N. and A. L. Kistler, 1977: A numerical study of the chicago lake breeze. *Bound.-Layer Meteor.*, **12**, 93–123.

Piacsek, S. A. and G. Williams, 1970: Conservation properties of convection difference schemes. *J. Comput. Phys.*, **6**, 392–405.

Prandtl, L., 1945: Über ein neues Formelsystem für die ausgebildete Turbulenz. *Nachr. Akad. Wiss. Göttingen, Math-Phys*, **K1**, 6–19.

Prandtl, L., K. Oswatitsch, and K. Wieghardt, 1969: *Führer durch die Str¨mungslehre.* Friedr. Vieweg + Sohn GmbH, 535 pp.

Prandtl, L. and W. Tollmien, 1924: Die Windverteilung über dem Erdboden, errechnet aus den Gesetzen der Rohrströmung. *Z. Geophys.*, **1**, 47–55.

Raasch, S. and M. Schröter, 2001: Palm - A large-eddy simulation model preforming on massively parallel computers. *Meteorol. Z.*, **10**, 363–372.

Reynolds, O., 1883: An experimental investigation of the circumstances which determine wether the motion of water shall be direct or sinuous, and of the law of resistance in parallel channels. *Philos. Trans. Roy. Soc. London*, **174**, 935–982.

Roache, P. J., 1985: *Computational fluid dynamics.* 6th ed., Hermosa Publishers, 446 pp.

Schumann, U., 1975: Subgrid scale model for finite difference simulations of turbulent flows in plane channels and annuli. *J. Comput. Phys.*, **18**, 376–404.

Sheng, J., D. G. Wright, R. J. Greatbatch, and D. E. Dietrich, 1998: CANDIE: A new version of the DieCAST ocean circulation model. *J. Atmos. Oceanic Technol.*, **15**, 1414–1432.

Smith, S. W., 1997: *The scientist & engineer's guide to digital signal processing.* California Technical Pub., 626 pp.

Steinhorn, I., 1991: Salt flux and evaporation. *J. Phys. Oceanogr.*, **21**, 1681–1683.

Stensrud, D. J. and H. N. Shirer, 1988: Development of boundary layer rolls from dynamic instabilities. *J. Atmos. Sci.*, **45**, 1007–1019.

Stewart, R. H., 2008: *Introduction to physical oceanography.* Open source textbook, 345 pp., URL `http://oceanworld.tamu.edu/resources/ocng_textbook/contents.html`.

Stull, R. B., 1988: *An introduction to boundary layer meteorology.* Springer Science + Business Media B.V., 670 pp.

Tennekes, H. and J. L. Lumley, 1972: *A first course in turbulence.* The MIT Press, 300 pp.

Thorpe, S. A., 2004: Langmuir circulation. *Annu. Rev. Fluid Mech.*, **35**, 55–79.

Thorpe, S. A., 2005: *The turbulent ocean.* Cambridge University Press, 439 pp.

Walter, B. A. and J. E. Overland, 1984: Observations of longitudinal rolls in a near neutral atmosphere. *Mon. Wea. Rev.*, **112**, 200–208.

Weckwerth, T. M., J. W. Wilson, R. M. Wakimoto, and N. A. Crook, 1997: Horizontal convective rolls: Determining the environmental conditions supporting their existence and characteristics. *Mon. Wea. Rev.*, **125**, 505–526.

Williamson, J. H., 1980: Low-storage Runge-Kutta schemes. *J. Comput. Phys.*, **35**, 48–56.

Wippermann, F., 1969: The orientation of vortices due to instability of the Ekman-boundary layer. *Beitr. Phys. Atmos.*, **42**, 225–244.

Young, G. S., D. A. R. Kristovich, M. R. Hjelmfelt, and R. C. Foster, 2002: Rolls, streets, waves, and more: A review of quasi-two-dimensional structures in the atmospheric boundary layer. *Bull. Amer. Meteor. Soc.*, **83**, 997–1001.

Zikanov, O., D. N. Slinn, and M. R. Dhanak, 2003: Large-eddy simulations of the wind-induced turbulent Ekman layer. *J. Fluid Mech.*, **495**, 343–368.

Acknowledgment

First of all, I would like to thank my supervisor, Prof. Dr. Siegfried Raasch, for his continuous guidance and supervision, particularly for the motivating discussions, which supported the progress of this work, and for the hints to solve technical problems.
I have to thank Dr. Igor Esau for offering this topic.
I would like to thank all members of the PALM group for their help with several technical problems that occurred during this work. A special thanks goes to Dr. Micha Gryschka for the discussions on the subject.

I would also like to thank the members of the HLRN for the technical support on the supercomputing system.

I am very grateful to Viola Hilger, Farah Kanani, Matthias Sühring and Linda Voß for correcting my work and for all the valuable hints for improvement of this work. I also thank them, as well as Michael Schrempf, for the great collaboration during my studying.

For any kind of support during my studying, I sincerely thank my brother Sascha and my parents Marion and Hermann.
Finally, I sincerely thank Clara Werder for her moral support during this work.

Eidesstattliche Erklärung

Hiermit erkläre ich, dass ich die vorliegende Diplomarbeit selbständig und nur unter Verwendung der angegebenen Quellen und Hilfsmittel sowie dem Rat meiner akademischen Lehrer angefertigt habe.

Hannover, 23. Juni 2011